UNIVERSITA' DEGLI STUDI DI MILANO-BICOCCA

Facoltà di Scienze Matematiche, Fisiche e Naturali

PhD School in Nanostructures and Nanotechnologies

# Recombination processes and carrier dynamics in Ge/SiGe multiple quantum wells

PhD thesis of

Eleonora Gatti

Reg. Nr. 048151

**Supervisor:** Prof. Mario Guzzi

**Coordinator:** Prof. Gianfranco Pacchioni

Academic Year 2010-2011

*To the people*
*who have conveyed to me*
*and shared with me*
*the fascination for physics*

# Contents

**List of abbreviations** ............ **7**

**List of symbols** ............ **8**

**1. Introduction** ............ **9**

**2. Structural and optical properties of Ge/SiGe quantum wells** ............ **14**

2.1. SiGe alloys ............ 14

2.1.1. Structural properties ............ 15

2.1.2. Electronic properties ............ 16

2.2. Band alignment and band structure of Ge/SiGe quantum wells ............ 21

2.3. Optical properties of Ge/SiGe quantum wells ............ 25

2.3.1. Absorption ............ 25

2.3.2. Temperature dependence of absorption spectra ............ 28

2.3.3. Quantum Confined Stark Effect ............ 29

2.3.4. Continuous wave photoluminescence ............ 31

2.3.5. Carrier dynamics ............ 33

**3. Indirect gap related emission** ............ **36**

3.1. General features of the indirect recombination ............ 36

3.2. Decay time of the indirect recombination ............ 41

3.2.1. Decay time values ............ 41

3.2.2. Decay time dependence on the emission wavelength ............ 43

3.2.3. Decay time dependence on well thickness ............ 45

3.2.4. Decay time dependence on temperature ............ 49

3.3. Conclusions ............ 51

**4. Direct gap related emission** ............ **53**

4.1. General features ............ 53

4.1.1. Self absorption ............ 56

4.1.2. Emission from high energy states ............ 57

4.2. Temperature dependence of the CW-PL spectra …… 60
4.3. CW-PL spectra: resonant and non-resonant excitation conditions …… 66
4.4. Photoluminescence and relaxation processes …… 69
4.4.1. Decay time of the direct recombination …… 69
4.4.2. Spectra as a function of the excitation wavelength …… 70
4.4.3. TR pump-probe ABS measurements …… 76
4.5 Conclusions …… 78

**5. Conclusions …… 80**

**Appendix A …… 83**
A.1. Band alignment …… 83
A.2. Electronic states in quantum wells …… 85
A.3. Optical transitions in quantum wells …… 88
A.4. Excitons in 2D systems …… 90

**Appendix B …… 92**
B.1. Ge/SiGe quantum wells grown via LEPECVD …… 92
B.1.1. LEPECVD …… 92
B.1.2. Sample structure …… 94
B.2. Continuous wave photoluminescence and linear absorption measurements …… 99
B.3. Decay time measurements …… 100
B.3.1. Measurement of the indirect gap related decay time …… 101
B.3.2. Extraction of the PL decay time from the experimental measurements …… 102
B.3.3. Measurement of the direct gap related decay time …… 105
B.4. Photoluminescence as a function of excitation wavelength …… 107
B.5. Time resolved pump-probe absorption measurements …… 108

**List of publications …… 109**

**Acknowledegments …… 111**

**Bibliography …… 113**

# List of abbreviations

| | |
|---|---|
| 1D: | one-dimensional |
| 2D: | two-dimensional |
| ABS: | absorption |
| CB: | conduction band |
| CW-PL: | continuous-wave photoluminescence |
| DOS: | density of states |
| EMA: | effective mass approximation |
| FWHM: | full width half maximum |
| GVS: | graded virtual substrate |
| HH: | heavy hole |
| HR XRD: | high resolution X-ray diffraction |
| HWHM: | half width half maximum |
| IDWA: | infinitely deep well approximation |
| LA: | longitudinal acoustic |
| LEPECVD: | low-energy plasma-enhanced chemical vapor deposition |
| LH: | light hole |
| LO: | longitudinal optical |
| LT: | low temperature (2-14K) |
| MQW: | multiple quantum well |
| OD: | optical density |
| PL: | photoluminescence |
| QCSE: | Quantum Confined Stark effect |
| QW: | quantum well |
| RT: | room temperature |
| SO: | split-off |
| SS: | Stokes shift |
| T: | temperature |
| TA: | transversal acoustic |
| TE: | transversal electric |
| TM: | transversal magnetic |
| TDD: | threading dislocation density |
| TO: | transversal optical |
| TR: | time-resolved |
| TR-PL: | time-resolved photoluminescence |
| VB: | valence band |
| VS: | virtual substrate |
| XRD: | X-ray diffraction |

# List of symbols

| | |
|---|---|
| $\alpha$: | absorption coefficient |
| $\Delta t$: | time delay |
| $\Delta\alpha L$: | differential absorption |
| $\lambda_{exc}$: | excitation wavelength |
| $a$: | lattice constant |
| $c\Gamma n$: | $n$-th conduction confined state at $\Gamma$ |
| $cLn$: | $n$-th conduction confined state at L |
| $E_g$: | energy gap |
| $E_{g,dir}$: | direct energy gap |
| $E_{g,ind}$: | indirect energy gap |
| $HHn$: | $n$-th heavy hole confined state |
| $I_{dir}$: | integrated intensity of the direct emission |
| $I_{ind}$: | integrated intensity of the indirect emission |
| $\mathbf{k}$: | wavevector |
| $\mathbf{k}_{\parallel}$: | in-plane wavevector |
| $L_z$: | quantum well thickness |
| $LHn$: | $n$-th light hole confined state |
| $n$: | subband index |
| $S'_{HH}$, $S_{LH}$, $S_{HH}$: | satellite PL peaks (see Section 4.4.2) |
| $V_0$: | height of the potential barrier in a real quantum well |
| $\tau_{tot}$: | total (measured) decay time |
| $\tau_{rad}$: | radiative component of the decay time |
| $\tau_{nonrad}$: | non-radiative component of the decay time |
| $\tau_{therm}$: | thermalization time |
| $\tau_{ISB}$: | intersubband scattering time |
| $\tau_{\Gamma\text{-}rad}$: | decay time of the direct transition |
| $\tau_{L\text{-}rad}$: | decay time of the indirect transition |
| $\tau_{L\text{-}relax}$: | $\Gamma$ to L scattering time |

# Chapter 1

# Introduction

At the beginning of the semiconductor age, germanium (Ge) had a very important role. In fact, also thanks to its application in devices, mainly semiconductor diodes, Ge was a very diffusely studied semiconductor: papers concerning the Ge band structure and the Ge electrical and optical properties were published already in the forties of the last century. In the same years many efforts were devoted to the development of growth techniques aimed at obtaining high quality Ge single crystals. The first demonstration of a transistor was obtained by Bardeen, Brattain, and Shockley in 1950 using a Ge-based device. Anyway, in the following decades the interest for Ge strongly reduced, due to the main characteristics of another semiconducting material, the silicon (Si), and to the development of the Si-based MOS technology. In fact, the intrinsic carrier concentration in Si is much lower than in Ge, and thus in Si the room temperature (RT) conductivity can be determined by the doping concentration only. Furthermore, its oxide ($SiO_2$) is stable, tough and it is exceptionally plentiful in nature. In recent years a renewed interest in Ge has risen for its potentialities in electronics, where Ge is now mainly used to gain higher mobility (see, e.g., Refs. [1, 2]), and in photonics, where Ge is considered by different authors a good candidate to reach the challenging aim of integrating efficient optical properties on the Si-platform.[3, 4]

Indeed, recently many efforts are developed aimed at obtaining materials that are both integrable on the CMOS technology and characterized by good optical properties. The direct gap heterostructures based on III-V and II-VI semiconductors cannot satisfy both these requirements at the same time: direct gap III-V and II-VI semiconductors are characterized by efficient optical properties, but cannot be easily integrated on the CMOS technology. On the contrary, Ge not only is compatible with the Si platform, but it is also characterized by the so-called *quasi direct* optical behavior; this means that its optical properties are strongly influenced by transitions at the centre of the Brillouin zone due to the small energy distance

between the direct gap and the fundamental indirect gap (about 140 meV at RT). Prototype components for optical interconnection such as thin Ge-based photodetectors[5 - 7] and optical modulators based on the Franz-Keldysh effect[8] have already been realized thank to these peculiar optical properties. Furthermore, optically pumped laser emission at RT has been reported in n-doped Ge-on-Si structures,[9] thanks to the degrees of freedom provided by the control of the strain, which allows some tailoring of the energy distance between the conduction L and Γ minima, and by the n-type doping, which favors the population of the Γ minimum.[10, 11]

In the last twenty years, the advance of epitaxial growth techniques, such as MOCVD (*Metal Organic Chemical Vapor Deposition*) and MBE (*Molecular Beam Epitaxy*),[12] has allowed to grow innovative semiconductor heterostructures, with high control of interfaces and good structural quality. The possibility to grow heterostructures whose band aligment allows to spatially confine the carriers is very promising from the point of view of optical properties. As a matter of fact, if the extent of the spatial confinement is comparable with carrier De Broglie wavelength, quantum mechanical effects occur, such as the discretization of energy levels, whose spacing is determined by the dimension of the heterostructure and by the band offsets. A heterostructure in which electrons and holes are confined in one dimension, while act as free carriers in the other two directions, is called *quantum well* (QW). In a QW the confinement modifies the bandstructure and the density of states (DOS) respect to bulk semiconductors. Moreover, if electrons and holes are confined in the same spatial region (*type-I* QWs), the increase of the superposition between electron and hole wavefunctions, yields an enhancement of the absorption coefficient and of the recombination efficiency. Furthermore, the dependence of confinement energies on QW thickness, composition and strain level adds further degrees of freedom in the tailoring of the so-called *optical gap*, i.e. the energy distance between the first confined valence level and the first confined conduction level.
Indeed, very efficient and widely diffused devices are based on direct gap, III-V semiconductor QWs, such as QW lasers.[13]

Due to their compatibility to the CMOS platform, SiGe-based QWs have attracted great interest in the recent years. The attention was first devoted to Si-rich QWs, thanks to their easier integration on the Si-platform. Nevertheless, Si-rich heterostructures are characterized by a low optical efficiency due to the indirect nature of the bandgap and to the *type-II* band

alignment (i.e. electrons and holes are confined in different spatial regions of the heterostructure). Consequently, despite the integration limits due to a huge lattice mismatch, the interest has moved to Ge-rich QWs, which are characterized by a type-I band aligment and by a quasi-direct optical gap, because, like Ge, their optical properties are strongly influenced by direct type transitions.
In particular, Ge QWs with Ge-rich barriers present a type-I band alignment for both the Γ− and the L-type states, as theoretically predicted in Ref. [14] and experimentally confirmed in Ref. [15]. Their quasi direct optical behavior has been confirmed by photocurrent[16, 29] and linear absorption (ABS)[17] measurements. The observation of RT Quantum Confined Stark Effect (QCSE)[18, 19] indicates that Ge/SiGe QWs can be applied in optical modulators; indeed designs for modulators based on these system have been proposed in Refs. [20 - 22]. Moreover, a huge dynamical Stark shift has been recently measured.[23] On the other hand, RT direct emission,[24] optical gain on the fs scale,[25] and RT electroluminescence[26] make these systems potential candidates also for efficient light emitters on Si.
Thus, Ge QWs have attracted great interest as proved by many recent papers on their optical properties (see, e.g., Refs. [15 - 17, 19, 22, 24, 27 - 33]), carrier dynamics (see, e.g., Refs. [23, 25, 34 - 36]), and spin properties (Ref. [37]).

These literature works clearly show that Ge/SiGe QWs with Ge-rich barriers are interesting from both a fundamental and an applicative point of view, and thus deserve a detailed understanding of their excitation, relaxation and recombination processes. The fundamental interest for these systems lies in the fact that Ge QWs can be considered a model quasi-direct system; we will show that Ge/SiGe QWs with Ge-rich barriers are characterized by a rich carrier dynamics and by features in the PL spectra different from those commonly observed in direct gap QWs based on III-V semiconductors. On the other hand, the understanding of recombination processes and carrier dynamics in these systems could also be useful in view of the potential applications of Ge/SiGe QWs in optoelectronics and, in particular, in light emitting devices.

Consequently, the aim of this thesis is a detailed study of the recombination processes and of the carrier dynamics in Ge/SiGe QWs with Ge-rich barriers. The recombination paths and the carrier dynamics of Ge/$Si_{0.15}Ge_{0.85}$ MQWs have been analyzed through optical spectroscopy techniques: time-resolved photoluminescence (TR-PL), continuous wave photoluminescence (CW-PL), optical ABS and ultra-fast pump-probe spectroscopy have all been employed. The

samples studied in this work were grown by *Low-Energy Plasma-Enhanced Chemical Vapor Deposition* (LEPECVD)[38], a state-of-the-art technique which allows to grow Ge-rich heterostructures of high quality on Si substrates at fast grow rates, about one order of magnitude faster than conventional epitaxial growth techniques. The good structural and optical quality of these Ge/SiGe MQWs is further guaranteed by the introduction of a graded virtual substrate between the Si substrate and the active layers and by the strain balancement in the active part of the heterostructure.

This thesis is organised as follows. In Chapter 2 a summary of the structural properties of Ge/SiGe QWs is presented, followed by a review of the literature results concerning their optical properties; these results are at the same time the framework in which our experimental work has been inserted and the reference for the discussion of the experimental results.
Chapter 3 is devoted to a detailed study of the indirect cL1-HH1 recombination between the first L-type conduction confined state (cL1) and the first valence confined heavy hole state (HH1) through CW-PL and decay time measurements. The Chapter opens with a discussion on the origin of the zero-phonon line and on the attribution of phonon replicas, based on literature results and on original experimental data; then, the results of the first detailed study of the decay time of the indirect emission in Ge/SiGe QWs are reported, with particular attention to the dependence of the decay time on QW thickness and lattice temperature.
A thorough study of the direct cΓ1-HH1 emission between the first Γ-type conduction confined state (cΓ1) and the first valence confined heavy hole state (HH1) is presented in Chapter 4. First, the main features of the direct emission are presented through the results of CW-PL measurements: in particular the Stokes shift (SS) values, self-absorption and recombination involving high energy excited states are described and discussed. Then, the dependence of PL spectra on lattice temperature is analyzed in detail and the evidence of the direct gap related recombination at RT is discussed with attention to the different recombination paths carriers follow when the sample is excited resonantly and non resonantly to QW confined states. Finally, the results of TR-PL, of PL as a function of the excitation wavelength and of ultrafast TR pump-probe ABS measurements, are presented. These measurements, performed at the Physics department of the Philipps Universität-Marburg, in Marburg (Germany), under the supervision of Priv. Doz. Sangam Chatterjee, provide evidence of the new and rich carrier dynamics in Ge/SiGe QWs and provide the basic information for the discussion of the relaxation processes of photoexcited carriers.

In Chapter 5 an overall picture of the peculiar carrier dynamics of Ge/SiGe QWs is drawn on the basis of the experimental results obtained in this work: relaxation, thermalization and recombination processes are summarized and their typical time scales are indicated.
Finally, in Appendix A the general properties of QWs are briefly summarized, while the details of the growth technique, the characteristics of the samples and the description of the experimental setups are reported in Appendix B.

# Chapter 2

# Structural and optical properties of Ge/SiGe quantum wells

This Chapter is aimed at providing the framework in which our experimental work has been developed and the basis for the discussion of the original experimental results on Ge/SiGe QWs obtained in this thesis work that will be described in Chapters 3 and 4. Indeed, in the last few years a number of literature works has been devoted to the study of the fundamental optical properties of Ge/SiGe QWs through theoretical calculations and experimental results.[15-36] Furthermore, very recent papers have also opened new directions, such as electrolumnescence[26] or spin polarization[37].

In the first part of the Chapter the structural and electronic properties of SiGe bulk alloys are described. Particular attention is devoted to the effect of the strain on the band structure. In the second part the discussion is focused on compressively strained Ge/SiGe QWs with Ge-rich barriers. First the band alignment, the band offsets and the confined levels of this system are described, then an overview of the fundamental optical properties of these systems is presented, based on recent literature data.

## 2.1 SiGe alloys

In this Section the main structural and electronic characteristics of bulk SiGe alloys are summarized in order to introduce the discussion of Ge/SiGe QW properties that will be presented in the second part of the Chapter. The effect of the strain due to the lattice mismatch typical of SiGe epitaxial structures on the electronic properties of these systems is also shortly presented.

A detailed discussion of the lattice characteristics, band structure and strain of SiGe alloys and SiGe-based systems can be found in different books and papers, such as Refs. [3, 39 - 44].

### 2.1.1 Structural properties

Si and Ge are fully miscible, forming $Si_{1-x}Ge_x$ solid solutions with the Ge fraction $x$ ranging from 0 to 1. Si, Ge and SiGe alloys crystallize in the diamond structure. The corresponding Bravais lattice is the face-centered-cubic (FCC), with the two atoms of the basis occupying respectively the (0,0,0) and ($a$/4,$a$/4,$a$/4) positions, where $a$ is the edge of the cubic cell. The cubic unit cell contains eight atoms and each atom is coordinated to four nearest neighbours arranged at the vertices of a regular tetrahedron (Fig. 2.1).

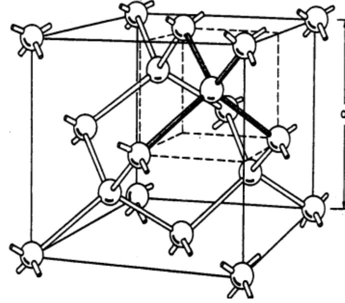


**Figure 2.1:** Diamond crystal structure. Each atom has four nearest neighbours arranged at the vertices of a tetrahedron. [45]

The dependence of the lattice constant of $Si_{1-x}Ge_x$ alloys on the composition is described in first approximation by the Vegard's law [46]:

$$a_x = a_{Si}\,(1-x) + a_{Ge}x\ . \tag{2.1}$$

In Eq. 2.1, that predicts a linear dependence of the alloy lattice constant on the composition, $a_{Si}$ is Si lattice constant ($a_{Si}$ = 0.5431 nm at RT) while $a_{Ge}$ is Ge lattice constant ($a_{Ge}$ = 0.5658 nm at RT)[47]. Slight deviations from the Vegard's law have actually been reported in different theoretical and experimental papers (e.g. Refs. [48 - 50]). A critical summary of this topic can be found e.g. in Ref. [51].

When a $Si_{1-x}Ge_x$ layer is epitaxially grown on a $Si_{1-y}Ge_y$ substrate with different composition, it adapts its lattice constant to that of the substrate (*pseudomorphic growth*). As a consequence, the layer experiments a *structural* strain which is compressive if $x > y$ or tensile if $x < y$. The structural strain is proportional to the *lattice mismatch*, i.e. to the difference between the lattice constant of the epilayer and that of the substrate. As the thickness of the strained epilayer increases, the elastic energy stored rises, with a linear dependence between the energy stored and the thickness.[42] The system may relieve the strain lowering its total free energy by means of the nucleation of dislocations. These extended defects relieve the strain, reducing the whole energy of the system, and their nucleation requires a minimum energy. Thus there is a film thickness, called *critical thickness*, over which the introduction of dislocations in the epilayer becomes favorable.[52]

The thermal expansion coefficients of bulk Si and Ge are reported in Fig. 2.2 as a function of the lattice temperature in the 0 - 1000 K range. The expansion coefficient of Ge is higher than that of Si in the whole temperature range, and this implies that the same temperature reduction causes a higher lattice contraction in Ge than in Si. Extending the discussion to SiGe alloys, the dependence of their expansion coefficient on T is expected to be intermediate between those of Ge and Si, depending on the composition. Let us consider the case of a $Si_{1-x}Ge_x$ layer epitaxially grown on a $Si_{1-y}Ge_y$ substrate. At the growth temperature the epilayer adapts its lattice constant to that of the substrate, as previously described. Cooling the heterostructure to RT, the epilayer and the substrate lattices contract at a different rate. As a consequence, a *thermal* strain appears in the epilayer which adds to the structural one. The amount of thermal strain depends on the temperature variation and on the composition of the epilayer and of the substrate.

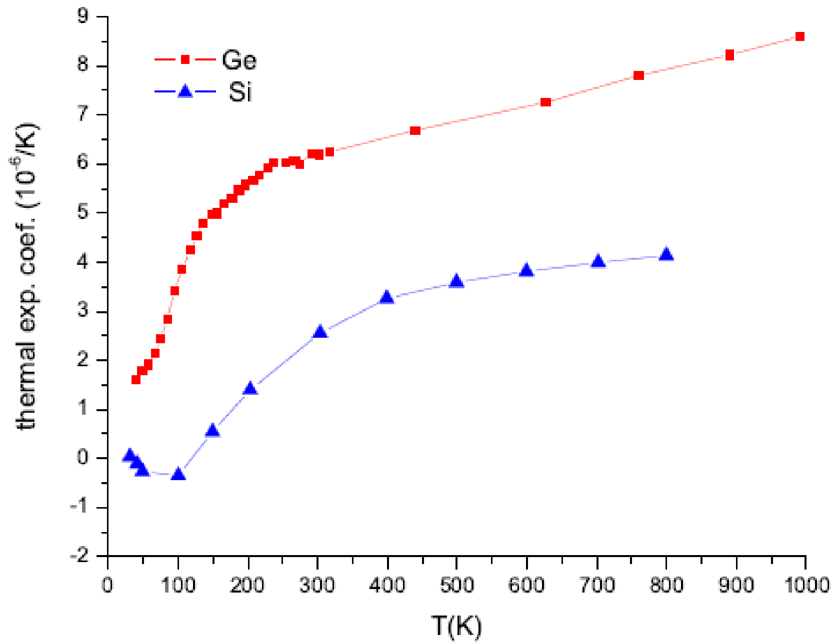


**Figure 2.2:** Thermal expansion coefficients of bulk Si and Ge between 0 and 1000 K.[53 - 55]

### 2.1.2 Electronic properties

The band structure of bulk Si and Ge at RT is reported in Fig. 2.3(a). The fundamental band gap is indirect for Si as well as for Ge. In both cases, the top of the valence band (VB) is located at the centre of the Brillouin zone (Γ point). It consist of three degenerate bands, the *heavy hole* (HH), the *light hole* (LH) and the *split-off* (SO). The degeneracy is partially removed by the spin-orbit interaction that shifts the SO band towards lower energies. For $\boldsymbol{k}$ = 0 VB states transform with the same symmetry of atomic $p$ orbitals. In Si the minimum of the

conduction band (CB) is along the Δ (<100>) direction of the Brillouin zone, 15 % away from the X point. Thus in Si there are six equivalent conduction valleys (Fig. 2.3(b)). The fundamental indirect gap energy in Si is $E_{g,ind}$ = 1.12 eV at RT. The Si CB presents also a local minimum at Γ, about 4.06 eV above the VB maximum at RT. In Ge the minimum of the CB is at the L (111) point, at the edge of the Brillouin zone. Thus in Ge there are eight equivalent half-valleys (Fig 2.3(b)). The indirect gap energy in Ge is $E_{g,ind}$ = 0.66 eV at RT. A local minimum at Γ is also present. The local minimum at Γ is $E_{g,dir}$ = 0.80 eV above the VB maximum at RT. As a consequence, the energy difference between the direct and the indirect gap in Ge at RT is 140 meV only. CB states at Γ are *s*-like for both Si and Ge.

The direct and indirect $E_g$ values for bulk Si and Ge at RT and at 0 K are summarized in Table 2.1.

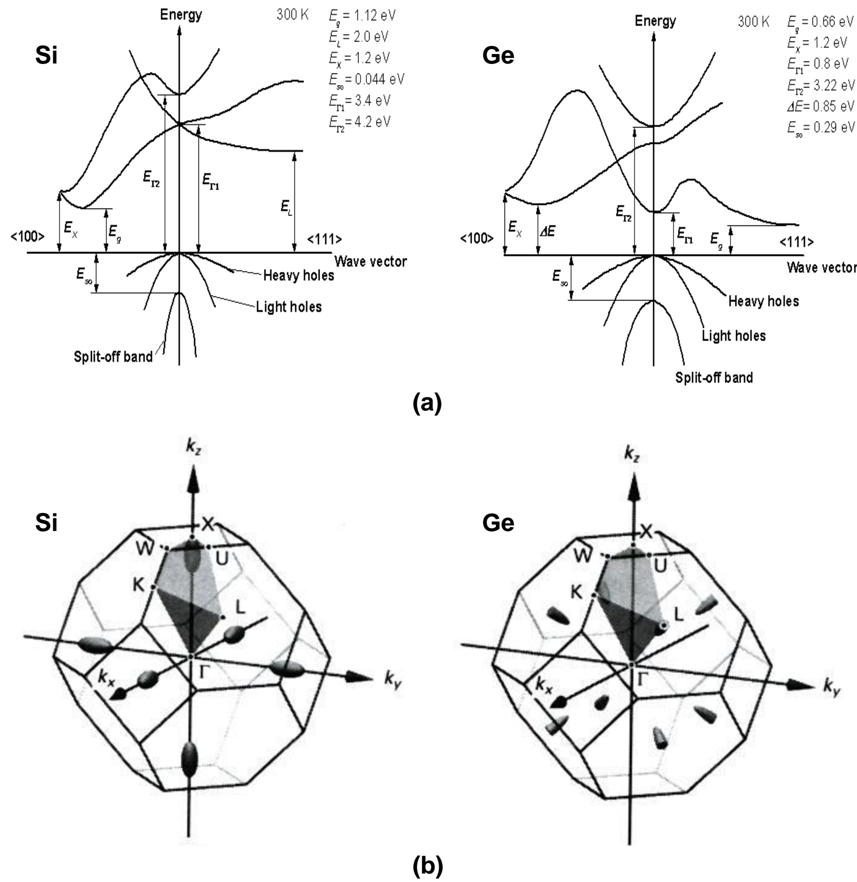


**Figure 2.3:** **(a)** Band structure of bulk Si and Ge at RT. Energy gap values and split-off energy are reported. **(b)** Many valley structure of Si and Ge [56].

| | | Si | Ge |
|---|---|---|---|
| **$E_{g,dir}$** | **0 K** | 4.18 eV | 0.89 eV |
| | **300 K** | 4.06 eV | 0.80 eV |
| **$E_{g,ind}$** | **0 K** | 1.17 eV | 0.74 eV |
| | **300 K** | 1.12 eV | 0.66 eV |

**Table 2.1:** $E_{g,dir}$ and $E_{g,ind}$ values of bulk Si and Ge at 0 K and 300 K. The values of $E_{g,dir}$ of Si have been taken from Ref. [57]; all the others are reported in Ref. [47].

In Fig. 2.4 the indirect and direct band gap values of SiGe alloys are reported as a function of the the Ge content $x$ at LT. A monotonic decrease from the Si to the Ge bulk value (Table 2.1) is found for both the indirect and direct band gap. The direct band gap energy presents a very steep linear dependence on the Ge content $x$ described by [58]

$$E_{g,dir} = 4.185 - 3.296x \text{ eV}. \tag{2.2}$$

The indirect gap is Si-like, with the CB minimum along the Δ direction for $x < 0.85$, while it becomes Ge-like, with the CB minimum at the L point for $x > 0.85$. The dependence of the excitonic indirect gap $E_{g,ind}^{exc}$ on $x$ is parabolic in the former range and linear in the latter, as described by the following relationships obtained by Weber and Alonso form LT PL measurements[58]:

$$E_{g,ind}^{exc} = 1.155 - 0.43x + 0.206x^2 \text{ eV} \quad \text{for } x < 0.85 \tag{2.3a}$$

$$E_{g,ind}^{exc} = 2.010 - 1.270x \text{ eV} \quad \text{for } x > 0.85. \tag{2.3b}$$

The Si, Ge and SiGe alloy band structure is described in detail e.g. in Ref. [56].

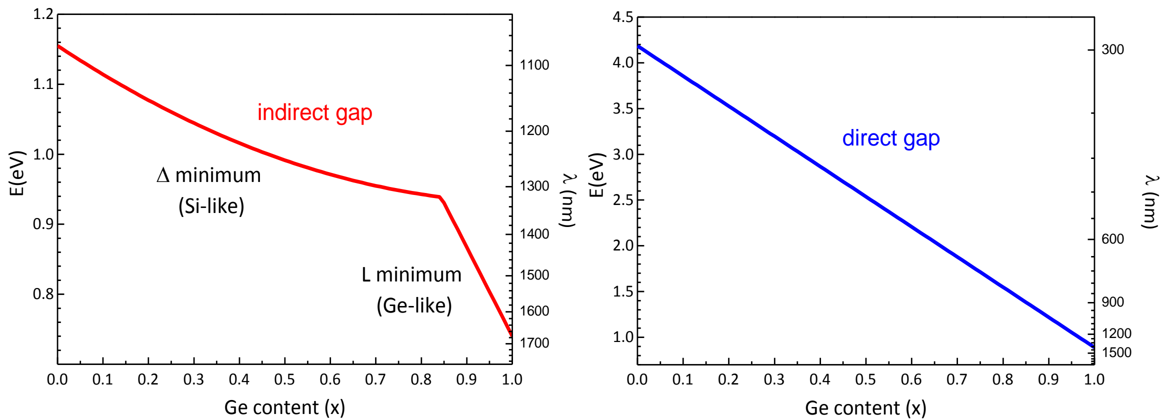


**Figure 2.4:** Indirect (left) and direct (right) band gap of $Si_{1-x}Ge_x$ alloys as a function of the Ge content at LT. Data have been taken respectively from Refs. [58 - 60].

In bulk semiconductors the dependence of $E_g$ on the temperature is described by the empirical Varshni law:

$$E_g(T) = E_g(0) - \frac{\alpha T^2}{\beta + T}, \quad (2.2)$$

where α and β are parameters typical of each semiconductor and $E_g(0)$ is the energy gap value at 0 K.[61] The values of α and β for bulk Si and Ge are reported in Table 2.2.

| | **Si** | **Ge** |
|---|---|---|
| **α (direct gap)** | | $6.5 \cdot 10^{-4}$ eV/K |
| **β (direct gap)** | | 410 K |
| **α (indirect gap)** | $4.73 \cdot 10^{-4}$ eV/K | $4.77 \cdot 10^{-4}$ eV/K |
| **β (indirect gap)** | 636 K | 235 K |

**Table 2.2:** α and β Varshni's parameters of bulk Si and Ge.[28, 47] To the best of our knowledge, no values are available in the literature for the Si direct gap.

At the end of this Section the effects of the strain on the band structure of SiGe alloys are analyzed. As a matter of fact, the strain modifies the energy and the curvature of the bands and breaks the degeneracies, causing relevant changes in the electronic and optical properties of the alloys.

If a $Si_{1-x}Ge_x$ layer is grown on a $Si_{1-y}Ge_y$ substrate, it experiments a biaxial strain, which is compressive in the plane and tensile in the growth direction if $x > y$, and tensile in the plane and compressive in the growth direction if $y > x$.

A biaxial deformation can be decoupled into two components: hydrostatic and uniaxial. The isotropic *hydrostatic* component induces a shift of the conduction and valence levels, yielding a variation of the energy gaps. As an example, in the case of bulk Ge both the direct and the indirect band gaps decrease if a tensile strain is applied, and increase in the opposite case.[10] The anisotropic *uniaxial* component is responsible for the splitting of degenerate levels, e.g. HH and LH states at the top of the VB, or conduction minima at Δ in Si-rich alloys. L and Γ conduction minima are not affected by the uniaxial component.[62] The effects of the two components are schematically shown in Fig. 2.5 for a $Si_{1-x}Ge_x$ alloy with $x > 0.85$ (CB absolute minimum at L).

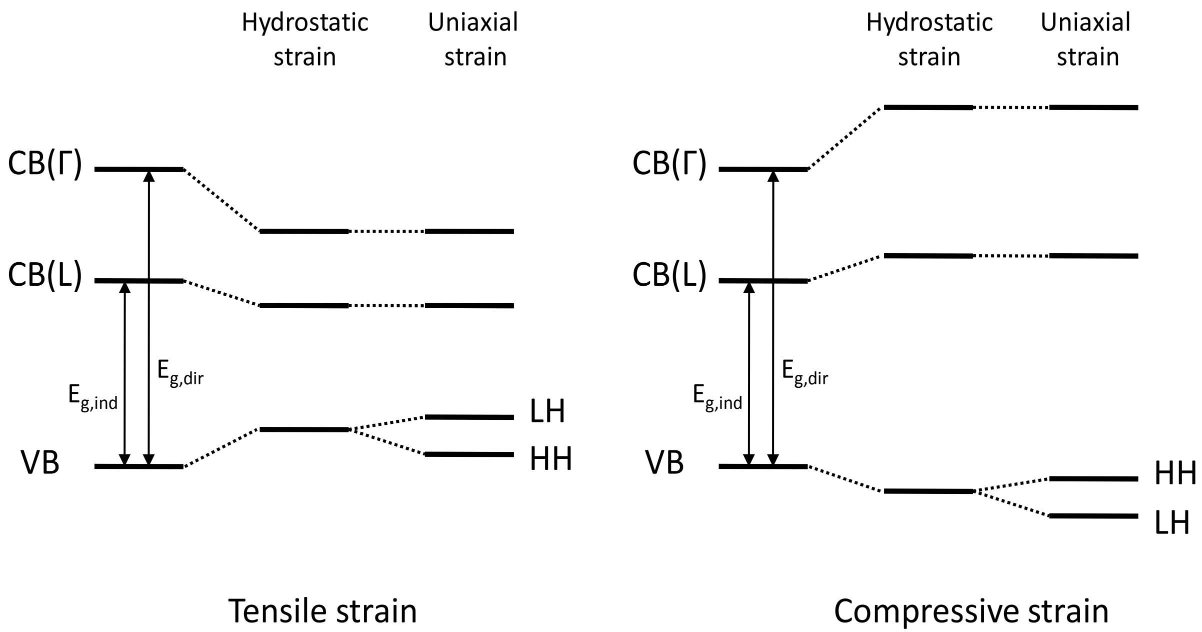


**Figure 2.5** Scheme of the effects of tensile and compressive strain on a $Si_{1-x}Ge_x$ alloy with $x > 0.85$. The effects of the hydrostatic and uniaxial strain components are shown separately.

The effect of compressive and tensile strain on the direct gap of bulk Ge is shown in Fig. 2.6. The role of the two components is clearly visible: under compressive strain the energy gap increases and the top of the VB present an HH character; under tensile strain a decrease of the energy gap is observed and the LH state characterizes the top of the VB.

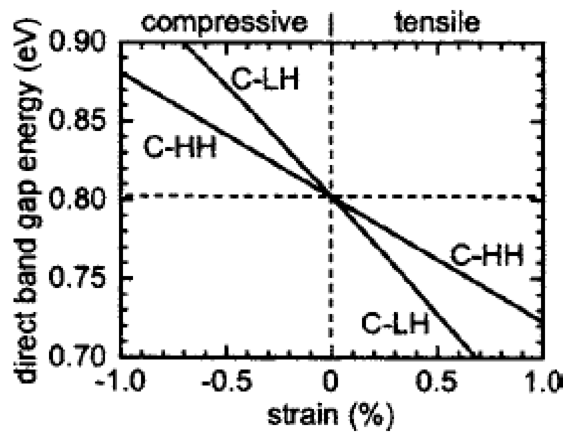


**Figure 2.6:** $E_{g,dir}$ of bulk Ge as a function of tensile and compressive strain. The splitting of HH and LH levels is also considered. [63]

As far as the indirect gap is concerned, the nature of the CB absolute minimum depends not only on the composition, but also on the strain (see, e.g., Fig. 2.7(a) in Section 2.2). Three regions can be identified: for high Ge concentration the CB absolute minimum is at the L point of the Brillouin zone. For Si-richer compositions under tensile strain a $\Delta_{\perp}$ minimum is found (i.e. the $\Delta$ points along direction perpendicular to the interface plane are characterized by the lower energy); on the other hand, if a compressive strain is applied the CB is characterized by a $\Delta_{||}$ minimum.[14, 40]

## 2.2 Band alignment and band structure of Ge/SiGe quantum wells

The fundamental energy gap, the band offsets and the band alignment of a $Si_{1-x}Ge_x$ active material on a $Si_{1-y}Ge_y$ substrate have been calculated in Ref. [14] for the whole composition range ($0 \leq x, y \leq 1$) and are reported in Fig. 2.7. In this calculation, based on the tight-binding method, it is assumed that the substrate is relaxed while the active material layer is pseudomorphically grown on the substrate, and consequently strained. This thesis work is devoted to the study of Ge/SiGe QWs with Ge-rich barriers ($y = 0.85$), and thus the present discussion will summarize the results related to this system only. In particular we will associate the substrate with the barrier layer and the active material with the well layer.

As shown in Fig. 2.7(a), the character of the fundamental energy gap of the active layer depends on $x$ and $y$; in the case of strained Ge QWs embedded in barriers with Ge content higher than 0.4, the fundamental energy gap in the well layer involves the conduction minimum at L. In Fig. 2.7(b) and 2.7(c) the band offset values are plotted for the CB and the VB respectively. The positive value reported in Fig. 2.7(b) for the compositions of interest indicates that the L minimum of the CB in the Ge well is lower in energy respect to that of the $Si_{0.15}Ge_{0.85}$ barriers. On the contrary, the negative value of Fig. 2.7(c) allows to conclude that the VB maximum in the Ge well is higher in energy respect to that of the $Si_{0.15}Ge_{0.85}$ barriers. These offset values give the type-I band alignment sketched in Fig 2.7(d) for the indirect gap of Ge/$Si_{0.15}Ge_{0.85}$ QWs: both electrons and holes are confined in the same spatial region (see Section A.1), i.e. in the Ge well. The type I band alignment has been experimentally proved in Ref. [15], as it will be discussed in Section 2.3.4.

Finally, it should be specified that in the Ge/SiGe QW samples analyzed in this work, both well and barrier layers are actually strained because they adapt their lattice constant to that of the final layer of the GVS (see Section B.1.2), while in the calculations summarized in Fig.

2.7 the barriers are assumed to be relaxed. Anyway, since the composition of the barriers ($Si_{0.15}Ge_{0.85}$) and that of the final layer of the VGS ($Si_{0.10}Ge_{0.90}$) are close, the tensile strain in the barriers is such that, for the band offset calculation, barriers can be reasonably assumed, to a first approximation, as relaxed.

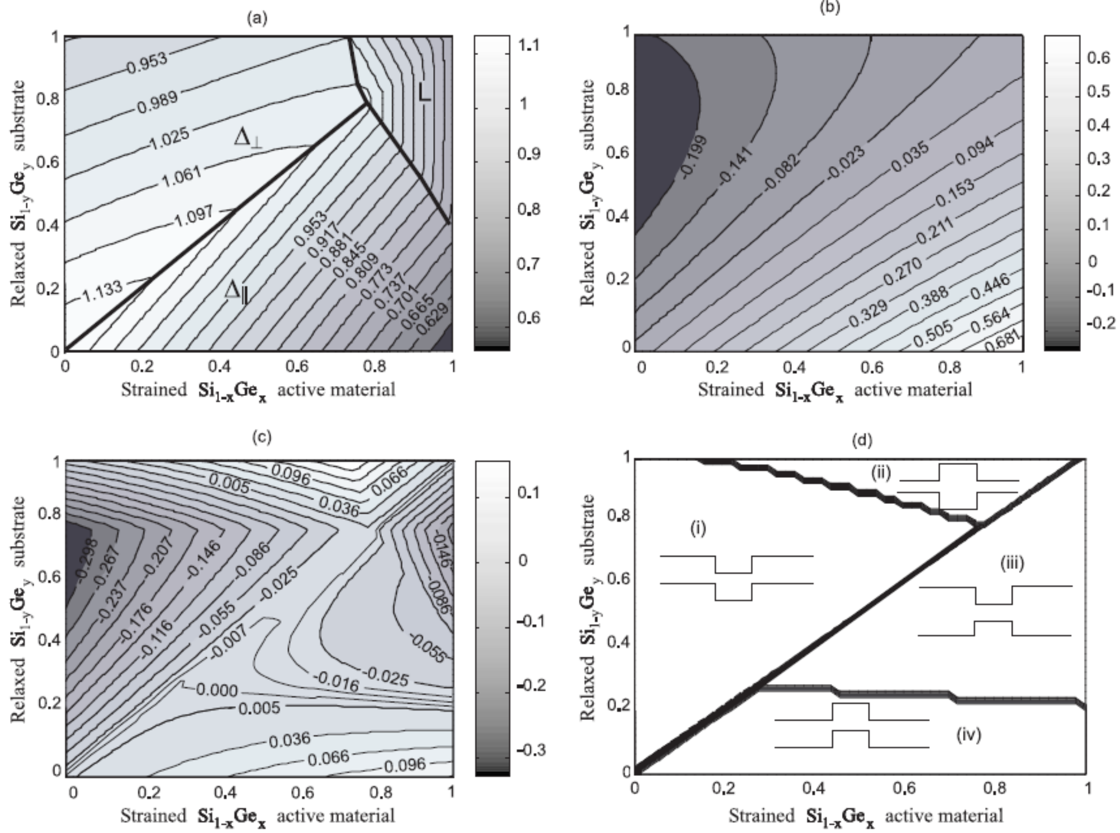


**Figure 2.7:** Fundamental energy gap **(a)**, CB offset **(b)**, VB offset **(c)** and resulting band alignment **(d)** for a strained $Si_{1-x}Ge_x$ QW between relaxed $Si_{1-y}Ge_y$ barriers as a function of $x$ and $y$ in the whole range of compositions. Energies are in eV. [14]

The complete LT band structure of $Ge/Si_{0.15}Ge_{0.85}$ QWs on a $Si_{0.10}Ge_{0.90}$ VS has been calculated via the tight-binding method by M. Virgilio and G. Grosso: their results are reported in Ref. [15]. As an example, the results for a 10 nm thick QW with 23 nm thick barriers are reported in Fig. 2.8, where VB and CB offsets are also shown. A type-I band alignment is predicted not only for the indirect band gap, as previously discussed, but also for the direct band gap involving the conduction band minimum at Γ. The large band offset for the Γ conduction minimum (about 400 meV) is due to the steep rise of the direct energy gap as the Si content of the SiGe alloy increases (see Section 2.1, Fig. 2.4). The L minimum band offset is about 150 meV. Since the composition of the substrate is intermediate between those of the barriers and of the wells (see Section B.1.2), Ge well layers experiment a compressive

strain, while $Si_{0.15}Ge_{0.85}$ barriers are slightly tensile strained. As a consequence, HH and LH levels are not degenerate in both the well and the barrier layers (see Section 2.1), but with different valence top characters (see Fig 2.9). A band offset of about 80 meV for the HH band (red line in Fig. 2.8) and of about 20 meV for the LH band (green line in Fig. 2.8) results. The type-I band alignment is anyway found in both the cases.

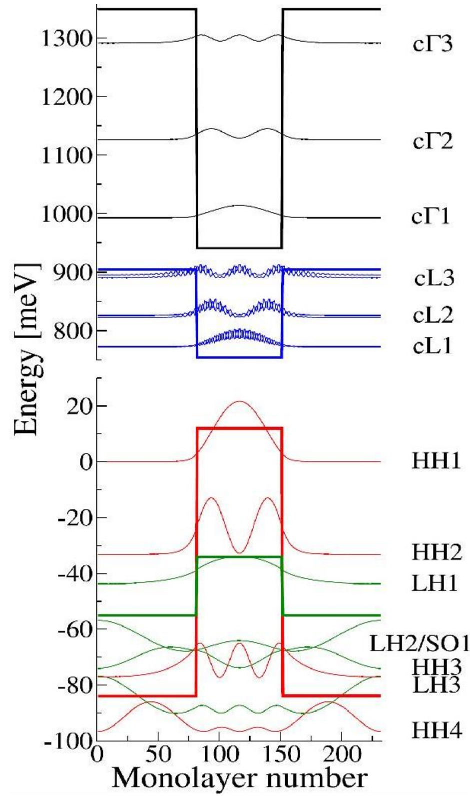


**Figure 2.8:** Calculated band offsets and square modulus of the wavefunctions of electron and hole confined states for a $Ge/Si_{0.15}Ge_{0.85}$ 10 nm thick QW. [15]

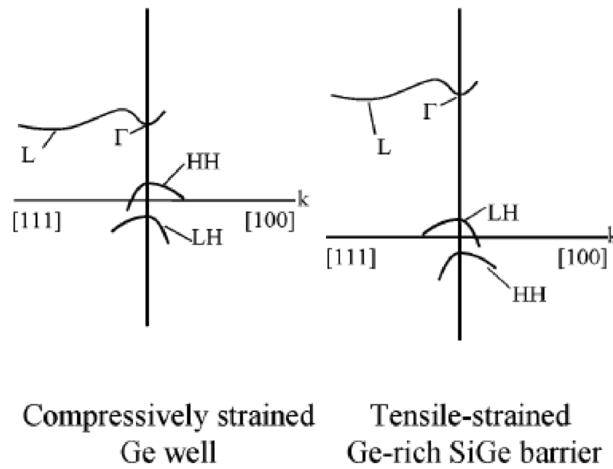


**Figure 2.9:** Sketch of the band structure of compressively-strained Ge well and tensile-strained Ge-rich SiGe barrier layers. [64]

In Fig. 2.8 the square modulus of the wavefunctions of electron and hole confined states is also reported. For the first confined states (HH1, cL1, cΓ1), the wavefunction is nearly fully confined inside the well region. As the levels approach the top of the potential barrier, the wavefunction penetration into the barriers increases, as expected.

Finally, an example of the extended dispersion curves calculated via tight-binding for Ge/$Si_{0.15}Ge_{0.85}$ QWs is reported in Fig. 2.10. [30]

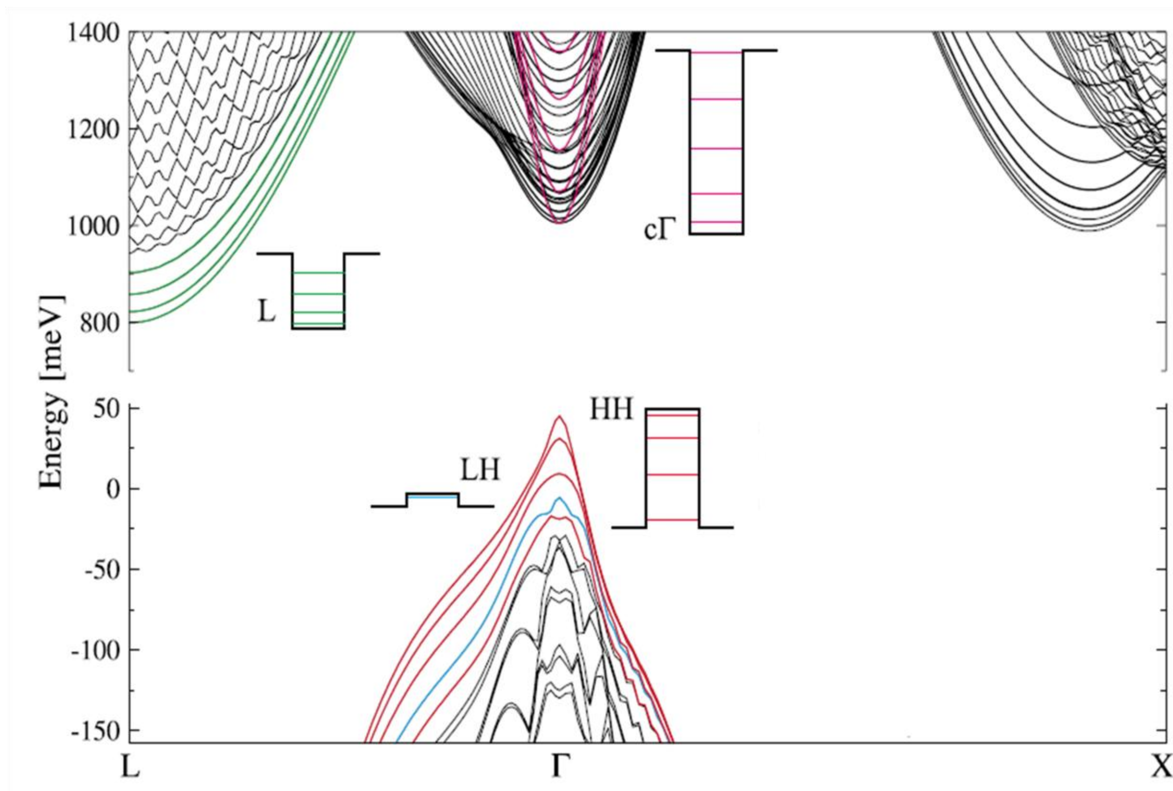


**Figure 2.10:** Dispersion relations calculated via tight-binding for Ge/$Si_{0.15}Ge_{0.85}$ QWs. QW conduction subbands close to the L (green) and Γ (violet) points are reported. Subbands in the VB are shown in red (HH) and blue (LH). The bulk band edge profiles are sketched together with the energies of the states at the L and Γ points. [30]

The band structure of Ge/$Si_{0.15}Ge_{0.85}$ QWs has been calculated also in Ref. [16] via six-band **k·p** method and in Ref. [22] via a combined 6x6 **k·p** and one-band effective mass modelling tool, with results analogous to those shown in Figs. 2.8 and 2.10.

## 2.3 Optical properties of Ge/SiGe quantum wells

### 2.3.1 Absorption

In the recent years different literature works have been devoted to the optical ABS of Ge/SiGe QWs, such as Refs. [15 - 17, 29, 30, 32, 33], with analogous results. In the first part of this Section, we will refer mainly to Ref. [15].

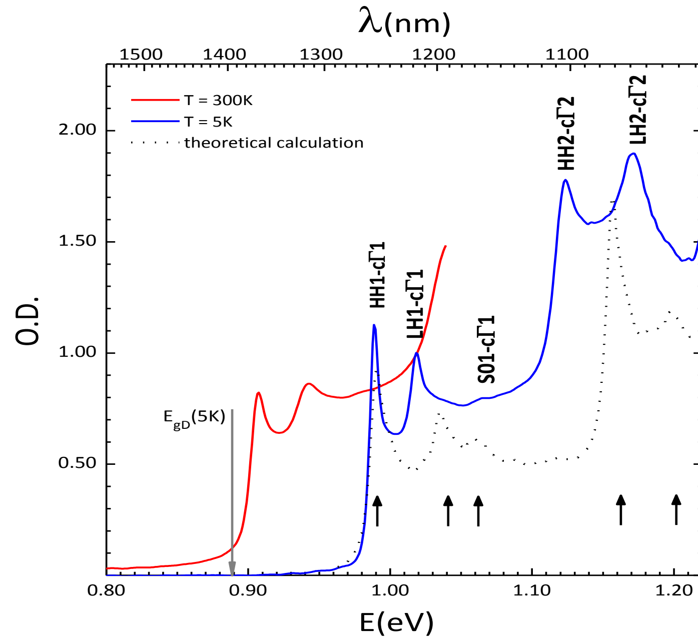


**Figure 2.11:** Experimental ABS spectra of 200 Ge/$Si_{0.15}Ge_{0.85}$ QWs with $L_z$ = 9.9 nm at 300 K (red line) and 5 K (blue line). The calculated LT ABS spectra including excitonic effects (dotted black line) and the transition energies deduced from the band structure (black arrows) are also shown. [15] The direct energy gap value for bulk relaxed Ge at 5 K is reported as a reference (grey arrow).

Typical RT and LT ABS spectra of Ge/$Si_{0.15}Ge_{0.85}$ MQWs are reported in Fig. 2.11 ($L_z$ = 10 nm, 200 QWs).[15] The spectra reproduce the staircase shape of the DOS typical of direct gap semiconductor QWs with type-I band alignment (see Section A.2). [65, 66] Sharp peaks due to confined excitons are visible at the edge of each step even at RT. Let us consider the LT spectrum first. The absorption edge is blue shifted respect to the direct energy gap of bulk Ge (grey arrow), due to the confinement (see Section A.2) and the compressive strain in Ge well layers (see Section 2.2). The theoretical spectrum, that includes excitonic effects, calculated from the band structure reported in Fig 2.8, is also shown by the dotted line. The comparison between the experimental and the calculated spectrum allows to attribute the ABS peaks to dipole allowed HH*n*-cΓ*n*, LH*n*-cΓ*n* and SO*n*-cΓ*n* transition between confined states at Γ with

the same subband index $n$ (see labels in Fig. 2.11). The optical coupling between subbands with different indices is indeed suppressed by parity selection rules.[17]

Since the fraction of light absorbed per well does not depend on QW thickness, optical absorption normal to the plane of MQW structures is usually expressed as *(number of wells)*$^{-1}$ and not as absorption coefficient in cm$^{-1}$. [19, 67, 68]

Rising the temperature from 5 to 300 K the spectrum is red shifted accordingly to Varshni's law (see Section 2.3.2) and the FWHM of the HH1-cΓ1 peak broadens following the relation reported in Ref. [29].

The first evidence of indirect gap related ABS between confined valence states at Γ and confined conduction states at L in Ge/SiGe QWs has been recently reported in Ref. [32], where an absorption coefficient about 3 orders of magnitude lower than that for the direct transitions is evaluated, in agreement with typical results for bulk Ge.[47] Direct gap related transitions dominate the ABS spectra, and thus Ge QWs are commonly told to show a *pseudo-direct* optical behavior.

ABS selection rules in QW systems for light propagating along and perpendicularly to the QW plane and for different linear polarizations have been calculated in literature works, e.g. in Refs. [69] and [70]. In table 2.3 the dipole matrix elements for direct gap related transitions involving respectively HH and LH valence states are reported for all the possible combinations of light propagation and linear polarization direction.

| | $\varepsilon_x$ | $\varepsilon_y$ | $\varepsilon_z$ | Transition |
|---|---|---|---|---|
| Propagation parallel to $z$ | $\frac{\pi}{\sqrt{2}}$ | $\frac{\pi}{\sqrt{2}}$ | *impossible* | HH$n$-cΓ$n$ |
| Propagation parallel to $x$ | *impossible* | $\frac{\pi}{\sqrt{2}}$ | *forbidden* | HH$n$-cΓ$n$ |
| Propagation parallel to $y$ | $\frac{\pi}{\sqrt{2}}$ | *impossible* | *forbidden* | HH$n$-cΓ$n$ |
| Propagation parallel to $z$ | $\frac{\pi}{\sqrt{6}}$ | $\frac{\pi}{\sqrt{6}}$ | *impossible* | LH$n$-cΓ$n$ |
| Propagation parallel to $x$ | *impossible* | $\frac{\pi}{\sqrt{6}}$ | $\frac{2\pi}{\sqrt{6}}$ | LH$n$-cΓ$n$ |
| Propagation parallel to $y$ | $\frac{\pi}{\sqrt{6}}$ | *impossible* | $\frac{2\pi}{\sqrt{6}}$ | LH$n$-cΓ$n$ |

**Table 2.3:** Selection rules for interband transitions at Γ involving HH and LH valence states, obtained from the absolute value of transition matrix elements as calculated in Ref. [69]. The direction $z$ is perpendicular to the QW plane, while the directions $x$ and $y$ are parallel to it. $\varepsilon_x$, $\varepsilon_y$, and $\varepsilon_z$ indicate linear polarization along the $x$, $y$, $z$ directions, respectively.

When light propagates along the *z* direction, i.e. perpendicular to the QW plane, equal ABS is obtained for polarization along the *x* and *y* direction. On the other hand, light propagating parallel to the QW plane, e.g. in the *x* direction, can have two possible polarizations: parallel to the QW plane, i.e. along *y* (*TE mode*), and perpendicular to the QW plane, i.e. along *z* (*TM mode*). The selection rules reported in Tab. 2.3 show that no HH*n*-cΓ*n* transitions can be observed in the TM mode, while LH*n*-cΓ*n* transitions occur for both the possible polarizations, although the matrix element is twice larger for the TM mode than for the TE mode.

These selection rules have been verified on Ge/SiGe MQWs through ABS measurement as a function of the polarization and through the comparison with theoretically predicted spectra in Refs. [30] and [68]. The experimental configuration is schematically shown at the top of Fig. 2.12.

The experimental and calculated spectra for TE and TM polarised light are reported at the bottom of Fig. 2.12. The HH-related transitions are markedly suppressed in the TM mode, while ABS peaks due to LH*n*-cΓ*n* transitions are not affected by the polarization of the incoming light, as suggested by the selection rules. Moreover, the O.D. values of the HH1-cΓ1 and LH1-cΓ1 transitions are compatible with those expected from the matrix element reported in Tab. 2.3, taking into account also the geometry of the experimental system, as discussed in detail in Refs. [30] and [68].

In conclusion, TE/TM absorption measurements have provided an experimental confirmation of the ABS selection rules; this further proves the attribution of ABS features to HH*n*-cΓ*n* and LH*n*-cΓ*n* transitions. Moreover, the fact that selection rules for type-I direct gap semiconductors have also been confirmed for Ge QWs, further indicates the quasi direct behavior of these systems.

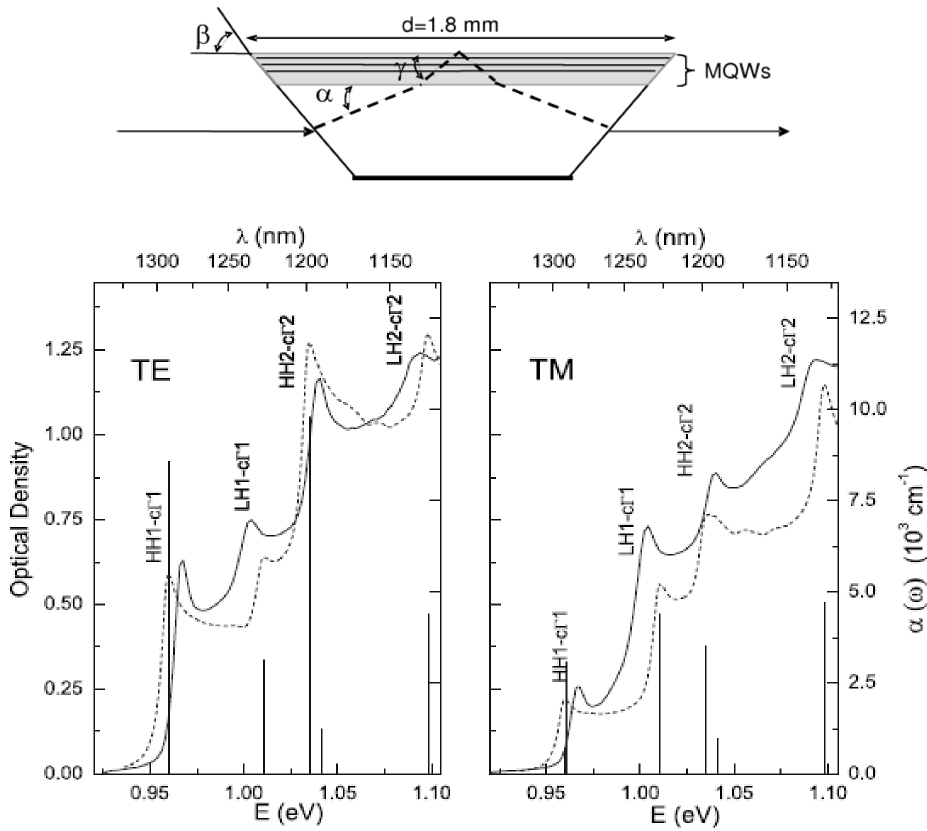


**Figure 2.12:** Top: experimental configuration for ABS measurements in polarized light: the arrows show the optical path of the transmitted light. Bottom: calculated (dashed lines) and experimental (full lines) ABS spectra for TE and TM polarized light at the lattice temperature of 5 K.[30]

### 2.3.2 Temperature dependence of absorption spectra

The dependence of the HH1-cΓ1 excitonic peak energy of Ge QWs on the lattice temperature is reported in Fig. 2.13(a) (squares).[29] As the temperature rises the peak follows the red shift of the direct gap of bulk Ge described by Varshni's law. This proves that the temperature dependence of the optical gap of Ge QWs is not affected by strain and confinement effects in the 5 - 300 K range within the experimental error.

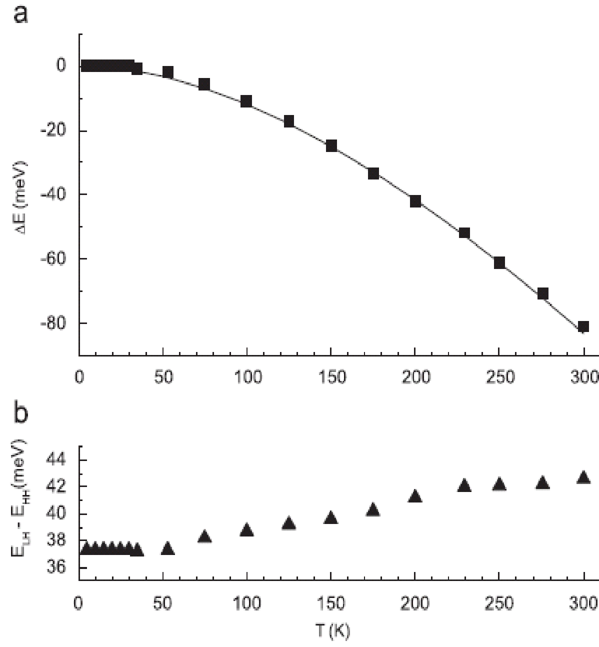


**Figure 2.13:** (**a**) Dependence of the HH1-cΓ1 ABS peak energy on the lattice temperature for Ge/$Si_{0.15}Ge_{0.85}$ MQWs (squares). Varsnhi's law for the direct gap of bulk Ge (Eq. 2.2 with parameters of Tab. 2.1) is also reported as a full line. (**b**) Dependence of the energy distance between the LH1-cΓ1 and the HH1-cΓ1transition as a function of lattice temperature.[29]

In Fig. 2.13(b) the energy distance between LH1-cΓ1 and HH1-cΓ1 excitonic peaks is reported as a function of temperature. Reducing the temperature from 300 to 5 K, the energy distance slightly reduces, by about 5 meV. This is caused by an increase of the tensile thermal strain in Ge QW as the temperature gets lower, due to the mismatch between the expansion coefficients of the Si substrate and the Ge/SiGe QWs (see Section 2.1). The tensile thermal strain partially compensates the compressive structural strain, giving rise to a reduction of the energy spacing between HH1 and LH1 confined states.

### 2.3.3 Quantum Confined Stark Effect

The QCSE is defined as the change of the ABS edge of a QW system in response to an electric field applied along the growth direction. As schematically sketched in Fig. 2.14, the applied electric field causes a band bending, resulting in a tilted QW. This has two main consequences: a reduction of the optical gap and a decrease of the superposition between electron and hole wavefunctions. As a final effect, the ABS edge is reduced, broadened and red-shifted.[69]

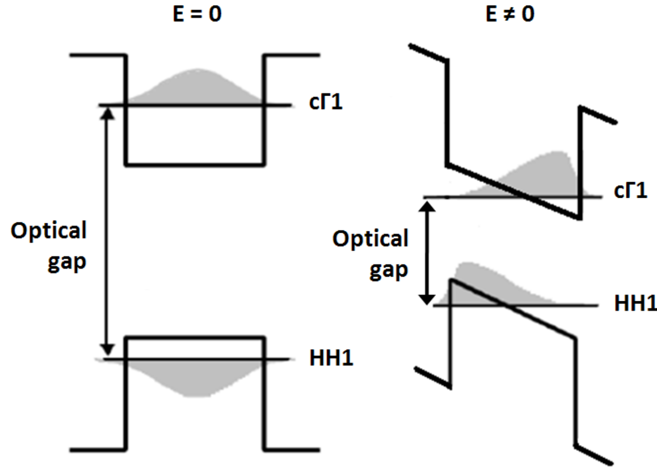


**Figure 2.14:** Schematic sketch of the effect on the QW band structure of an electric field **E** applied along the growth direction. In presence of the electric field, the optical gap is reduced and the electron and hole wavefuntions are pulled towards opposite directions, yielding a decrease of their superposition.

As previously discussed, the QCSE enables QW systems to be used as high-performance modulators, characterized by low dimensions and low power dissipation. A strong QCSE on QWs made of III-V semiconductors like GaAs and InP is reported in different literature works, [71 - 73] and indeed these systems are already used in devices.

An efficient QCSE in strain balanced Ge/SiGe QWs at RT has been demonstrated for the first time in Ref. [18] through photocurrent measurements (see Fig. 2.15). At a 0 V bias the spectrum reproduces the features of interband ABS described in Section 2.3.1. Rising the potential from 0 to 4 V both the HH1-cΓ1 and the LH1-cΓ1 peaks undergo a red-shift of about 30 meV. The effective absorption coefficient at the HH1-cΓ1 excitonic peak reduces from $6{\cdot}10^{-3}$ to $3{\cdot}10^{-3}$ $cm^{-1}$. This values are comparable with those obtained for III-V QWs (see, e.g., Ref. [74] for InGaAsP/InP QWs and Refs. [71, 75] for GaAs/AlGaAs QWs). Moreover, they demonstrate that an efficient QCSE may be obtained in a spectral region close to the C band used in telecommunications (about 0.8 eV = 1550 nm) in a system which is compatible with the CMOS technology.

The results presented in Ref. [18] have been confirmed by different theoretical[22, 64, 76] and experimental[20, 21] literature works. A clear QCSE has been reported also for Ge/SiGe MQWs analogous to those analyzed in this work through photocurrent[16] and optical ABS[19] measurements.

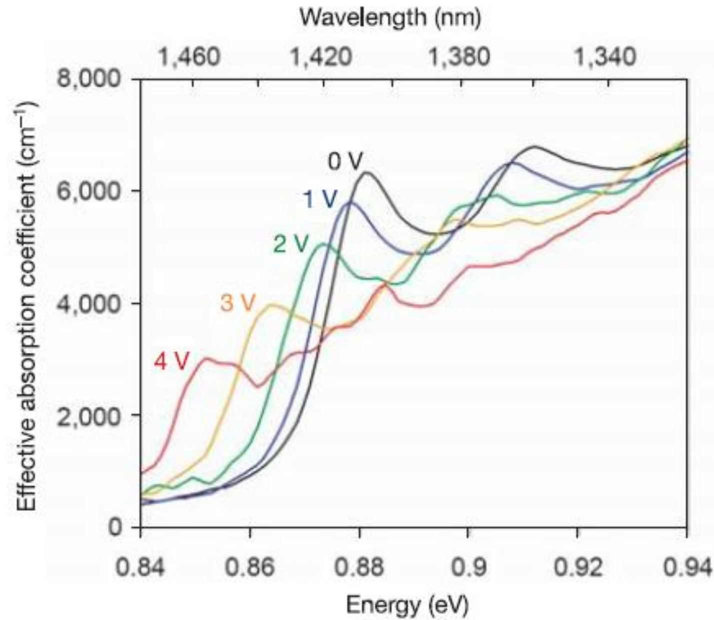


**Figure 2.15:** RT ABS spectra deduced from photocurrent measurement on Ge/SiGe MQWs (10 periods). A strong QCSE is observed: applying a bias from 0 to 4 V, the absorption peaks red shift, broad and reduce.[18]

### 2.3.4 Continuous wave photoluminescence

In this Section a short presentation of the main features of the CW-PL spectra of Ge/SiGe MQWs at LT is provided. A detailed discussion of the direct and indirect emission will be carried out in the first Section of Chapters 3 and 4 respectively.

A typical LT PL spectrum of Ge/SiGe QWs is reported in Fig. 2.16. Three regions can be identified. A comparison between ABS and PL spectra allows to attribute the emission peak at about 0.97 eV to the direct gap related transition cΓ1-HH1 from the first confined conduction state at Γ to the first heavy hole confined valence state. The peak at about 0.78 eV is attributed to the zero-phonon line of the indirect cL1-HH1 transition between the first confined CB state at L and the HH1 level. The peak and shoulders between 0.74 and 0.77 eV are attributed to phonon replicas of the cL1-HH1 transition[15] (for a detailed discussion, see Section 3.1). At lower energies (0.6 - 0.7 eV), emission related to defects (mainly dislocations) is visible, as confirmed by the comparison with PL results obtained on bulk SiGe alloys. [68, 77]

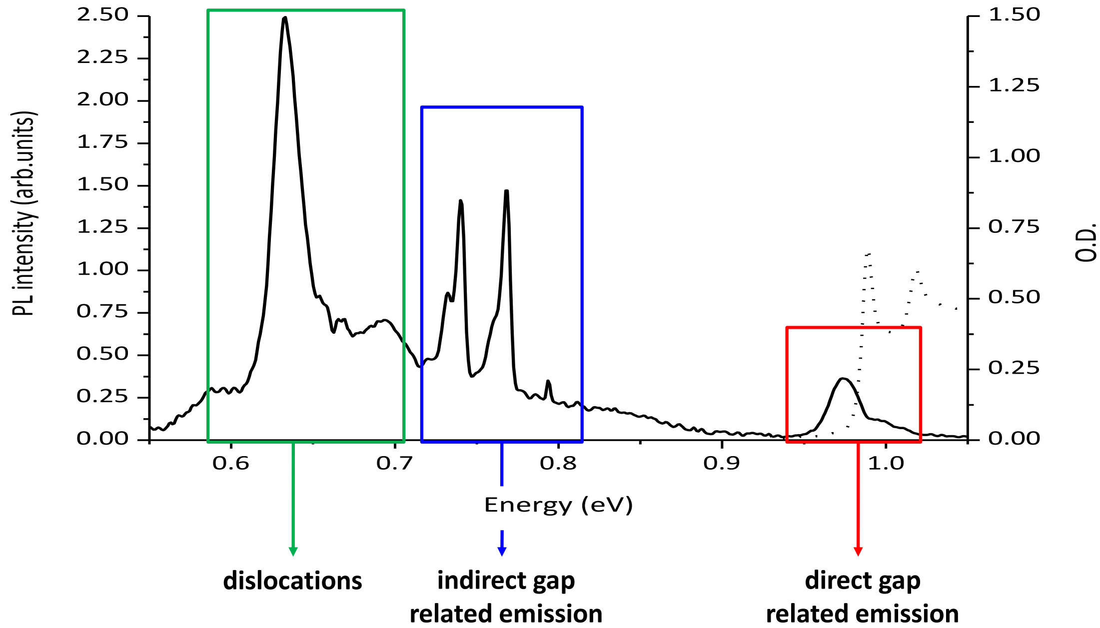


**Figure 2.16:** Typical LT PL spectrum of Ge/SiGe MQWs (sample 7864-E10: 200 QWs, $L_z$ = 9.9 nm). The LT ABS spectrum is also reported (dotted line).[68]

The fact that both direct and indirect transition are visible in the same PL spectrum is due to the proximity between $E_{g,dir}$ and $E_{g,ind}$ in Ge (see Section 2.1) and also to the higher recombination rate for the direct transition that allows to observe the cΓ1-HH1 transition even if carrier dynamics favors the population of L- type states (see Section 2.3.5).

In Fig. 2.17 the energy peak of the cL1-HH1 zero-phonon line and of its phonon replica is reported as a function of the energy of the cΓ1-HH1 emission. A linear dependence is shown. As the QW thickness decreases, the energy distance between the two transition increases, since L states are less sensitive to changes in the QW width than the Γ ones. Moreover, the good agreement between experimental and calculated data (full and open symbols respectively) not only confirms the attribution of the PL peaks to the cL1-HH1 indirect transition between confined states but also proves the type-I band alignment of both the L and the Γ conduction minima.[15] In the inset of Fig. 2.17, the dependence of the energy of the cL1-HH1 zero-phonon emission on the QW thickness is also shown.

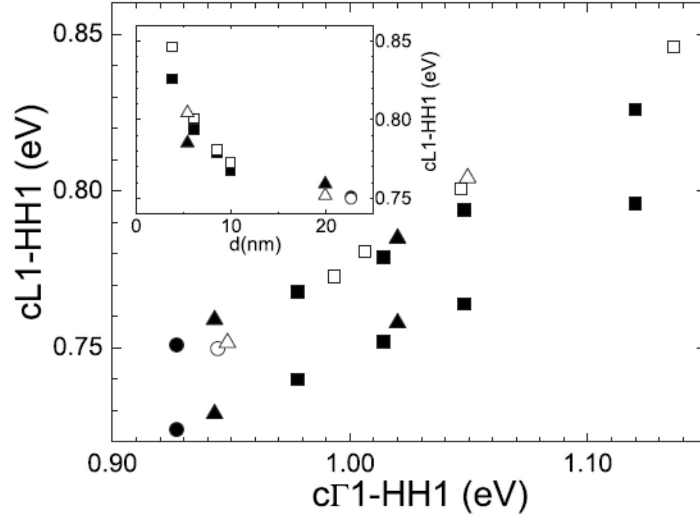


**Figure 2.17:** Energy of the indirect cL1-HH1 zero-phonon transition and of its phonon replica as a function of the energy of the direct cΓ1-HH1transition. Full symbols are experimental data obtained via LT PL measurements on wafers 7873 (triangles), 7864 (squares), and 7909 (dots). The open symbols show the values calculated via tight-binding method (excitonic effects have not been included). In the inset the experimental and the calculated values of the energy of the indirect cL1-HH1 transition are reported as a function of $L_z$.[15]

### 2.3.5 Carrier dynamics

Different literature works are devoted to the study of the dynamics of photoexcited carriers in Ge/SiGe QWs through experimental analysis, mainly pump-probe TR ABS, in most of the cases corroborated by theoretical simulations.[23, 25, 34 - 36, 78] In this Section the main literature results are summarized. They will be an useful reference for the discussion of the experimental results of TR-PL and PL as a function of the excitation wavelength that will be presented in Chapters 3 and 4.

In the following, the results reported in Refs. [25] and [36], obtained on samples analogous to the ones analyzed in this work, are mainly discussed. In Fig. 2.18(b) the RT pump-probe differential ABS in false color scale as a function of the time delay form the pump pulse is reported for Ge/$Si_{0.15}Ge_{0.85}$ MQWs. The pump energy is resonant to the HH3-cΓ3 transition. At $\Delta t = 0$ ps the ABS is heavily bleached at the injection energy only. After about 250 fs, the most of the carriers occupy states in the vicinity of the HH2-cΓ2 transition, and further relax to states next to the HH1-cΓ1 transition after about 450 fs.[36] The observed thermalization times (as a whole about 500 fs) are considerably longer in Ge QWs than in typical III-V QWs (about 100 fs). This difference can be attributed to a lack of Fröhlich interaction[79] due to the purely covalent nature of the bonding.[25] Then, after 500 fs all the carriers have scattered to L-type states via intervalley phonon scattering. The Γ- to L-type states scattering process

results more efficient than intravalley cooling. Moreover, its efficiency increases as the electrons are promoted to states with $\mathbf{k}_{\|} \neq 0$.[36] Typical scattering times are of the order of 200-300 fs. This result has been confirmed also in [34]. The quasi-equilibrium condition, reached by the system after 500 fs, persist to the ns regime.[25]

When the sample is excited resonantly to the HH1-cΓ1 transition (Fig. 2.18(c)), a pronounced scattering to higher energies is observed, mainly towards the subband cΓ2 in proximity of the minimum. The energy necessary to this heating of the system is gained from the excess energy of the electrons scattered to the L valley. Once electrons reach the L valley, they lose their excess energy not only generating phonons, but also interacting with electrons in the Γ valley, causing their up-scattering towards higher energy states.

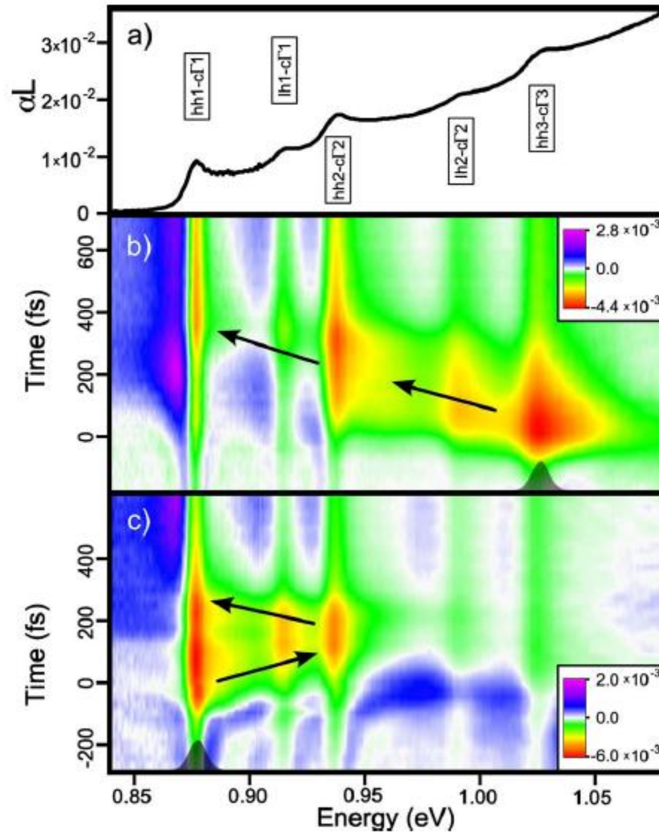


**Figure 2.18:** **(a)** RT linear ASB spectra for 50 Ge/SiGe QWs. **(b) and (c)** RT differential ABS spectra (ΔαL) in false color scale as a function of the delay time form the pump pulse for excitation resonant to the HH3-cΓ3 and the HH1-cΓ1 transitions respectively. The grey pulse shape indicate the respective pump spectra. The relaxation processes are emphasized by the black arrows.[36]

In Ref. [25] the ultrafast response at RT as a function of the optically injected carrier density is investigated. As shown in Fig. 2.19(a) and 2.19(b) , when the sample is excited close to the HH1-cΓ1 transition with a pump photon density of $2.5 \cdot 10^{9}$ cm$^{-2}$ per pulse, ultrafast transient

optical gain is observed as the carriers relax, indicating carrier population inversion around the Γ point. The gain last up to 20 fs; a maximum value of $\alpha L = -8 \cdot 10^{-4}$ per QW is obtained. If the photon density is decreased, lower maximum values can be reached and the gain lasts for longer times, due to slower scattering processes. If the sample is excited far from the resonance, no gain can be observed, since the amount of carriers that scatter to L valley before reaching the bottom of the subband significantly rises. In Fig. 2.19(c) the corresponding calculated spectra are plotted; for each curve the value of the ratio between Γ and L carrier populations is also reported. A comparison between Figs. 2.19(b) and 2.19(c) clearly shows that the gain lifetime is limited by the efficient phonon-assisted Γ to L intervalley scattering.

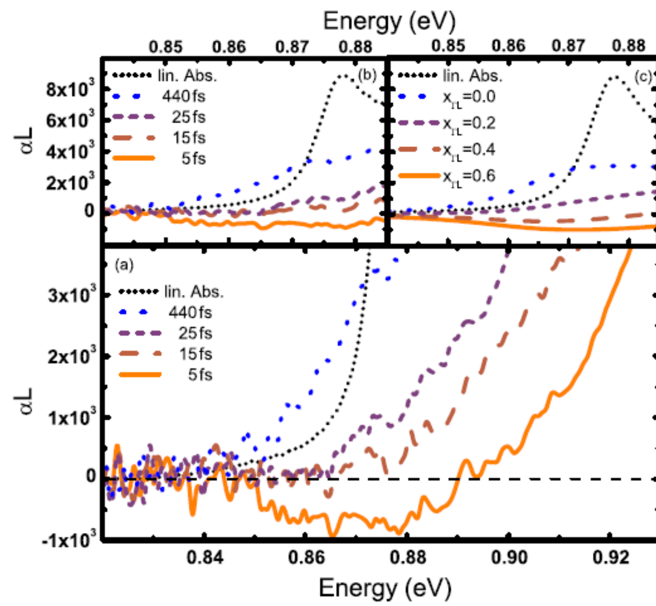


**Figure 2.19:** RT ABS spectra around the HH1-cΓ1 transition. In **(a)** and **(b)** experimental spectra for different delay times from the pump pulse are shown. Corresponding theoretical spectra, selected by line-shape comparison, are reported in **(c);** for each curve the value of the ratio between Γ and L carrier populations is also reported. Linear ABS is reported in all the graphs as a reference.[25]

# Chapter 3

# Indirect gap related emission

This Chapter is devoted to a detailed analysis of the indirect gap related emission in Ge/SiGe QWs.

In the first Section the general features of the recombination process, as resulting from previous works, are reviewed. Moreover, the origin of the zero-phonon line and the attribution of the phonon replicas are discussed in details on the basis of recent literature data and experimental evidences. In Section 3.2 a systematic study of the PL decay of the indirect L-Γ transition is presented, and the dependence of the decay time on QW thickness, excitation density and lattice temperature is discussed in detail.

## 3.1 General features of the indirect recombination

The typical LT PL spectrum of Ge/SiGe MQWs has been reported in Fig. 2.16 and its general characteristics have been shortly presented in Section 2.3.4. In Fig. 3.1 the zoom of the spectral region 0.7 – 0.8 eV of the PL spectrum characterized by the presence of indirect transitions is reported. As already discussed in Section 2.3.4, the peak at 0.768 eV is attributed to the zero-phonon line of the indirect gap related cL1-HH1 transition.

In an indirect QW system, different phenomena can account for the observation of the zero-phonon line. As a matter of fact, in a QW structure the confinement breaks the **k**-conservation rule in the growth direction, $z$, while this selection rule still holds along $x$ and $y$. Consequently, depending on the wavevector **k** of the CB and VB states involved in the transition, the relaxation of **k**-conservation along the $z$-direction can allow the observation of indirect recombination without phonon participation. This effect has been observed, for instance, in indirect gap Si-rich SiGe/Si QWs grown on Si (100) surface. In this case, two of the six equivalent Δ points of the CB are along the $z$ direction (see Fig. 2.3); as a consequence, the confinement itself enables the observation of the zero-phonon transition.[81] Moreover, in these systems the QW material is a SiGe alloy, and the zero-phonon

recombination is favored also by the alloy scattering, that can provide the Δ electrons with the momentum required to recombine with Γ holes.[100]

In the Ge/SiGe QWs with Ge-rich barriers under analysis, the CB absolute minimum is at the L point of the Brillouin zone. The samples are grown on a Si (100) surface and all the equivalent points have a component in the *xy* plane (see Section 2.1, Fig. 2.3). As a consequence, the confinement cannot be at the origin of the zero-phonon line. In literature the observation of the zero-phonon line in QW systems in which momentum conservation is not relaxed by the confinement is justified considering two different mechanisms related to the roughness of the interfaces between wells and barriers. In Ref. [80] the origin of the zero-phonon line is attributed to the carrier scattering with the interface roughness, that provides the required momentum. On the other hand, QW thickness fluctuations localize excitons in regions of lower potential, providing a delocalization of electrons and holes in the **k**-space[81] and thus a non-zero probability for the zero-phonon transition to occur.[80]

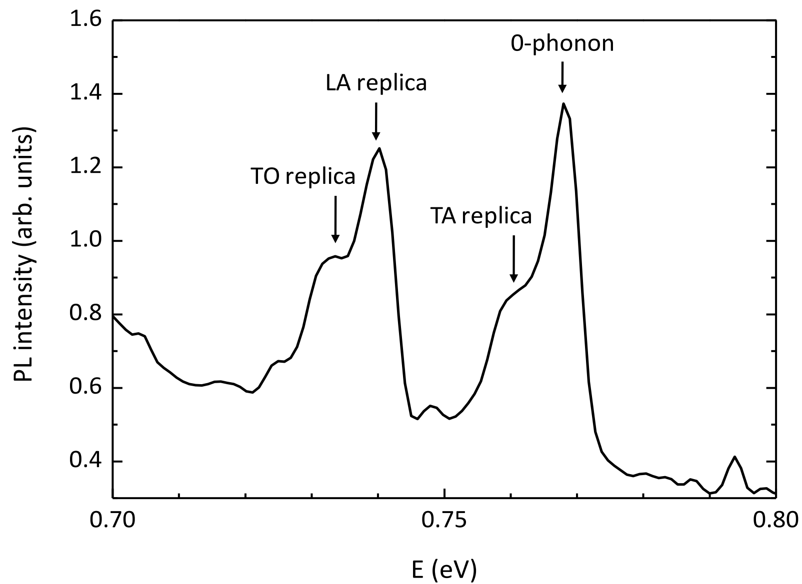


**Figure 3.1:** PL spectrum for Ge/SiGe MQWs (sample 7864-E10) measured at T = 5 K. The spectral region of the indirect emission is here shown in detail.[68]

The indirect spectral region of the PL spectrum reported in Fig. 3.1 is also characterized by the presence of other structures. A Gaussian fit of the two doublets provides the energy of these structures: 0.733 eV, 0.740 eV, and 0.761 eV respectively. All the analyzed Ge/SiGe QW samples display the same features. As discussed in detail in Ref. [68], the energy spacing between the peaks does not depend on $L_z$ and their intensity ratio remains constant varying the exciting power density by orders of magnitude. These results prove that the peak at 0.740

eV and the low energy shoulders at 0.733 eV and 0.761 eV can be phonon replicas of the cL1-HH1 transition.

Literature works, mainly based on Raman spectroscopy, show that in SiGe heterostructures phonon energies are not significantly influenced by the confinement for a QW thickness larger than 2-3 nm.[82 - 84] Accordingly, in different papers on SiGe/Si QWs the phonon replicas have been attributed using for the phonon energies the values of the bulk alloys (see, e.g., Refs. [85 - 87]).

Taking into account that the minimum thickness of the studied Ge/SiGe QWs is 3.8 nm, the attribution of the phonon replicas in the PL spectra of Ge/SiGe QWs can be based on the LT phonon energies at L for bulk Ge (see Fig. 3.2).

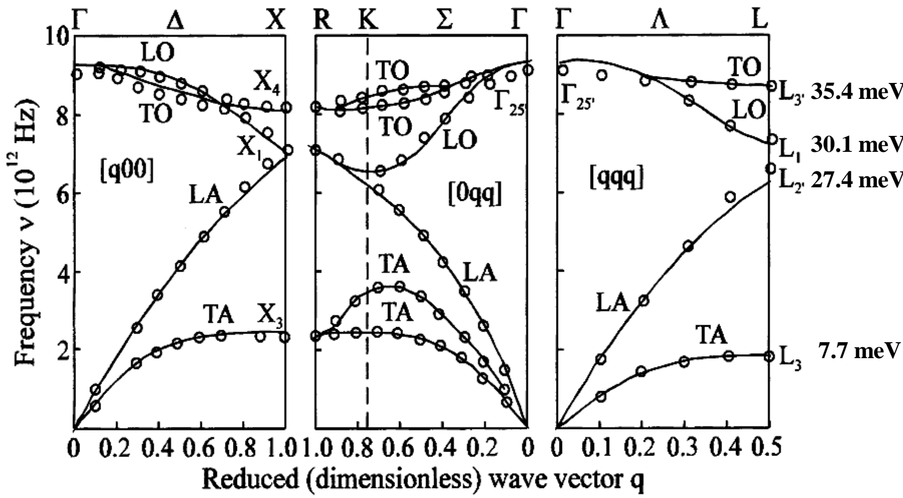


**Figure 3.2:** LT phonon dispersion curves of bulk Ge.[88] The energy of the phonons at the L point of the Brillouin zone are from Ref. [47].

The PL peak at 0.740 eV, 28 ± 1 eV red-shifted respect to the zero-phonon line, is thus attributed to the LA replica. The attribution of this peak to the LA phonon replica is in agreement with Refs. [27] and [89], where Ge/SiGe QWs with Ge-rich barriers grown on Ge substrates are discussed. The energy of the TA phonon at the L point is 7.7 meV (Fig. 3.2) and the shoulder centered at 0.761 meV, 7 meV red shifted respect to the zero-phonon line, can be attributed to the TA replica of the cL1-HH1 transition. Finally, the shoulder at 0.733 eV, separated from the zero-phonon line by 35 meV, is compatible with both the TO replica or the two-phonon TA+LA replica. Since the intensity of a two-phonon replica is expected to be significantly lower than that of a single-phonon one (in Ref. [90], e.g., the ratio of the probabilities of the two processes is estimated to be two orders of magnitude), and the intensity of this structure is compatible with that of the TA replica, the peak is attributed to the TO-phonon-assisted indirect recombination.

The attribution of the phonon replicas in Fig. 3.1 indicates that in Ge/SiGe QWs the interaction with acoustic phonons is more important than the interaction with optical phonons. Literature works confirm this conclusion for Ge-rich SiGe systems. The first confirmation comes from Ref. [58], where bulk SiGe alloys with composition ranging from $Si_{0.92}Ge_{0.08}$ to $Si_{0.07}Ge_{0.93}$ are studied: the related LT PL spectra are shown in Fig. 3.3. In Si-rich alloys, the TO replicas dominate the spectra. However, as the Ge content increases, the intensity of the phonon assisted transitions changes as well as the type of the involved phonons: the contribution of acoustic phonons increases, while the TO replica intensity decreases. It is important to remark that also in the optical spectra of bulk Ge the role of the acoustic phonons is relevant. This has indeed been reported in Ref. [91], where the LA replica dominates the PL spectrum. LT PL measurement performed in this work (Fig. 3.4) confirm this conclusion: the zero-phonon emission is not observed, while intense phonon replicas characterize the spectrum. The TA, LA and TO replicas are visible at 0.700 eV, 0.708 eV and 0.729 eV respectively, and the intensity of the LA replica is about 7 times higher that that of the TO and TA replicas.



**Figure 3.3:** LT near band gap PL spectra for bulk $Si_{1-x}Ge_x$ alloys with different compositions. Zero-phonon ($X^{NP}$) and phonon assisted transitions are visible. [58]

Furthermore, the dominance of the LA phonon is confirmed also by Ref. [32]; in this work, the indirect region of ABS spectra in Ge/SiGe MQWs was calculated assuming a dominant role for LA phonons and well reproduced by experimental photocurrent data.

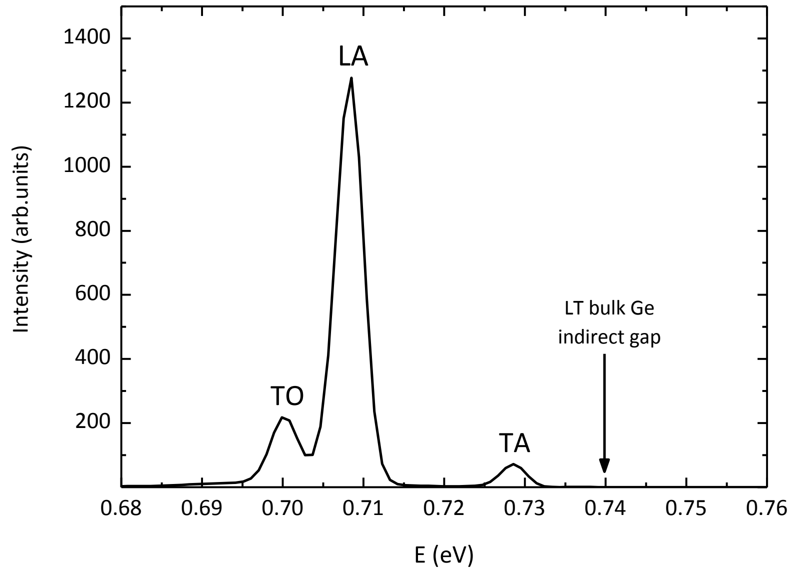


**Figure 3.4:** Experimental PL spectrum of bulk Ge at the lattice temperature of 2 K (excitation power density of about 2 kW/cm$^2$). The TA, LA and TO phonon replicas of the indirect recombination are observed. The attribution is supported by Refs. [47, 58, 88]. Exciton binding energy (about 4 meV in bulk Ge)[27] was also considered.

No evidence is experimentally found in the PL spectra of the indirect cL1-LH1 transition, involving the first LH confined valence state. On the basis of the calculated band structure (see Fig. 2.8), the energy distance between the cL1-HH1 and cL1-LH1 transitions is expected to be about 40 meV. On the contrary, as it will be shown in Chapter 4, the cΓ1-LH1 emission is commonly present in the direct gap related PL spectra. This difference may be traced back to two factors: (i) the oscillator strength of the cL1-HH1 and cL1-LH1 transitions, and (ii) the DOS of the HH and LH bands. First, transitions at Γ involving LH states are characterized by a lower oscillator strength respect to those involving HH states. Indeed, the ratio of the probability of cΓ1-LH1 transition and cΓ1-HH1 direct transitions is one third (see Tab. 2.3). An analogous behavior may be reasonably assumed for the cL1-LH1 and the cL1-HH1 transitions, despite the different initial state involved. Furthermore, we should consider that the transition rate of an indirect transition is proportional to the product of the DOS of the initial and final states[92]; thus, the different effective mass value of HH and LH

valence states favors the cL1-HH1 recombination. These two factors may account for the lack of the cL1-LH1 transition in the PL spectra.

## 3.2 Decay time of the indirect recombination

In this Section the results of a detailed experimental study of the decay time of the indirect cL1-HH1 emission are presented. The decay time dependence on the QW thickness $L_z$, on the emission wavelength and on the lattice temperature is discussed and compared with literature data. Where no otherwise specified, the measurements have been performed under *non-resonant* excitation conditions ($\lambda_{exc}$ = 351 nm), i.e. electrons are promoted to the *continuum* states of barriers and wells. In these excitation conditions, as it will be discussed in Section 4.4, at LT the indirect gap related emission only is visible, since the excited electrons thermalize directly to L-type states.

The details of the experimental techniques used for the decay time measurements are reported in Section B.3.1. Nevertheless, for the discussion of the experimental data presented in this Section, it is important to remind that the shortest measurable decay time is 2 ns and the precision of the measured decay time is ± 0.3 ns. Moreover, the measured decay curve is actually a convolution of the exponential PL decay and of the laser pulse, which has a Gaussian shape (see Section B.3.2). Consequently, the decay time has always been obtained through the deconvolution procedure described in Section B.3.2, where the method used for the extraction of the decay time values from the experimental decay curves is discussed in detail.

### 3.2.1 Decay time values

A detailed discussion of the different processes involved in the PL of semiconductors can be found in different papers. In this work we refer to Refs. [92] and [93] for bulk semiconductors and to Ref. [94] for QW systems. We concentrate here on the total decay time, $\tau_{tot}$, which is the experimental result of a decay time measurement. Once the photoexcited electrons have thermalized to the bottom of the CB, they can recombine with holes at the top of the VB through different radiative and non-radiative channels.

In case of indirect transitions the radiative recombination can occur through different mechanisms, such as phonon participation or scattering with interface roughness; as described in Section 3.1, these processes are important for Ge/SiGe QWs. These mechanisms are

characterized by different decay times. If the probabilities of the different processes are independent, the radiative decay time $\tau_{rad}$ can be written as

$$\frac{1}{\tau_{rad}} = \frac{1}{\tau_1} + \frac{1}{\tau_2} + \ldots \quad , \tag{3.1}$$

where $\tau_1$, $\tau_2$, … are the decay times characterizing the different processes. If the *i* process is significantly faster than the others, $\tau_{rad}$ coincides $\tau_i$. If all the processes are competitive, they all contribute significantly to determine the $\tau_{rad}$ value.

Similarly a non-radiative decay time $\tau_{nonrad}$ can be defined: different processes can contribute to $\tau_{nonrad}$, and a relation analogous to the previous one can be written.

Finally, assuming independent radiative and non radiative recombination processes, the total decay time $\tau_{tot}$ of the excited carrier recombination process is given by

$$\frac{1}{\tau_{tot}} = \frac{1}{\tau_{rad}} + \frac{1}{\tau_{nonrad}} \, . \tag{3.2}$$

Figure 3.5 shows a typical decay curve obtained for the zero-phonon cL1-HH1 transition at the lattice temperature T = 14 K. A single exponential decay is observed over about three decades. At this lattice temperature decay times of the order of 10 ns have been measured for all the analyzed samples (see Fig. 3.8).

To the best of our knowledge, no data on the decay time of Ge QWs with Ge-rich barriers are reported in literature and no data can be easily found on confined indirect gap systems characterized by a type-I band alignment. The only example of TR-PL analysis of an analogous system is given in Ref. [80], where decay times of the order of 50-200 ns are reported for (GaIn)As/InP QWs, depending on composition and QW thickness.

The $\tau_{tot}$ values we measured are compatible with the literature data on type I direct gap QWs based on III-V materials and on type II indirect gap Si-rich QWs. In type-I direct gap QWs based on III-V semiconductors, where optical transitions are favored by the direct nature of the gap and by the increased electron-hole wavefunction overlap, the typical decay times are of the order of hundreds of ps.[95 - 99] In type-II indirect gap SiGe/Si QWs, on the contrary, the localization of electrons and holes in different spatial regions and the indirect gap give decay times of the order of hundreds of ns or higher.[81, 100, 101] Since our systems are characterized by an indirect transition in type-I QWs, intermediate decay time values are expected. Indeed, the measured $\tau_{tot}$ values are just one order of magnitude higher than those typical of type-I direct-gap III-V QWs, as expected due to a lower transition probability, and about two orders

of magnitude shorter than those typical of type-II indirect-gap SiGe/Si QWs, thanks to the type-I band alignment.

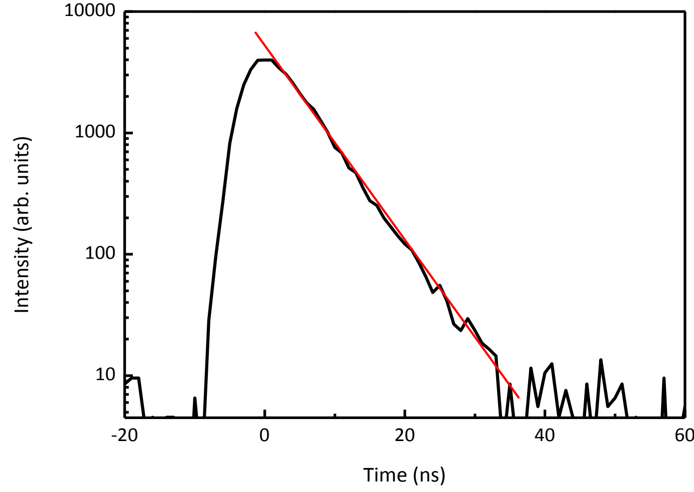


**Figure 3.5:** Typical decay curve of the zero-phonon cL1-HH1 transition; data refer to sample 7909-F1 measured at the lattice temperature of 14 K.

In different samples the decay was measured also for the LA phonon replica of the cL1-HH1 transition. The decay time of the LA replica always reproduces that obtained for the zero-phonon line, as expected. Indeed, decay time measurements detect the depletion rate of the excited state involved in the transition, regardless of the different mechanisms that contribute to the depletion, as previously discussed. Consequently, no difference is expected between the decay time of the LA replica and of the zero-phonon emission, since the same initial and final states are involved. This result is a further confirmation of the attribution of the peak at 0.740 eV in Fig. 3.1 to a phonon replica.

### 3.2.2 Decay time dependence on the emission wavelength

As described in Section B.3.1, the decay curve is measured at a fixed wavelength, usually in correspondence of the zero-phonon peak. In some cases, however, the decay has been measured also as a function of the emission wavelength. In Fig. 3.6 the decay time $\tau_{tot}$ is reported as a function of the emitted photon energy. The CW-PL spectrum of the same sample measured under non-resonant excitation conditions is also reported as a reference. When the emitted phonon energy is close to the zero-phonon line maximum (about ± 10 meV), $\tau_{tot}$ remains constant within the experimental error; however, moving to higher energies, $\tau_{tot}$ starts

to decrease. This behavior could be due to the cooling process of the carriers occupying states far from the conduction minimum, which is competitive with the radiative recombination. Moreover, measurement as a function of exciting power density have shown that the decay time at the maximum of the zero-phonon peak is not modified if the excitation power density is reduced by more that one order of magnitude. This suggests that $\tau_{rad}$ is a relevant component of $\tau_{tot}$. As a matter of fact, the decay time is expected to vary with the exciting power density when non radiative processes, like Auger effect or recombination involving defect levels, which are respectively enhanced and reduced by higher exciting power densities, are important.

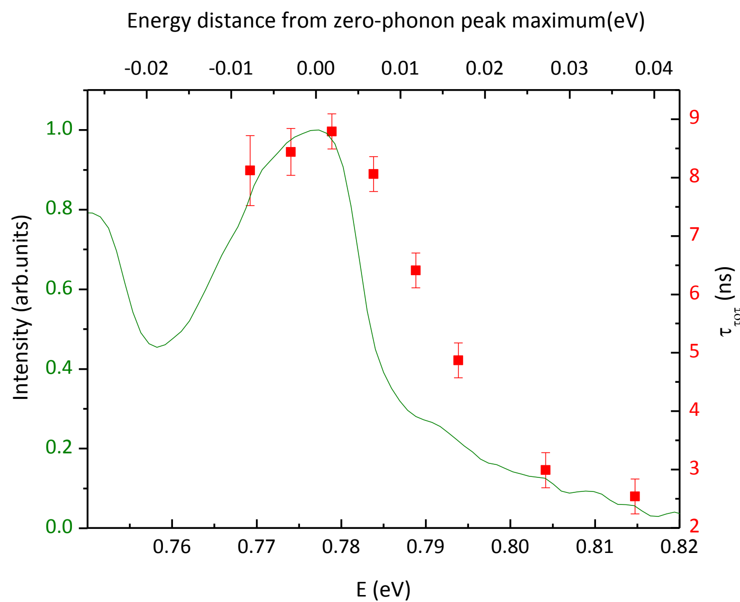


**Figure 3.6:** Decay time as a function of the emitted photon energy (red squares) at the lattice temperature of 14 K for sample 7864-E5. The CW-PL spectrum (green line) is also reported.

If the time integral of the decay curves is plotted as a function of the wavelength at which the decay has been measured, an *integrated spectrum* is obtained. An example of integrated spectrum is shown by the black dots in Fig. 3.7, where the CW-PL spectrum measured on the sample under non-resonant excitation ($\lambda_{exc}$ = 532 nm) is also reported. There are two evident differences between the spectra: (i) at energies lower than 0.77 - 0.78 eV the integrated spectrum only is affected by the detector cutoff (see Section B.3.1), and (ii) the high energy tail of the integrated spectrum is more intense. This latter can be justified taking into account the excitation conditions. The power density used in CW-PL measurements is about 2 kW/cm$^2$ (see Section B.2), while the peak power density in the decay time measurements is

about $5.5\cdot10^3$ kW/cm$^2$ (see Section B.3.1). Since the typical $\tau_{tot}$ values are of the order of 10 ns and the laser pulse lasts few ns, we can safely assume that the ratio between the excited carrier densities in the two excitation conditions is of the same order of magnitude of the ratio between the above exciting power densities. This ratio accounts for the difference between the two spectra: hot-carrier recombination can be expected to contribute to the integrated spectrum due to the significantly higher excited carrier density in decay time measurements.

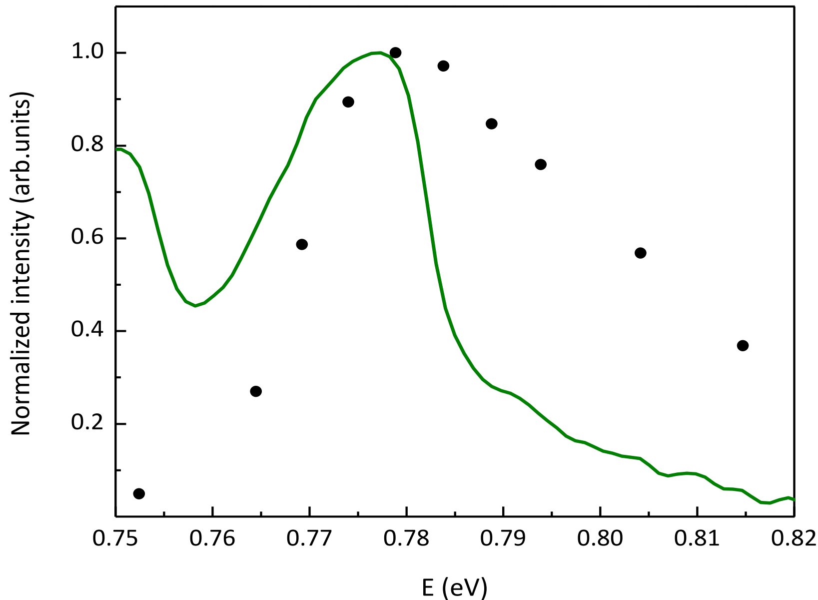


**Figure 3.7:** Comparison between integrated spectrum (black dots) and CW-PL spectrum (green line) of the zero-phonon line of sample 7864-E5; the two spectra are measured under non-resonant excitation conditions at the lattice temperature T = 14 K.

### 3.2.3 Decay time dependence on well thickness

The decay time of the zero-phonon emission in different samples is reported in Fig. 3.8 as a function of the QW thickness. Samples with QW thickness ranging from $L_z = 3.8 \pm 0.5$ nm to $L_z = 22.6 \pm 1.0$ nm were analyzed at the lattice temperature of 14 K; the $L_z$ determination is discussed in Section B.1.2.

Data in Fig. 3.8 show that the decay time increases as the QW thickness increases with a nearly linear trend. An analogous behavior has been reported for both III-V[95 - 97, 102, 103] and SiGe/Si[81] QWs. In the literature, different phenomena are suggested to contribute to the observed dependence of the radiative lifetime on $L_z$.

(1) The exciton binding energy depends on the QW thickness (see Section A.4), and increases as the QW width is reduced[104]; the transition probability is thus enhanced, giving rise to a reduction of $\tau_{rad}$.[81, 95, 97, 105] This is also confirmed in Ref. [96], where the following dependence of the decay time on the binding energy of the 2D-exciton ( $E_B^{2D}$ ) has been obtained

$$\tau^{2D} \propto \frac{\Delta(T)}{E_B^{2D}} \ . \tag{3.3}$$

In Eq. 3.3 $\Delta$ is the homogeneous width of the excitonic PL peak, which is expected to increase as $L_z$ increases. The homogeneous contribution to the FWHM is determined by the transition probability and, in the case of a phonon assisted transition, by the curvature of the phonon and electron dispersions at the points of the Brillouin zone involved in the transition. The inhomogeneous contribution is due to extrinsic factors, that change from sample to sample: in Ge/SiGe QWs the main extrinsic factor can be reasonably assumed to be the interface roughness.

Preliminary results suggest that in Ge/SiGe QWs the inhomogeneous component prevails on the homogeneous one. In fact, from preliminary measurements of the dephasing time of the excitonic transition on sample 8009-G7 a homogeneous component of about 2-3 meV can be estimated at LT, while FWHM values between 4 and 20 meV are found for the HH1-c$\Gamma$1 LT ABS peak of the different samples. Consequently, it has not been possible to check experimentally the validity of Eq. 3.3 for Ge/SiGe QWs through PL measurements.

(2) The interface roughness has also to be taken into account, because of its important role in the zero-phonon emission, as discussed in Section 3.1. As $L_z$ decreases, the role of the interface roughness becomes more relevant, as shown in Refs. [102, 106]. Accordingly, the zero-phonon emission, favored by exciton scattering[80] and exciton localization at the minima of the spatially fluctuating potential, [80, 81] becomes more probable and the decay time is expected to decrease.

(3) Finally, also the superposition of electron and hole wavefunctions depends on $L_z$, and thus it is expected to contribute to the dependence of the decay time on $L_z$. The decrease of the decay time is indeed compatible with the increasing overlap of electron and hole wavefunctions due to the reduction of $L_z$. However, when the QW thickness is lower than a critical value, the wavefunction overlap is expected to start decreasing, since the wave function significantly penetrate the barriers. Accordingly,

the decay time is expected to rise as shown e.g. in Ref. [81] for SiGe/Si QWs, where a critical $L_z$ of 4 nm is found. In Ge/SiGe QWs no rise of the decay time is observed as $L_z$ decreases: this may be due to the fact the critical QW thickness is equal or lower than the minimum $L_z$ considered (3.8 nm); this is compatible with the high offsets typical of this system (see Fig. 2.8), which are indeed higher than in SiGe/Si systems (see Fig. 2.7).

Summarizing, the decrease of the decay time as the QW thickness decreases can be mainly due to intrinsic factors, and suggests that $\tau_{rad}$ is a non negligible component of the total decay time. An analogous behavior is reported also in different literature works.[81, 95 - 97]

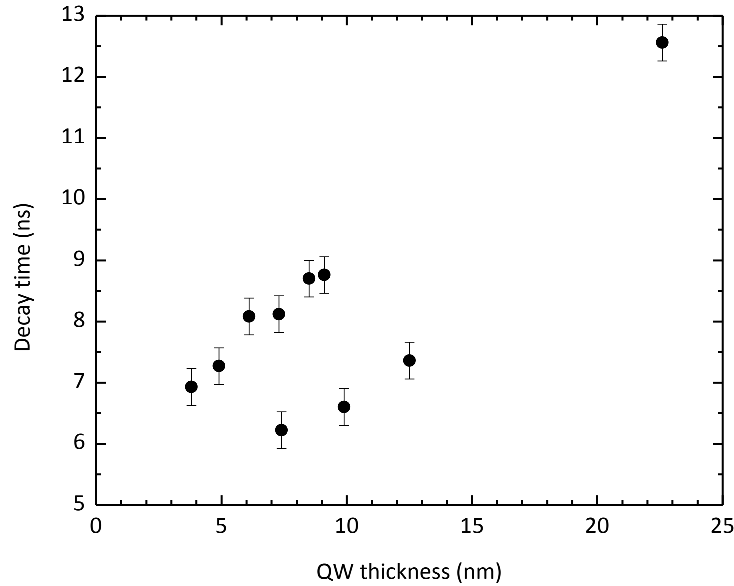


**Figure 3.8:** Decay time of the zero-phonon cL1-HH1 transition as a function of QW thickness at the lattice temperature T = 14 K.

Data points in Fig. 3.8 show also that different decay times can be found in different samples with the same $L_z$. In literature this behavior is associated to different defect concentration and interface roughness. [80, 96, 102, 107] In our case, this hypothesis is in good agreement with the results of CW-PL and ABS measurements. In Fig. 3.9 the LT CW-PL spectra of the two samples characterized by the same $L_z$ = 7.3 nm (as shown by the common value of the zero-phonon energy, 0.785 eV), but different decay times (see Fig. 3.8) are reported. The spectra have been normalized for an easier comparison. The blue line refers to the sample with $\tau_{tot}$ = 8.1 ± 0.3 ns and is the typical spectrum of samples characterized by long decay times, while the orange line refers to the sample with $\tau_{tot}$ = 6.2 ± 0.3 ns and is the typical spectrum of

samples characterized by short decay times. In both the spectra a peak at about 0.6 eV is present, attributed to transitions related to defects, mainly dislocations[68] (see Section 2.3.4).[a] The relative intensity of the dislocation-related peak provides indications about the dislocation density. The ratio is considerably higher for the sample characterized by the shorter decay time, and this suggests that a higher density of competitive recombination channels associated to defects may give rise to a reduction of $\tau_{tot}$. This is confirmed by literature works such as Refs. [80] and [107].

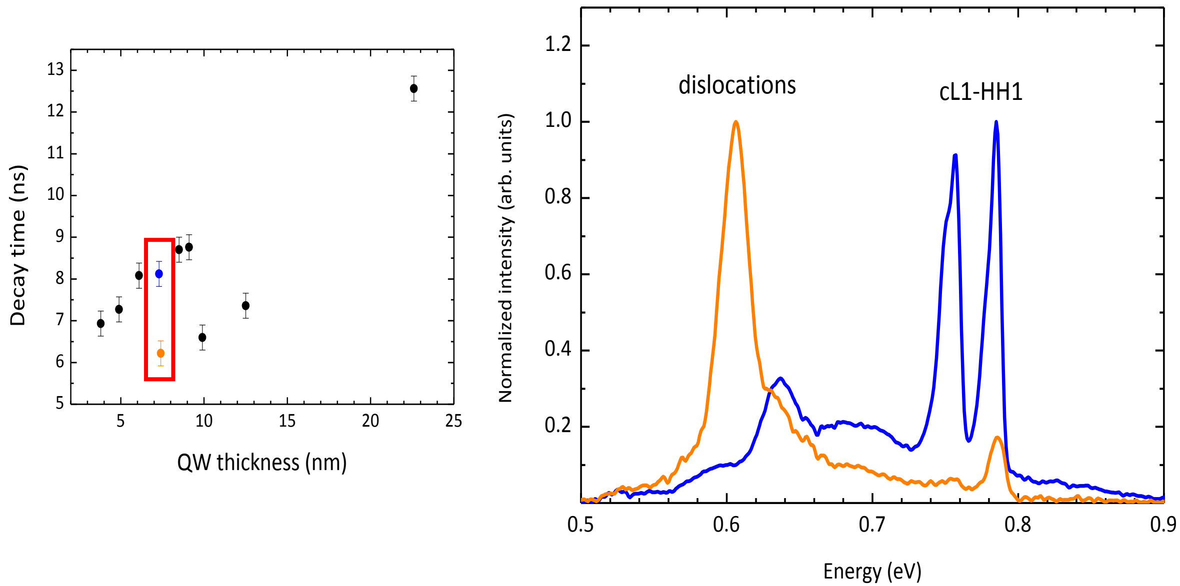


**Figure 3.9 :** CW-PL spectra of two samples characterized by the same $L_z$ (7.3 nm) but different decay times at the lattice temperature of 5 K, as indicated by the red rectangle in the grapf on the left. The orange line is the spectrum of sample 7909-F1, characterized by a shorter decay time (6.2 ± 0.3 ns), while the blue line is the spectrum of sample 7864-E4 characterized by a longer decay time (8.1 ± 0.3 ns). PL spectra have been normalized to their maximum.

Moreover, even in this case the interface roughness must be taken into account to explain data in Fig. 3.8. The samples characterized by a short decay time present at LT a HH1-cΓ1 ABS peak broader (average value 10 ± 1 meV) compared to the samples characterized by a long decay time (average value 6 ± 1 meV). This indicates that in samples featuring rougher

[a] The difference of about 20 meV between the dislocation peak energy of the two spectra can be easily explained. One of the parameters that influence the peak energy of the dislocation related emission in SiGe alloys is the annealing time: the PL peak blue shifts as the annealing time increases.[77, 110] The MQW stack has been grown at low rate for the sample 7864-E4 and at high rate for the sample 7909-F1. Consequently the VS in the first case has been exposed to high temperatures (i.e. it has been effectively annealed) for a considerably longer time respect to the latter. Since the dislocations in the active layers are those generated in the VS (see Section B.1.2), the blue shift of the dislocation peak of sample 7864-E4 is explained.

interfaces the probability of the zero-phonon indirect transition is enhanced by scattering and localization phenomena, and this corresponds shorter decay times.

In conclusion, in this Section the dependence of $\tau_{tot}$ on $L_z$ has been discussed. The increase of $\tau_{tot}$ as $L_z$ increases proofs that $\tau_{rad}$ is a non negligible component of the total decay time. This result is supported by different literature works, such as Refs. [95 - 97, 81]. Nevertheless, the observation of different decay times in QWs characterized by the same $L_z$ indicates that extrinsic effects, which change from sample to sample, can also affect the decay time. In particular for a given $L_z$, a higher interface roughness contributes to a shortening of $\tau_{rad}$, while non-radiative competitive channels due to a higher defect concentration reduce $\tau_{nonrad}$.
Analogous results have been proposed e.g. in Ref. [96], where both the linear decrease of the decay time in response to a reduction of $L_z$ due to intrinsic contribution, and the extrinsic effects that affect the decay time in a different way from sample to sample are reported.
Finally, it is important to underline that at 14 K radiative and non radiative contributions to $\tau_{tot}$ result to be of the same order of magnitude (see Fig. 3.8).

### 3.2.4 Decay time dependence on temperature

Different literature works discuss the decay time dependence on the lattice temperature. Most of them concern direct gap QWs based on III-V semiconductors. As far as the decay time can be considered purely radiative, it is expected to increase linearly with T, as predicted in Ref. [108] and experimentally confirmed in Ref. [96]. Then, when the temperature exceeds a critical value, thermally-activated non-radiative processes become important and the total lifetime starts to decrease.[81, 96, 98, 103, 109] The critical temperature value depends on the system, on the sample quality, and on the nature of the thermally-activated non-radiative processes.

In this thesis work, the decay time of Ge/SiGe QWs was measured as a function of the lattice temperature between 14 K and 300 K for different samples. At all the temperatures the emission was collected at the energy of the zero-phonon line. As will be discussed in Chapter 4, for T higher than about 90 K the PL peak broadening prevents the experimental observation of a resolved zero-phonon line in CW-PL spectra. Consequently, the zero-phonon line position was estimated on the basis of the thermal reduction of the Ge indirect gap described by Varshni’s law with the parameters reported in Table 2.2.

A common dependence on T was observed in all the analyzed samples. As an example, in Fig. 3.10 $\tau_{tot}$ is plotted as a function of the reciprocal temperature for samples 7864-E4 ($L_z$ = 7.3 nm) and 7864-E1 ($L_z$ = 3.8 nm). A monotonic decrease of $\tau_{tot}$ is observed as the temperature rises. Differences in $L_z$ influence the absolute $\tau_{tot}$ value but not the $\tau_{tot}$ dependence on T; this behavior is reported also in Ref. [96].

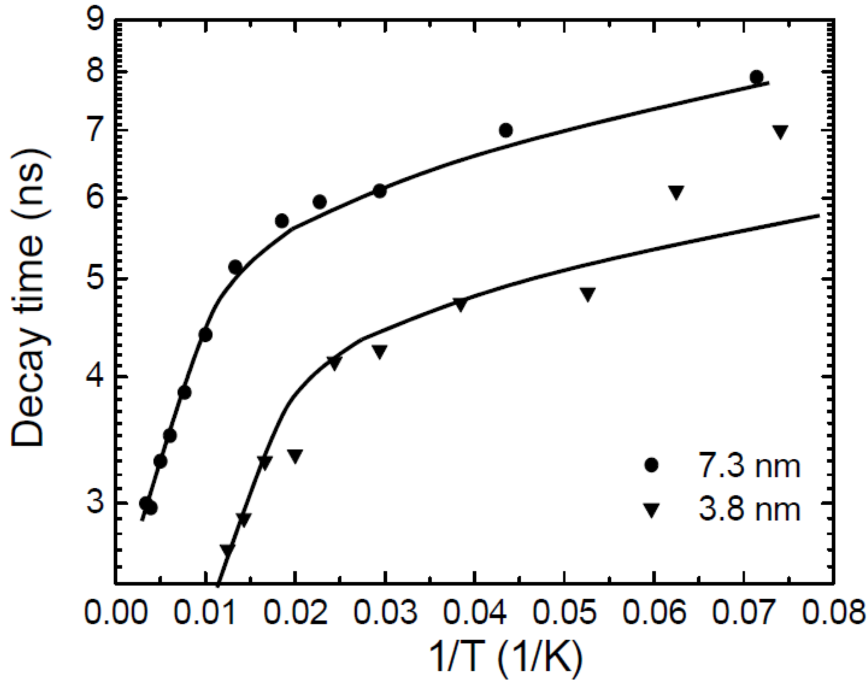


**Figure 3.10:** Decay time as a function of the reciprocal temperature for two samples 7864-E4 ($L_z$ = 7.3 nm) and 7864-E1 ($L_z$ = 3.8 nm) respectively. Solid lines are guides to the eye.

Different intrinsic and extrinsic effects can contribute to the observed decay time reduction with increasing T. First, the enhancement of the non radiative channels has to be considered. CW-PL spectra measured as a function of the temperature (see Section 4.2) show that the intensity of the indirect gap related emission monotonically decreases for increasing T. The decrease of the PL intensity, which is particularly relevant at temperatures higher than 70 K, proves the contribution of non-radiative channels to the decrease of $\tau_{tot}$. Furthermore, the increase of the phonon population enhances the probability of phonon assisted recombination, producing a decrease of $\tau_{rad}$. The exciton mobility has also to be taken into account: it is expected to be enhanced due to the increase of exciton thermal energy. In other words, excitons localised at the minima of the spatially fluctuating potential have enough thermal energy to overcome the potential barriers and become free 2D excitons; as a consequence, their lifetime is expected to decrease. This effect is described in Ref. [96] for GaAs/AlGaAs

QWs: $\tau$ is shown to remain constant until the exciton is localised and then to decrease as soon as excitons become free due to their thermal energy. Finally, in the literature the thermally activated exciton escape into barrier regions is also proposed to explain the reduction of the decay time as T rises.[98, 109] Unlike literature cases (InGaAs/GaAs QWs[109] and GaAs/AlGaAs QWs[98]), in which a band offset of few meV can be easily overcome thanks to thermal energy, in the analyzed Ge/SiGe QWs this phenomenon can be excluded due to the higher offset values (see Fig. 2.8).

In conclusion, the increase of non-radiative recombination processes, the increase of the phonon population, and the enhancement of exciton mobility are all expected to contribute to the decrease of $\tau_{tot}$ as the temperature increases. Nevertheless, a quantitative analysis of the different contributions is not possible. As a matter of facts, the above processes are characterized by different activation energies; but, since the decay time values vary of half a decade only in the temperature range 14 to 300 K, no reliable evaluation of the activation energies is possible.

## 3.3 Conclusions

In this Chapter a detailed study of the indirect gap related cL1-HH1 recombination in Ge/SiGe QWs, based on the analysis of the results of CW-PL and decay time measurement, has been presented.

The mechanisms responsible for the zero-phonon emission in these systems are discussed and the phonon-replicas are attributed on the basis of literature results and experimental data: in particular, the acoustic phonon contribution is found to be more important than the optical phonon contribution. Moreover, the similar intensity of the LA replica and the zero-phonon PL peaks indicates that in the most cases these two recombination mechanisms are equally probable.

To the best of our knowledge, no results on the decay times in Ge/SiGe QWs have been reported in literature so far. Thus, the first detailed study of decay times in Ge/SiGe QWs has been presented in this work. The measured decay time values of the indirect cL1-HH1 transition are of the order of 10 ns at 14 K. These decay times are just one order of magnitude higher than those typical of type-I direct gap III-V QWs and shorter than those characteristic of type-II indirect gap SiGe/Si QWs. The observed strong dependence of the decay time on QW thickness has been analyzed. The decrease of the decay time with decreasing QW thickness can be related to intrinsic factors, and suggests the significant contribution of the

radiative component to the $\tau_{tot}$ value. On the other hand, the observation of different decay times in samples characterized by the same $L_z$ may be due to contribution of extrinsic factors that change from sample to sample. Our results suggest that at LT the radiative and the non-radiative components have effects of the same order of magnitude on the total decay time value. Finally, the marked dependence of the decay time on the lattice temperature can be accounted for considering both radiative and non-radiative contributions.

# Chapter 4

# Direct gap related emission

In this Chapter a detailed description of the direct gap related emission in Ge/SiGe QWs is provided through the analysis of CW and TR-PL results.
First, the main features of the direct emission are presented; after a short description of the PL spectra, mainly devoted to the discussion of the SS, self-absorption corrections and the recombination involving states with $n > 1$ are described and discussed. Then, the dependence of PL on the lattice temperature is analyzed; our results confirm that the thermal promotion of electrons from L- to Γ-type states has a relevant role in the direct emission at RT. Moreover, an analysis of the relaxation processes of photoexcited carriers is performed through TR-PL, together with PL as a function of the excitation wavelength and pump-probe TR ABS measurements. Our data suggest that an ultrafast electron inter-subband scattering occurs at Γ. This analysis, together with the results presented in Chapter 3, allows to conclude this Chapter with an overall picture of carrier thermalization and recombination processes in Ge/SiGe QWs. The intricate interplay between the different relaxation processes in Ge/SiGe QWs yields spectral features different from the commonly observed emission features in typical GaAs-based QWs.

## 4.1 General features

This Section is devoted to the description of the typical features of the direct region of the LT CW-PL spectra. All the measurements presented here have been performed under *resonant* excitation conditions: carriers are excited between QW confined states since the exciting photon energy (1.165 eV = 1064 nm) is higher than the direct optical gap energy of the Ge QWs but lower than the direct gap energy of the $Si_{0.10}Ge_{0.90}$ barriers (see Fig. 2.8). At LT the direct emission is indeed visible only under these excitation conditions, as will be discussed in detail in Section 4.3. A detailed description of the experimental setup used for the CW-PL measurement presented here is reported in Section B.2.

The typical LT PL spectrum of Ge/SiGe MQWs has already been reported in Fig. 2.16 and its general characteristics have been shortly presented in Section 2.3.4. In Fig. 4.1 the zoom of the spectral region 0.90 – 1.05 eV, characterized by the presence of direct transition, is reported. As previously discussed, the peak at 0.974 eV is attributed to the cΓ1-HH1 direct gap related recombination. This PL peak is 14 meV red-shifted respect to the ABS peak related to the same transition. This energy distance between PL and ABS peaks is known as *Stokes shift* (SS). A detailed description of the SS can be found, e.g., in Ref. [111] and references therein. The origin of the SS in QWs is related to the interface roughness: the photoexcited carriers thermalize at the local energy minima (i.e., in the regions with larger $L_z$). As a consequence, the PL peak is red-shifted respect to the ABS peak. Obviously, in an ideal QW with flat and equally spaced interfaces, no SS should be observed. The SS is indeed an index of the interface quality: the smaller is the SS, the higher is the interface quality.

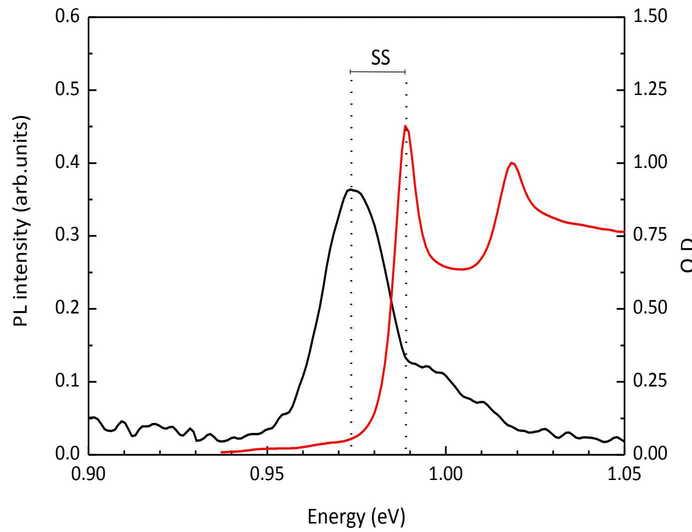


**Figure 4.1:** CW-PL spectrum of Ge/SiGe MQWs (sample 7864-E10) measured at the lattice temperature T = 5 K (black line). The spectral region of the direct emission is shown in detail. The ABS spectrum at the same lattice temperature is also shown for reference (red line). The distance between ABS and PL peaks related to the same transition is known as Stokes shift.

Since both SS and ABS FWHM depend on interface roughness, they can be related to each other. In Ref. [112] a linear relation is proposed

$$SS = b \cdot FWHM, \tag{4.1}$$

where the theoretical value of the parameter *b* is 0.55. Experimental SS values obtained in a set of III-V and II-VI QW samples have been collected in Ref. [112] and plotted as a function of the ABS FWHM (Fig. 4.2): the experimental data are fitted with a straight line whose slope is 0.6, in good agreement with the theoretical value. The red spot in Fig. 4.2 gives the

dispersion of the experimental data obtained in this work through the analysis of a number of Ge/SiGe QWs characterized by different QW number, thickness and growth rate. These experimental data give for the SS an average value of 11.0 ± 3.2 meV and for the ABS FWHM[b] an average value of 9.3 ± 4.3 meV; as shown in Fig. 4.2, these values are in good agreement with the literature trend.[112]

In discussing these data, it is important to note that in our case different factors may contribute to make a detailed analysis of the SS complex. First, PL and ABS measurements explore different areas of the sample, of the order of about $10^{-3}$mm$^2$ and about 1 mm$^2$ respectively (see Section B.2). Then, the ABS measurements probe all the QW stack, while in PL measurements the penetration depth of the exciting light ($\lambda_{exc}$ = 1064 nm) corresponds to about 50 QWs (see Section B.2). Finally, a local sample heating due to the laser may affect the lattice temperature in PL measurements and, consequently, may induce a red shift of the PL peak energy. All these factors are estimated to produce an indetermination of the order of few meV on the SS value, and thus do not modify the above conclusion.

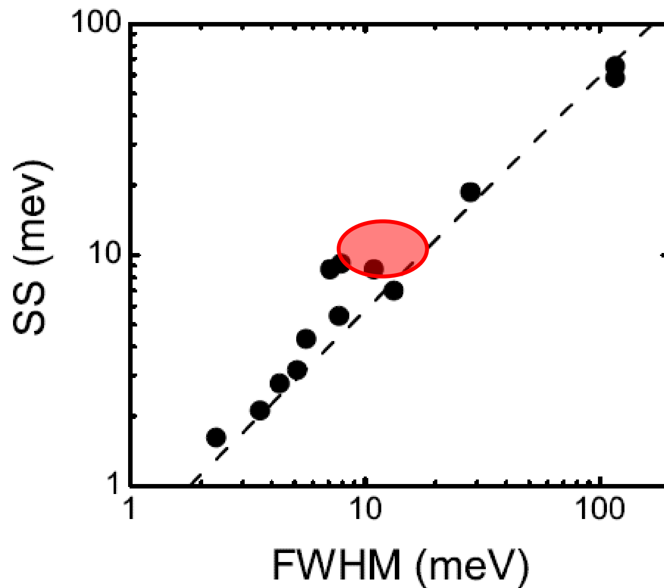


**Figure 4.2:** SS as a function of the FWHM of the ABS peak for GaAs, InGaAs, GaAsP, ZnSe, ZnSeS QWs. The data have been collected in Ref. [112]. The red spot represents the data obtained for different samples of Ge/SiGe QWs in this thesis work.

[b] The ABS FWHM has been evaluated through a Lorentzian fit of the HH1-cΓ1 peak of the experimental LT ABS spectra.

### 4.1.1 Self absorption

The cΓ1-HH1 peak of LT CW-PL spectra of our samples is usually characterized by a marked change of slope in the high energy tail. In Fig. 4.3 this marked change of slope is at 0.988 eV. The energy position of the slope change corresponds to that of the HH1-cΓ1 ABS peak. This suggests that the shape of PL spectra is affected by *self-absorption* effects: part of the light emitted is absorbed by the sample itself before reaching the surface.

Self-absorption effects on the PL spectra can be corrected on the basis of a simple model.[93] Let us consider first the case of bulk materials, excited by a laser with penetration depth given by $1/\alpha(\lambda_{exc})$, where $\alpha(\lambda_{exc})$ is the ABS coefficient at the wavelength of the exciting laser.

The effective intensity of the exciting laser ($I_L$) decreases with the depth *x*. The relation

$$-\frac{dI_L(x)}{dx} = \alpha(\lambda_{exc}) I_{L,0} e^{-\alpha(\lambda_{exc})x} \quad , \tag{4.2}$$

where $I_{L,0}$ is the intesity of the exciting laser at the depth 0, gives the excitation of PL. We assume that the recombination efficiency is independent on the intensity and that the excited carriers do not diffuse. Neglecting the reflection at the sample-air surface and assuming that the laser is completely absorbed by the sample, the measured spectrum $I_{meas}(\lambda)$ is given by

$$I_{meas}(\lambda) = I_{real}(\lambda) \int_0^{\infty} \alpha(\lambda_{exc}) I_{L,0} e^{-\alpha(\lambda_{exc})x} e^{-\alpha(\lambda)x} dx \, , \tag{4.3}$$

where $I_{real}(\lambda)$ is the "real" emitted spectrum and the therm $e^{-\alpha(\lambda)x}$ accounts for self-absorption. Thus, the "real" spectrum $I_{real}(\lambda)$ can be calculated from the measured spectrum $I_{meas}(\lambda)$ through the relationship

$$I_{real}(\lambda) \div I_{meas}(\lambda) \cdot \frac{(\alpha(\lambda_{exc}) + \alpha(\lambda))}{\alpha(\lambda_{exc})} \, . \tag{4.4}$$

Moving to the case of a QW system, the attenuation depends on the number of QWs only and not on their thickness, as discussed in Section 2.3.1 and in Refs. [19, 67, 68], and thus in Eq. 4.4 the ABS coefficients have to be expressed in (*number of wells*)$^{-1}$. If the sample is excited resonantly, the barriers can be assumed to be transparent, and Eq. 4.4 becomes

$$I_{real}(\lambda) \div I_{meas}(\lambda) \cdot \frac{A(\lambda_{exc}) + A(\lambda)}{A(\lambda_{exc})} , \tag{4.5}$$

where $A(\lambda_{exc})$ and $A(\lambda)$ are ABS coefficients in *(number of wells)*$^{-1}$. The experimental CW-PL spectra have been corrected using Eq. 4.5. When the correction is applied the change of slope disappears. This has been verified for all the samples. As an example, in Fig. 4.3 the corrected spectrum of sample 7864-E10 is shown by the blue line: the comparison with the

experimental spectrum evidences that the slope change has been removed, thus confirming that self-absorption affects the PL spectra of Ge/SiGe QWs.

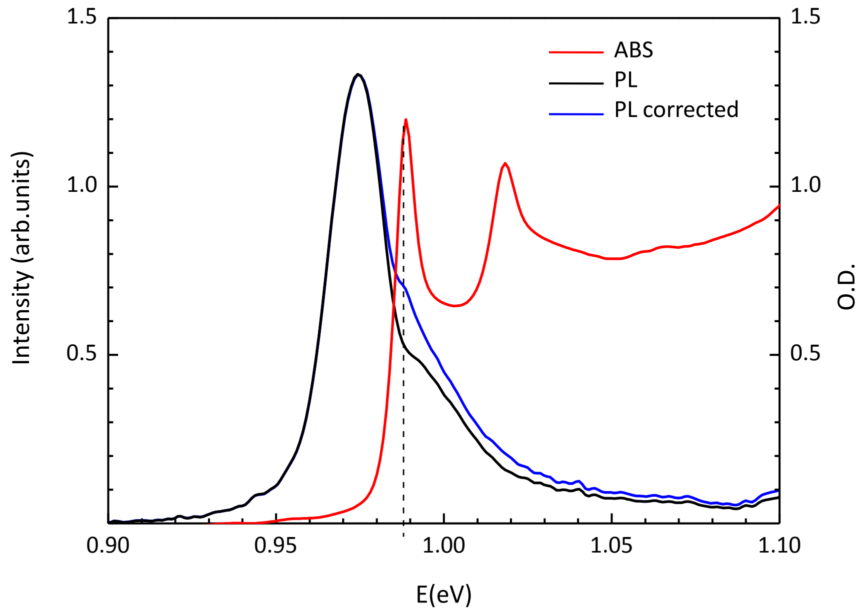


**Figure 4.3:** LT CW-PL spectrum of sample 7864-E10 corrected for self absorption (blue line). The experimental CW-PL (black line) and ABS (red line) spectra are also shown.

### 4.1.2 Emission from high energy states

In the LT CW-PL spectra of our Ge/SiGe MQWs structures at higher energy respect to the cΓ1-HH1 emission are usually present. The intensity of these structures is generally much lower than that of cΓ1-HH1 and the self-absorption correction does not affect significantly their shape and intensity. As an example, in Fig. 4.4 the CW-PL spectrum of sample 7864-E10, corrected for self-absorption, is reported on a logarithmic scale: the cΓ1-HH1 transition is present at 0.975 eV and a weaker peak at 1.105 eV is clearly visible. Its intensity is about one order of magnitude lower than that of the cΓ1-HH1 emission. A comparison with the ABS spectrum suggests its attribution to the cΓ2-HH2 emission, due to the proximity of the two structures in the PL and ABS spectra. The presence of transitions between confined QW states with $n > 1$ in PL spectra is not commonly observed, but it is reported in some literature works, such as Ref. [113] for GaAs/AlGaAs MQWs and Ref. [114] for GaInNAs/GaAs QWs.

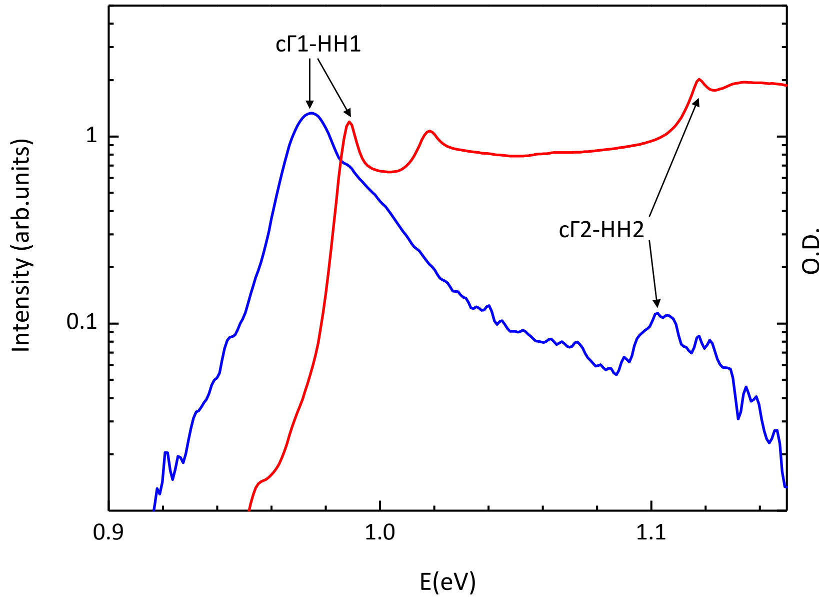


**Figure 4.4:** Self-absorption corrected CW-PL (black line) and ABS (red line) spectra of sample 7864-E10 at the lattice temperature T = 2 K. The cΓ2-HH2 emission is visible at 1.10 eV. Note the logarithmic scale.

The SS is observed even for the cΓ2-HH2 transition. In Fig. 4.5 CW-PL spectra of sample 8009-G7 at the lattice temperature of 5 K are reported for excitation power densities ranging from about 0.3 $kW/cm^2$ to about 3 $kW/cm^2$. When the maximum power density is used, a clear cΓ2-HH2 emission peak is visible at 1.029 eV and a carrier temperature of about 260 K can be estimated from the slope of the high energy tail of the cΓ1-HH1 peak. As the power density decreases, the high energy emission intensity decreases as well and finally disappears, and the carrier temperature reduces down to about 150 K. This behavior suggests that the observation of the cΓ2-HH2 emission could be attributed to a significant population of high energy states due to the carrier heating by the excitation.

Moreover, the ratio of the intensity of the two peaks depends on the energy distance between the cΓ1-HH1 and cΓ2-HH2 transitions and, in particular, it decreases as the energy distance increases, i.e. as $L_z$ diminishes. This behavior can be easily explained in terms of population of the states and supports the hypothesis that the presence in the spectra of the cΓ2-HH2 transition can be due to a high carrier temperature.

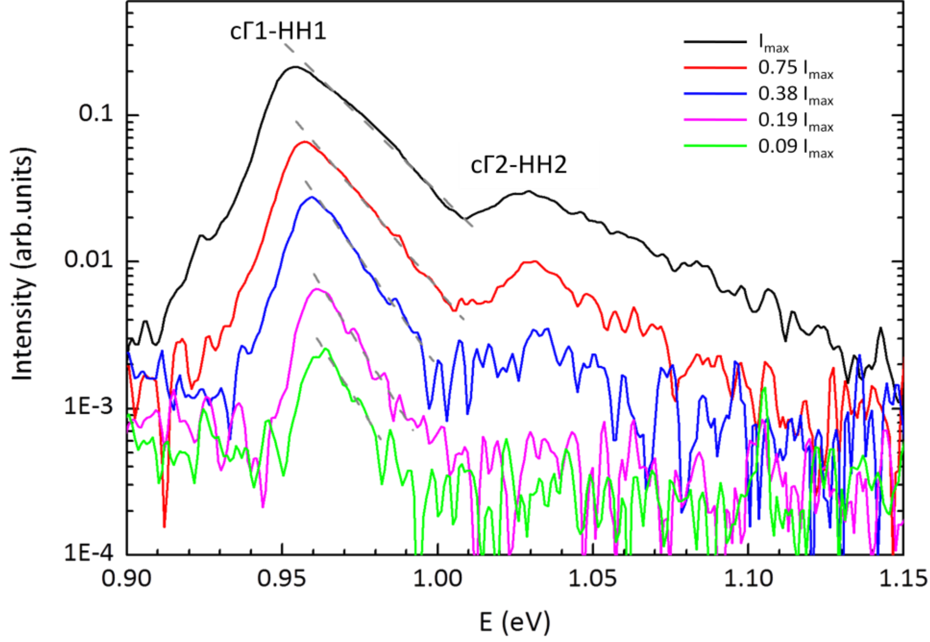


**Figure 4.5:** CW-PL spectra of sample 8009-G7 at the lattice temperature of 5 K with different exciting power density ($I_{max}$ = 3 kW/cm$^2$).

Another feature of the spectra in Fig. 4.5 is the lack of the cΓ1-HH1 transition. The absence of a clear evidence of this transition is a common situation when samples are excited with the 1064 nm line. In our opinion, this can be due to two factors: the low oscillator strength of the cΓ1-LH1 transition and the intense high energy tail of the cΓ1-HH1 peak. As already mentioned in Section 3.1, the transitions involving LH states are characterized by a lower oscillator strength respect to those involving HH states. The selection rules provide matrix elements equal to $\frac{\pi}{\sqrt{2}}$ and $\frac{\pi}{\sqrt{6}}$ for direct transitions involving HH and LH states respectively [69] (see Section 2.3.1, Tab. 2.3). Since the emission probability is proportional to the square of the matrix element, the recombination probability of a transition to a final LH state is one third of that of the corresponding HH one. Moreover, the weak cΓ1-LH1 emission is usually superimposed on the intense high energy tail of the cΓ1-HH1 emission, and thus is difficult to identify.

In conclusion, the cΓ1-LH1 emission is expected to be observed in PL spectra. Nevertheless, our data show that the observation of this transition is very sensitive to the experimental conditions. Indeed, as will be discussed in Section 4.3.2, when different wavelengths and power densities are used for the sample excitation, a weak cΓ1-LH1 PL peak can be observed.

## 4.2 Temperature dependence of the CW-PL spectra

In Fig. 4.6 the CW-PL spectra of sample 8009-G7 at the lattice temperatures of 5 K and 300 K are shown. The ABS spectra of the same sample at the two temperatures are also reported. The RT PL spectrum evidences that the direct gap related emission (energy peak at 0.88 eV) is visible also at 300 K with an intensity which is one order of magnitude lower than that at LT. The observation of the direct emission at RT in an indirect gap system is interesting from a fundamental point of view; it also suggests that Ge/SiGe QWs may be promising candidates for light sources, such as lasers, with a material system that can be easily integrated on Si. Finally, it proofs the good structural quality of the LEPECVD-grown Ge/SiGe QWs under analysis. Consequently, a detailed analysis of the dependence of PL spectra on the lattice temperature has been performed, in order to clarify the mechanisms responsible for the observation of direct emission even at RT. In Fig. 4.7 PL spectra measured at selected temperatures are reported.

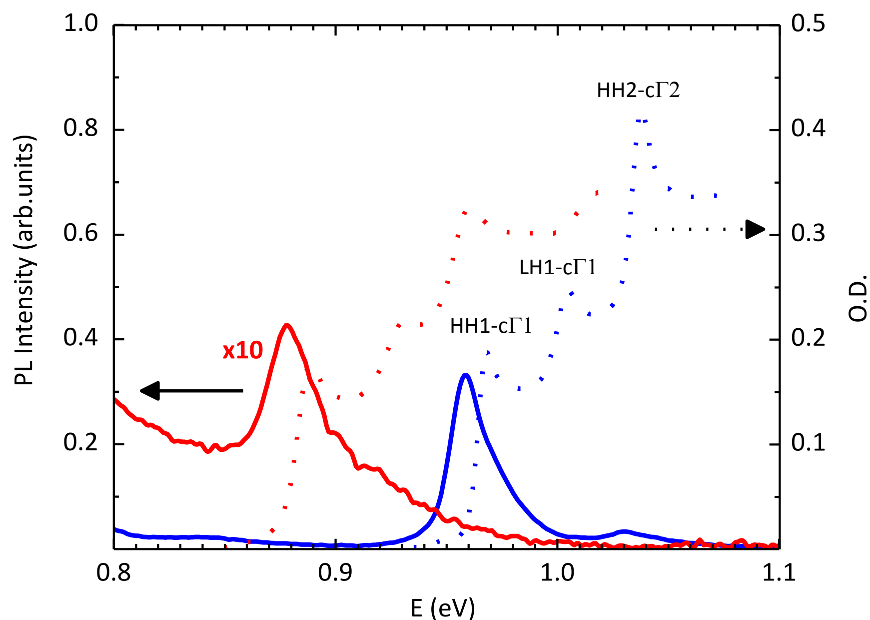


**Figure 4.6:** PL (full lines) and ABS (dotted lines) spectra of Ge/SiGe QWs (sample 8009-G7) at lattice temperatures of 5 K (blue lines) and 300 K (red lines).

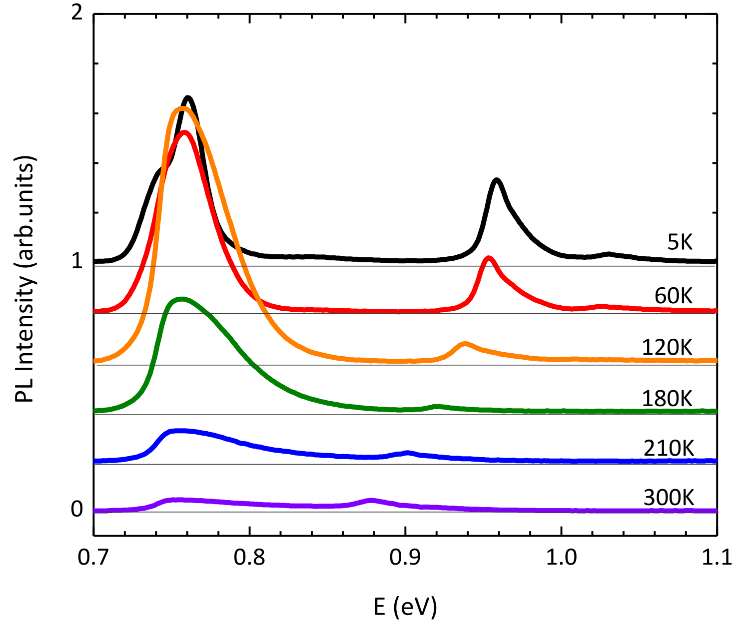


**Figure 4.7:** CW-PL spectra of sample 8009-G7 measured at selected temperatures between 5 K and 300 K. The indirect emission is only partially visible, due to the InGaAs detector cut-off at about 0.73 eV.

At 5 K the spectrum is analogous to that of sample 7864-E10 reported in Fig. 2.16. It is characterized by the indirect gap related peaks at about 0.73 eV (LA replica) and 0.76 eV (zero-phonon emission) and by the direct gap related peaks at 0.96 eV (cΓ1-HH1) and 1.03 eV (cΓ2-HH2). These measurements have been performed under resonant excitation conditions. As will be discussed in detail in Section 4.3, under these excitation conditions the electrons are directly promoted to the Γ-type states, from which they recombine giving rise to the direct emission. Furthermore, electrons can be very efficiently transferred from the Γ- to the L-type confined states by ultra fast mechanisms, mainly phonon scattering[34, 36, 115] (see Section 2.3.5), which make the indirect cL1–HH1 transition visible in the LT PL spectra.

Let us first consider the dependence of the direct emission on the lattice temperature. Increasing the temperature, the cΓ1-HH1 and cΓ2-HH2 structures red-shift, as expected. Their peak energy is reported as a function of the lattice temperature in Fig. 4.8: the temperature dependence is well fitted by Varshni's law with the parameters for the direct gap of bulk Ge given in Tab. 2.2. This indicates that confinement and strain do not affect significantly the dependence of the transition energies on the lattice temperature. The same result has been obtained also from ABS measurement, as reported in Section 2.1.2.[29] The integrated intensity of the direct emission ($I_{dir}$) as a function of the temperature is shown in Fig. 4.9. The

intensity first decreases and then, for temperatures higher than about 180 K, markedly increases.

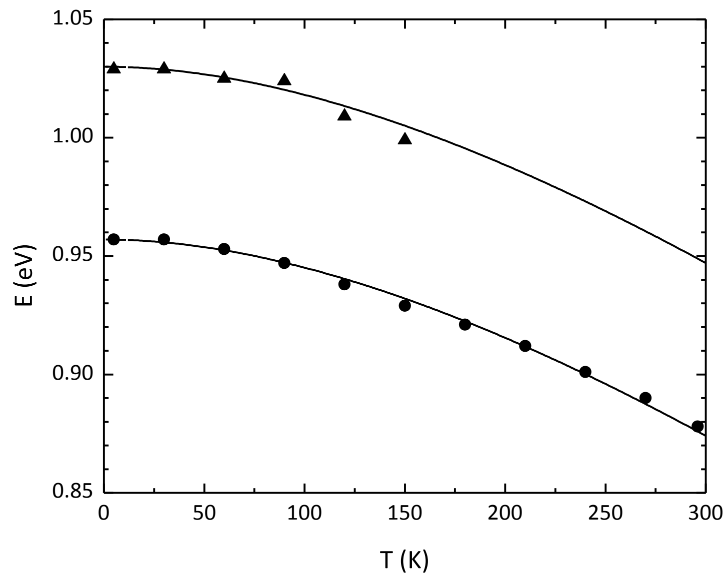


**Figure 4.8:** Peak energy of the cΓ1-HH1(circles) and cΓ2-HH2 (triangles) transitions as a function of the lattice temperature for sample 8009-G7. The temperature dependence of the direct gap of bulk Ge calculated using Varshni's law with the parameters reported in Ref. [28] is also reported (full lines).

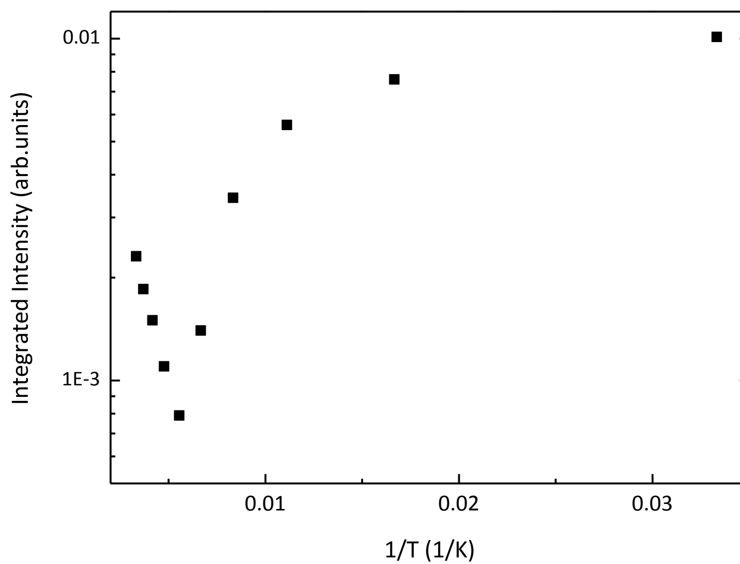


**Figure 4.9:** Integrated intensity of the cΓ1-HH1 peak as a function of the reciprocal temperature (sample 8009-G7).

Let us now move to the discussion of the indirect emission. The spectra in Fig. 4.7 have been measured using an InGaAs detector for a better signal-to-noise ratio, and thus are strongly

modified by the detector cut-off, mainly at high temperatures. Consequently, the actual shape of the indirect gap region has been measured in the whole temperature range using a PbS photoresistance (see Section B.2). Spectra at selected temperature are reported in Fig. 4.10: the temperature evolution of the indirect gap related emission is clearly visible. As the temperature increases, the FWHM of all the peaks increases. At temperatures higher than about 90 K it is not possible to resolve the different lines, and a broad band only is visible, which includes the zero-phonon line and the phonon replicas involving emission or absorption of a phonon (see, e.g., Fig. 4.10). The same behavior has been reported also in Ref. [89] for analogous Ge/SiGe QWs. This prevents from following the red shift of the cL1-HH1 zero-phonon transition with temperature.

The integrated intensity of the indirect region of the spectra ($I_{ind}$), measured with the PbS detector, is reported in Fig. 4.11. The intensity keeps constant up to about 40 K, slightly increases between 40 K and 60 K, and then monotonically decreases.

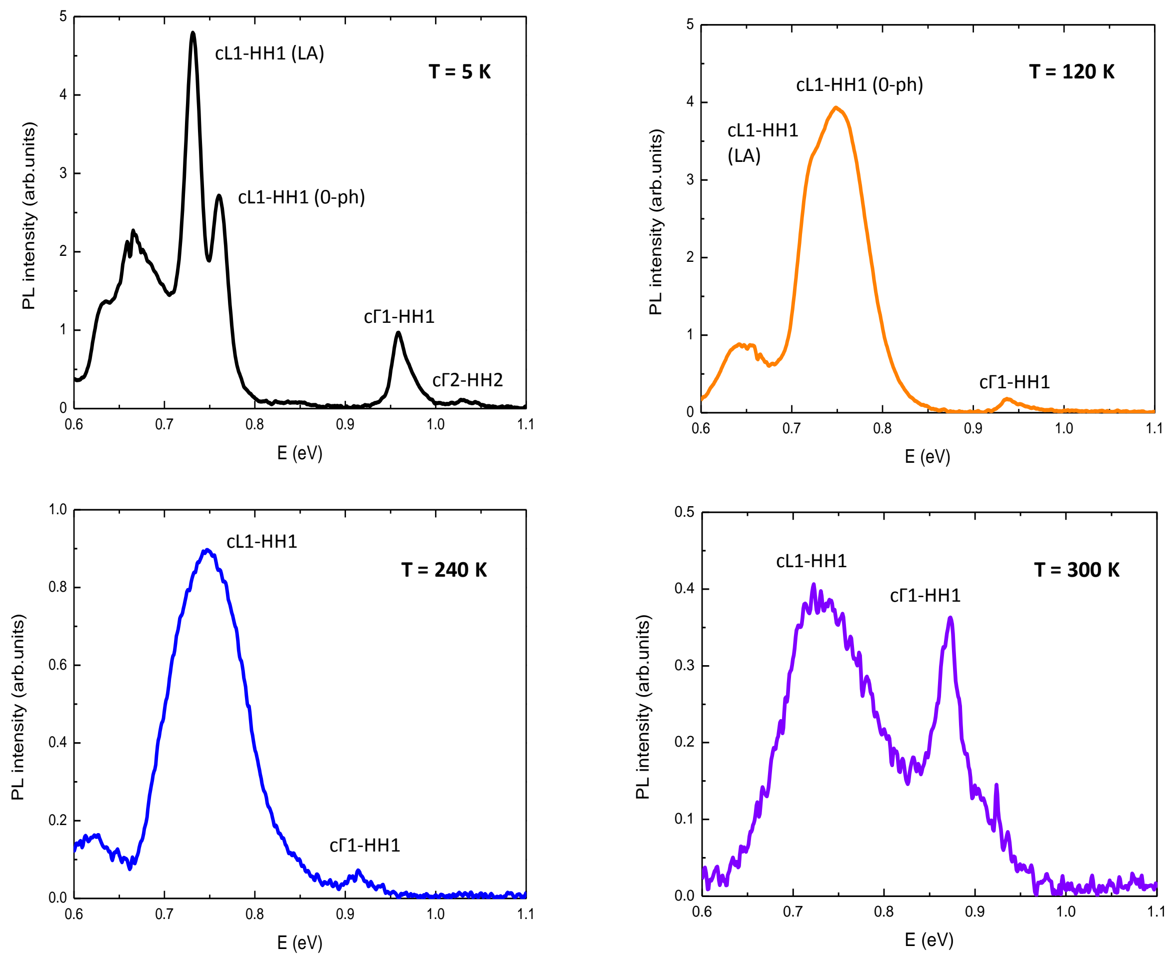


**Figure 4.10:** CW-PL spectra of sample 8009-G7 measured using the PbS detector at selected lattice temperatures.

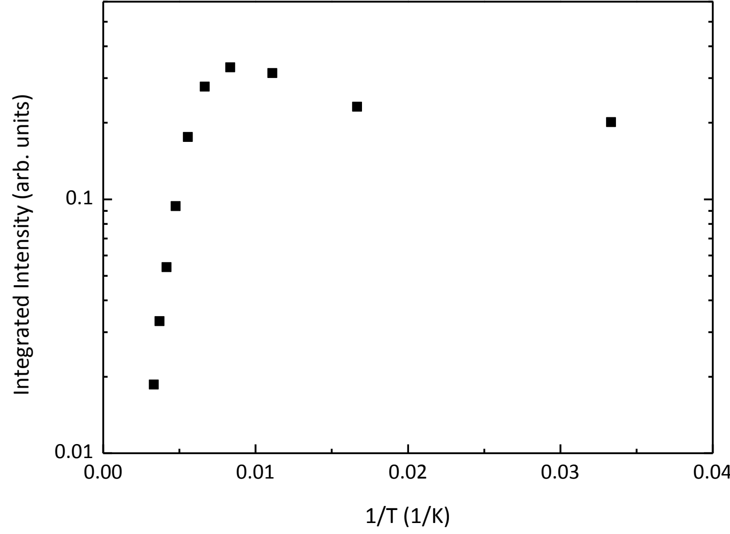


**Figure 4.11:** Integrated intensity of the indirect peaks as a function of the reciprocal temperature (sample 8009-G7).

If we assume that the non radiative processes equally affect the direct and the indirect radiative recombinations, the analysis of the ratio between $I_{dir}$ and $I_{ind}$ as a function of temperature allows to study the variation of the two transition rates with T neglecting non-radiative effects. The $I_{dir}/I_{ind}$ ratio is reported as a function of the reciprocal temperature in Fig. 4.12. Increasing the temperature, the $I_{dir}/I_{ind}$ ratio slowly decreases up to about 180 K and then markedly increases. These data suggest the presence of two different regimes. The initial reduction of the ratio as the temperature increases can be attributed to the increase of phonon population that enhances the Γ- to L-type states scattering by phonon interaction. The increase of the $I_{dir}/I_{ind}$ ratio at temperatures higher than about 180 K suggests that electrons can be thermally promoted from L- to Γ-type states. The linear fit of the data points of the Arrhenius plot at temperatures higher than 180 K (reported in Fig. 4.13) supports this hypothesis, and gives an activation energy ΔE of 170 ± 9 meV. The energy spacing between Γ and L minima at RT in Ge/SiGe MQWs can be estimated on the basis of the energy spacing between the cΓ1-HH1 peak and the cL1-HH1 zero-phonon line in the PL spectrum at 5 K (200 ± 4 meV, see Fig. 4.7). Taking into account the temperature dependence of the direct[28] and indirect[47] gap of bulk Ge as described by the Varshni parameters given in Table 2.2, an energy distance at RT $\Delta E_{\Gamma L}$ of 190 ± 10 meV between the first confined conduction state at Γ and the first confined conduction state at L can be obtained. This value is in a good agreement with the ΔE, and confirms that the direct gap PL at RT is due to the thermal promotion of electrons from L- to Γ-type states.

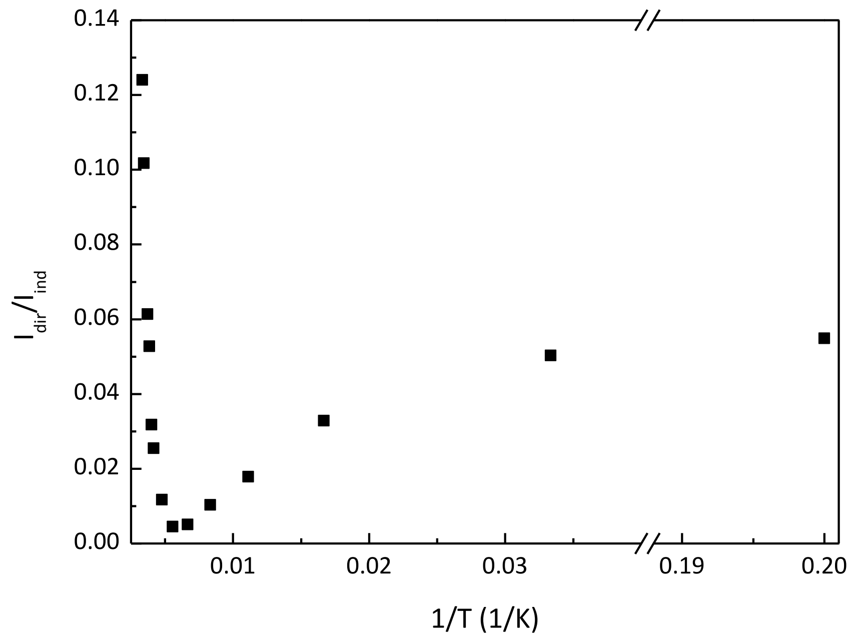


**Figure 4.12:** Ratio of the integrated intensity of the direct ($I_{dir}$) and indirect ($I_{ind}$) recombination as a function of the reciprocal temperature (sample 8009-G7).

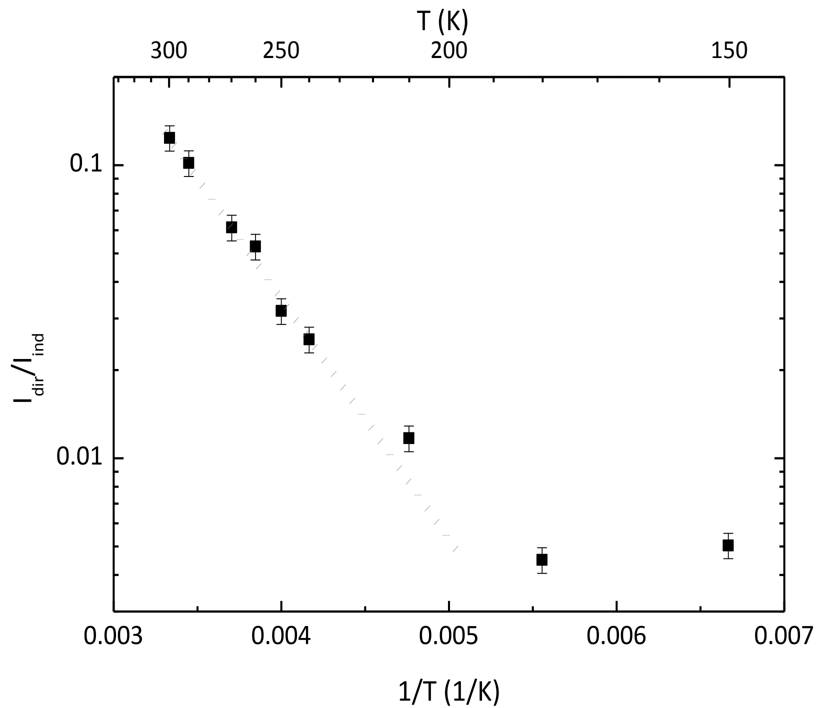


**Figure 4.13:** Ratio of the integrated intensity of the direct ($I_{dir}$) and indirect ($I_{ind}$) recombination as a function of the reciprocal temperature (sample 8009-G7). The linear fit of the experimental points is shown by the dotted grey line: the activation energy $\Delta E = 170 \pm 9$ meV is obtained.

The precision of the measured ΔE could be improved measuring PL spectra at temperatures higher than RT. However, the overall integrated intensity monotonically decreases as the temperature increases, due to thermal quenching (see Fig. 4.7) and this prevents from measuring the PL spectra at T > 300 K with a reasonable signal-to-noise ratio.

## 4.3 CW-PL spectra: resonant and non-resonant excitation conditions

As previously mentioned, the excitation conditions (resonant or non-resonant) strongly affect the features of PL spectra. In order to analyze the different thermalization paths of the carriers when the sample is excited resonantly and non-resonantly, CW-PL spectra were measured in the two excitation conditions with the same excitation power density (2 kW/cm$^2$) at the lattice temperatures of 5 K and 300 K.

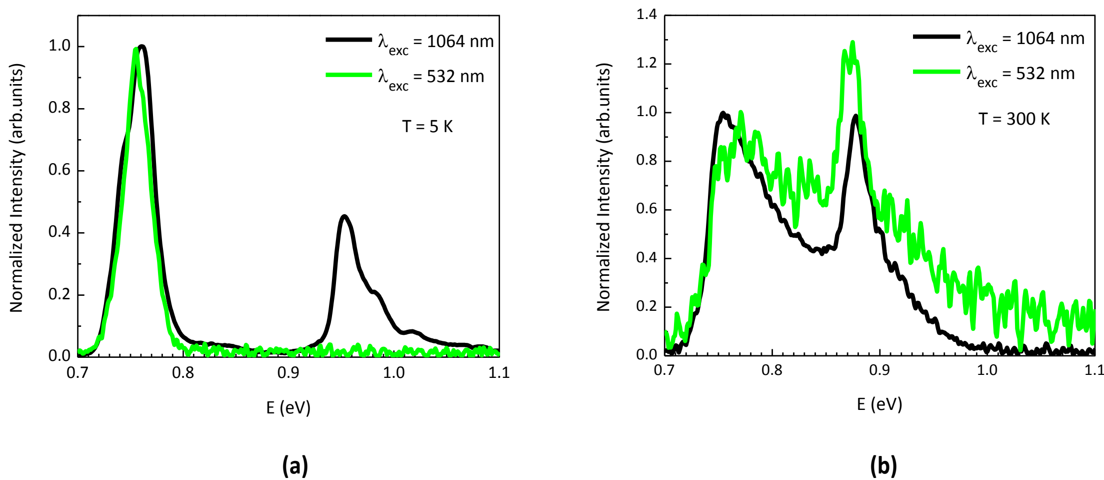


**Figure 4.14:** LT **(a)** and RT **(b)** CW-PL spectra of sample 7864-E5 under resonant (black lines) and non-resonant (green lines) excitation conditions. The spectra are normalized to the maximum of the zero-phonon line.

The spectra measured on the sample 7864-E5, reported in Fig. 4.14, indicate that:

(1) the overall PL intensity is strongly affected by the excitation conditions. When carriers are excited non resonantly ($\lambda_{exc}$ = 532 nm), the PL intensity is significantly lower than with resonant excitation ($\lambda_{exc}$ = 1064 nm); in non-resonant excitation conditions carriers undergo to non-radiative recombinations during the thermalization and diffusion in the barriers before reaching the L minimum. Due to

the low PL intensity in non-resonant excitation conditions, the spectra reported in Fig. 4.14 have been measured by the InGaAs detector.

(2) at 5 K (Fig. 4.14(a)) the indirect emission is visible in both the excitation conditions. The direct emission, on the contrary, is observed only when the sample is excited resonantly.

(3) at 300 K (Fig. 4.14(b)), analogous spectra are obtained in both the excitation conditions; i.e., the direct emission is visible also in non-resonant excitation conditions.

These experimental findings can be interpreted on the basis of the sketch of carrier dynamics of Fig. 4.15, in which the excitation, thermalization and recombination processes under the two excitation conditions are schematically shown. For simplicity, in Fig. 4.15 the first valence confined state (HH1) and the first conduction confined states at L (cL1) and at Γ (cΓ1) only are considered.

(1) At LT electrons excited resonantly to Γ-type confined states (Fig. 4.15(a)) can recombine giving rise to the direct cΓ1-HH1 recombination or can be efficiently scattered to L states, and then recombine giving rise to the indirect cL1-HH1 emission. On the other hand, electrons promoted to the continuum states of barriers and wells by non-resonant excitation (Fig. 4.15(b)), thermalize to the lowest energy states, i.e. the L-type confined states. Consequently, only the indirect cL1-HH1 emission can be observed.

(2) At RT the direct emission is visible in both resonant and non-resonant excitation conditions; moreover, the $I_{dir}/I_{ind}$ ratio is analogous for the two excitation conditions. This suggests that when the sample is excited non-resonantly electrons thermalized to L states can be thermally promoted to Γ type states (Fig. 4.15(d)), giving rise also to the cΓ1-HH1 emission. Similarly to the case of resonant excitation (see Section 4.2 and Fig. 4.15 (c)), a quasi-thermal equilibrium between L and Γ states is established at high temperatures.

In conclusion, the comparison between spectra obtained in resonant and non-resonant excitation conditions further supports the conclusions drawn in Section 4.2.

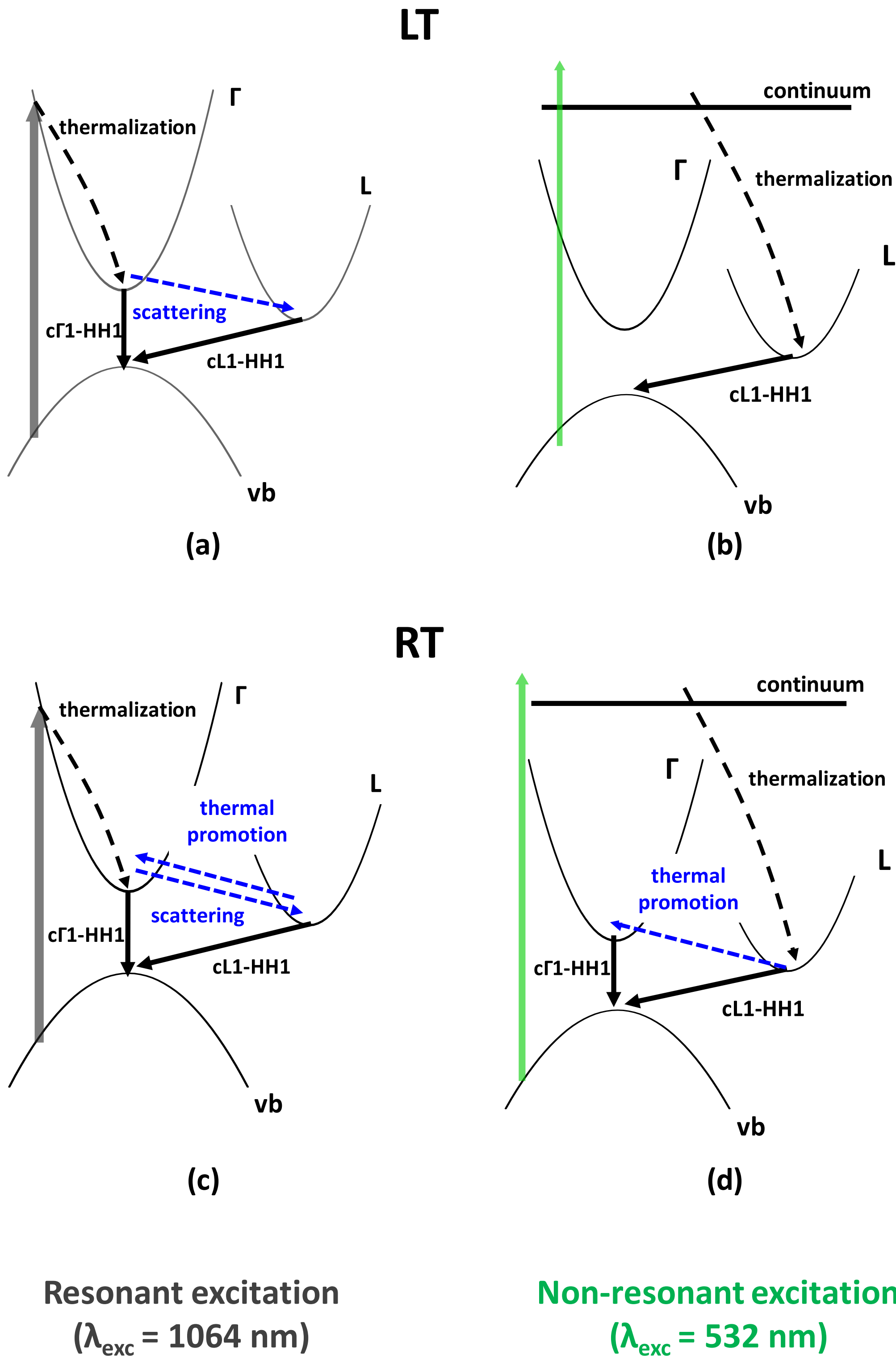


**Figure 4.15:** Schematic sketch of carrier dynamics when carriers are excited in resonant (**(a)**, **(c)**) or non-resonant (**(b)**, **(d)**) conditions at LT (**(a)**,**(b)**) and RT (**(c)**, **(d)**).

## 4.4 Photoluminescence and relaxation processes

This Section is devoted to the study of the intricate relaxation dynamics of carriers photoexcited resonantly to the Γ-type states of Ge/SiGe QWs. First, the results of TR-PL measurements of the direct gap related emission are presented: they are compatible with an efficient electron scattering from Γ- to L-type confined states. Then, a detailed analysis of the dependence of the direct gap related spectra on the excitation wavelength is discussed; the results of this analysis are interpreted assuming an efficient ultrafast inter-subband relaxation in competition with the intra-subband electron cooling. This analysis is also corroborated by the pump-probe TR ABS measurements in the ultrafast time regime.

### 4.4.1 Decay time of the direct recombination

The study of the decay time of the direct emission was performed on different samples under resonant excitation conditions with a temporal resolution of 1.5 ps. Details on the experimental setup can be found in Section B.3.3.

A typical result is shown in Fig. 4.16: the decay curve of the cΓ1-HH1 transition reproduces the laser pulse. This indicates that the depletion of Γ-type states is characterized by decay times equal or shorter than the time resolution of the experimental setup; the time resolution of our apparatus is much shorter than the direct gap related radiative recombination, which is expected to be of the order of hundreds of ps or ns, as suggested by literature works on type-I direct gap QWs based on III-V semiconductors [96 - 99].

Thus, our results indicate that the decay time of the Γ states is determined by the Γ-L scattering discussed in Section 2.3.5. TR pump-probe literature results on Ge/SiGe QWs show that the efficient phonon assisted electron scattering from Γ-type to L-type states is characterized by times in the order of 200-300 fs[25, 34], i.e., much shorter than the time resolution of our setup.

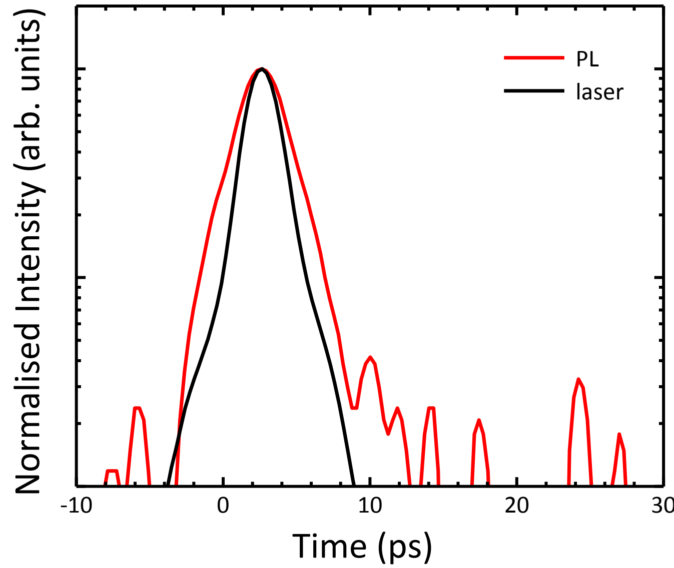


**Figure 4.16:** PL decay of the cΓ1-HH1 emission (red line) of sample 7864-E5 at the lattice temperature of 10 K. The laser pulse is also shown as a reference by the black line.

### 4.4.2 Spectra as a function of the excitation wavelength

In order to investigate thoroughly the relaxation and recombination processes in Ge/SiGe QWs, PL measurements as a function of $\lambda_{exc}$ have been performed at LT. Details on the experimental setup can be found in Section B.4. The experimental results related to one sample only (7864-E3) are presented, in order to simplify the discussion of the observed phenomena. Anyway, the same measurements have been performed on different samples, with fully analogous results.

The LT CW-PL spectrum of sample 7864-E3, measured with the excitation wavelength $\lambda_{exc}$ = 900 nm and a power density of 3.5 kW/cm$^2$, is shown in Fig. 4.17 by the green line. It reproduces all the features typical of the LT PL spectra of Ge/SiGe MQWs previously described (Sections 2.3.4 and 4.1). The cΓ1-HH1 emission appears at about 1.06 eV, while the indirect gap related peaks are found at 0.80 eV and 0.77 eV (zero-phonon line and the LA phonon replica, respectively). The LT linear ABS spectrum is shown as grey area, for reference. LT PL spectra measured using different $\lambda_{exc}$ from 900 to 870 nm keeping constant the exciting power density (3.5 kW/cm$^2$) are also reported in Fig. 4.17. The cΓ1-HH1 peak is observed in all the spectra at about 1.06 eV. However, for excitation wavelengths shorter than 900 nm an additional PL peak appears on the high energy side of the cΓ1-HH1 transition. In the following, this signature is referred to as "satellite" of the direct gap transition. The energy position and the intensity of the satellite strongly depend on $\lambda_{exc}$. As $\lambda_{exc}$ increases, the satellite peak energy gets closer to the cΓ1-HH1 energy; finally, at $\lambda_{exc}$ = 900 nm the two peaks merge.

At the same time, the integrated intensity of the direct emission increases as $\lambda_{exc}$ increases from 870 to 900 nm; at $\lambda_{exc}$ = 900 nm the integrated intensity reaches a maximum. In particular, the intensity increase is stronger for the satellite than for the cΓ1-HH1 peak. Asides, the shape as well as the intensity of the indirect gap related PL is not affected by the variation of $\lambda_{exc}$.

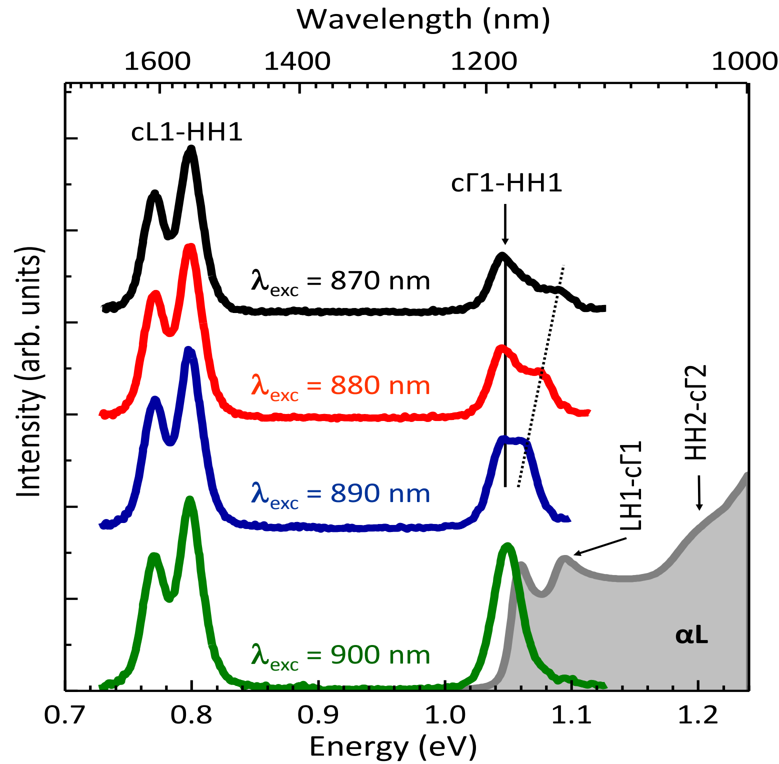


**Figure 4.17:** CW-PL spectra (solid lines) of sample 7864-E3 at the lattice temperature of 10 K for different $\lambda_{exc}$ between 870 and 900 nm. The spectra are offset for clarity. The energy position of the satellite peak of the cΓ1-HH1 transition is indicated by the dotted line. The ABS spectrum at the same lattice temperature is also reported as a reference by a grey area.

For a systematic analysis of the direct emission, the LT PL spectra have been measured in the spectral range of the direct transitions (1.03 - 1.20 eV) varying $\lambda_{exc}$ between 840 and 1010 nm in steps of 10 nm, keeping constant the excitation power density at 3.5 kW/cm$^2$. The spectra are shown in Fig. 4.18(a).

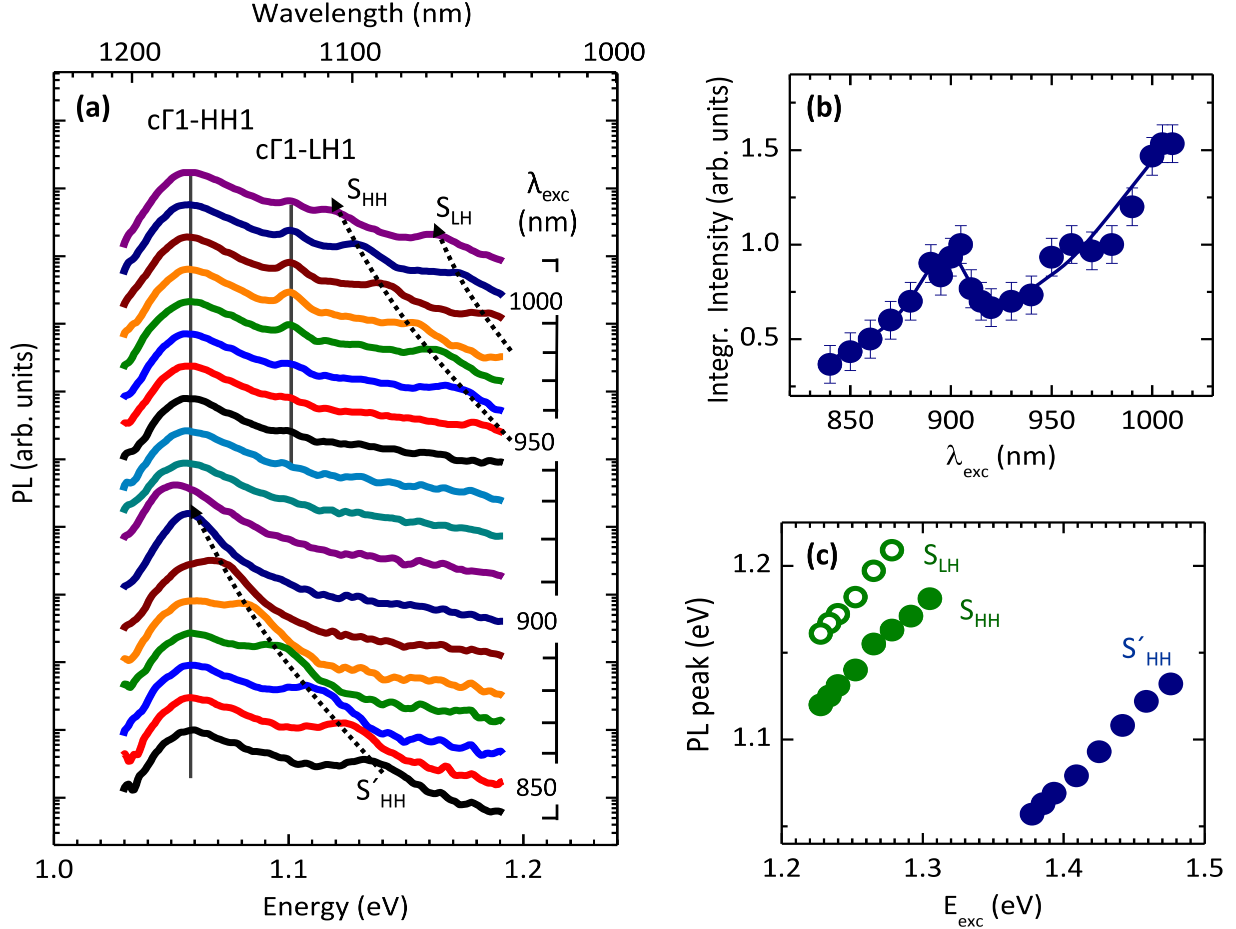


**Figure 4.18: (a)** CW-PL spectra of sample 7864-E3 measured at $\lambda_{exc}$ between 840 and 1010 nm at the lattice temperature of 10 K. All the spectra are normalized at the maximum of the cΓ1-HH1 emission and shifted for an easier comparison. **(b)** PL intensity, integrated over the full spectral range, as a function of $\lambda_{exc}$. **(c)** Peak energy of the satellites plotted versus the exciting photon energy.

As expected, the cΓ1-HH1 peak is present in all spectra at about 1.06 eV. For the lowest excitation wavelength ($\lambda_{exc}$ = 840 nm), a satellite ($S'_{HH}$) appears at 1.13 eV. Again, the position of this peak depends on $\lambda_{exc}$: the satellite gets closer to the cΓ1-HH1 transition as $\lambda_{exc}$ increases. At the same time, the PL intensity, integrated over the full investigated spectral range (1.03 - 1.12 eV), increases (Fig. 4.18(b)). The two peaks merge for $\lambda_{exc}$ = 900 nm; at this $\lambda_{exc}$ the integrated intensity reaches a local maximum (Fig. 4.18(b)). Further increasing $\lambda_{exc}$, the cΓ1-LH1 transition, identified on the basis of the ABS spectrum (see Fig. 4.17), becomes visible at about 1.10 eV. For $\lambda_{exc}$ > 920 nm, the overall intensity rises again with increasing $\lambda_{exc}$ and two new satellite peaks ($S_{HH}$ and $S_{LH}$) appear. As in the case of $S'_{HH}$, their spectral position depends on $\lambda_{exc}$. The peak energy of $S'_{HH}$, $S_{HH}$, and $S_{LH}$ is plotted as a

function of the exciting photon energy in Fig. 4.18(c). The energy of all the satellites shows a linear dependence on the excitation energy with a slope close to 1.

The experimental evidences reported in Figs. 4.17 and 4.18 can be interpreted assuming that relaxation and recombination in resonatly excited Ge/SiGe MQWs are determined by the processes sketched in Fig. 4.19. For simplicity, only the first (cΓ1) and the second (cΓ2) subbands are considered.

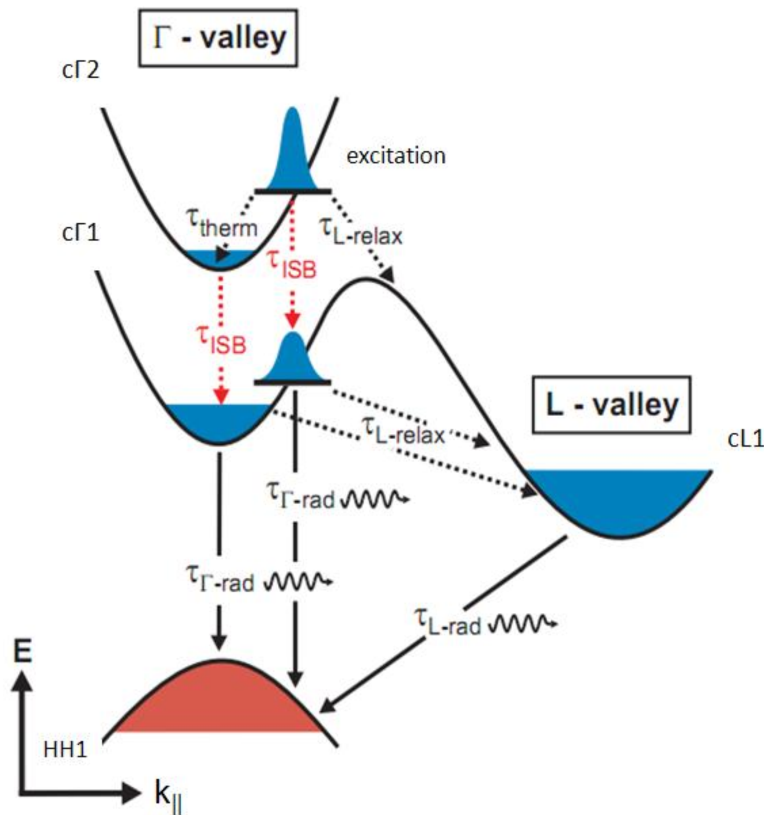


**Figure 4.19:** Schematic picture of scattering, thermalization and recombination processes that occur in Ge/SiGe QWs when electrons are excited to the continuum of a Γ-type subband.

When electrons are resonantly excited to the continuum of one subband, for instance the second one, three processes occur: inter-valley scattering to the L-type states with a characteristic time $\tau_{L\text{-relax}}$, thermalization towards the subband bottom with a characteristic time $\tau_{therm}$, and inter-subband scattering to the continuum of the first subband with a characteristic time $\tau_{ISB}$. As discussed in Section 2.3.5 and in Refs. [25] and [36], phonon-assisted inter-valley scattering to the L-type states is an extremely efficient relaxation channel for the electrons, due to the high density of states in L. The large effective mass of the L

minimum and its four-fold degeneracy make the density of states of the L valley about two orders of magnitude larger than that of the Γ valley. This leads to a scattering time $\tau_{L\text{-relax}}$ of the order of 200-300 fs for Γ- to L-type states relaxation.[25, 34] Electrons scattered to L can then recombine radiatively giving rise to the cL1-HH1 emission with a typical decay time of the order of 10 ns, as discussed in detail in Chapter 3. Intra-band thermalization times ($\tau_{therm}$) are expected to be of the order of 0.5 – 1.0 ps.[116] Indeed, pump-probe measurements reported in the literature[25, 36] confirm that thermal distribution is reached on this time scale, which is rather long compared to sub-100 fs thermalization time in GaAs.[117] Electrons that reach the bottom of the cΓ1 subband can recombine radiatively, giving rise to the direct gap emission. Considering different literature works on direct gap QWs based on III-V semiconductors (see, e.g., Refs. [96, 98]), intrinsic recombination times for the direct gap related recombination ($\tau_{\Gamma\text{-}rad}$) are supposed to be of the order of hundreds of ps. However, as shown in Section 4.4.1, the decay time of the direct gap PL is limited by the inter-valley scattering to the L-states. If the thermalization time is longer than the inter-subband scattering time ($\tau_{ISB}$), photo-excited electrons in the continuum of the cΓ2 subband quickly scatter towards the continuum of the cΓ1 subband. Then, before the thermalization and cooling to the bottom of the subband occur, they can recombine radiatively giving rise to the observed satellite peaks on the high energy side of the direct band gap PL. Obviously, when electrons are excited resonantly to the bottom of the cΓ2 subband, no satellite peaks appear.

We move now to the discussion of all the features observed in the PL spectra as a function of $\lambda_{exc}$ reported in Figs. 4.17 and 4.18. First, the shape as well as the intensity of the indirect gap PL is not affected by $\lambda_{exc}$ (Fig. 4.17). This confirms that the effects under analysis are mainly governed by electrons. The $S'_{HH}$ satellite is visible for $\lambda_{exc} < 900$ nm and then merges with the cΓ1-HH1 peak. This suggests that at $\lambda_{exc} < 900$ nm the electrons are excited to the continuum of the cΓ3 subband and the satellite $S'_{HH}$ peak becomes visible due to the ultrafast inter-subband scattering to the continuum of the cΓ1 subband. As $\lambda_{exc}$ increases and thus approaches the resonance with the HH3-cΓ3 transition, the spectral position of the satellite peak gets closer to the cΓ1-HH1 peak. Finally, at $\lambda_{exc} = 900$ nm the $S'_{HH}$ satellite merges with the cΓ1-HH1 peak. The results of 8×8 **k·p** calculations[c] performed with the structural data of sample 7864-E3 (see Section B.1.2) support this interpretation, giving an energy for the HH3-cΓ3 transition of about 900 nm. For $\lambda_{exc} > 900$ nm, electrons are promoted to the cΓ2

[c] In this sample the energy of the cΓ3-HH3 transition cannot be deduced from ABS spectra because of the VS absorption.

continuum and analogous features are observed as the electrons scatter to the cΓ1 subband. Two satellite peaks, $S_{HH}$ and $S_{LH}$, are visible. Since the energy distance between the two satellites is compatible with the energy distance between the cΓ1-HH1 and cΓ1-LH1 peaks, the $S_{HH}$ and $S_{LH}$ peaks are attributed to the cΓ1-HH1 and cΓ1-LH1 transitions within the electron-hole continuum, respectively.

Also the integrated PL intensity dependence on $\lambda_{exc}$ (see Fig. 4.18(b)) can be interpreted on the basis of the proposed picture. As $\lambda_{exc}$ increases and approaches the HH3-cΓ3 transition, the intensity of both the $S'_{HH}$ satellite and the cΓ1-HH1 peak increases. This can be explained considering two factors: the less efficient Γ to L scattering and the higher hole availability. Since the inter-valley scattering is faster for electrons with higher momenta[36], it becomes less effective when the electrons are excited closer to the $\mathbf{k}_{||} = 0$ transition. Also, the higher hole density in the proximity of Γ favors the recombination of non-thermal electrons, yielding an enhancement of the $S'_{HH}$ satellite peak. When $\lambda_{exc}$ is such to excite electrons in the continuum of the cΓ2 subband, the fraction of non-thermal electrons with higher momenta increases leading to an abrupt decrease of the PL intensity.

In addition, the linear dependence of the satellite energy position on the excitation energy shown in Fig. 4.18(c) is justified by the fact that subbands for $Ge/Si_{0.15}Ge_{0.85}$ QWs around Γ in both the conduction and the valence bands are nearly parallel, as predicted by tight-binding calculations (see Fig. 2.10).

As previously mentioned, different samples have been analyzed, fully reproducing the results of sample 7864-E3 we have discussed. The energy of the PL structures and the $\lambda_{exc}$ at which the satellites merge with the cΓ1-HH1 peak (i.e., the resonance with a cΓ*n*-HH*n* transition) change from sample to sample in agreement with the variation of the confinement energies with the QW thickness.

PL spectra measured as a function of the excitation power density at a fixed $\lambda_{exc}$ (Fig. 4.20(a)) provide some insight on the mechanism responsible for the inter-subband relaxation. In Fig. 4.20(b), the integrated PL intensity of the cΓ1-HH1 peak and of the $S'_{HH}$ satellite is plotted as a function of the exciting power. The integrated intensity shows a slightly super-linear dependence of the cΓ1-HH1 emission on the exciting power density, and an almost quadratic dependence for $S'_{HH}$.

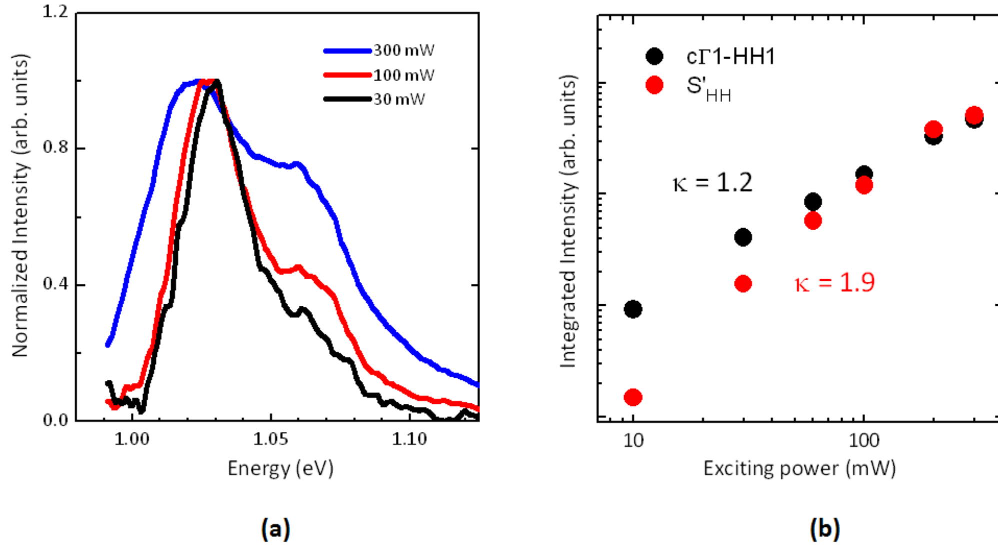


**Figure 4.20: (a)** Normalized CW PL spectra of sample 7864-E5 for different exciting powers. **(b)** Integrated intensity of the cΓ1-HH1 peak (black dots) and the S'$_{HH}$ satellite (red dots) as a function of the exciting power.

The nearly quadratic dependence of S'$_{HH}$ integrated intensity suggests that the electron inter-subband relaxation may occur via Coulomb scattering. On the other hand, the negligible momentum transfer for the observed inter-subband scattering points to radiative transitions. The satellite intensity is higher for excitation of the third in contrast to the second subband, as expected for intersubband radiative transitions according to the dipole selection rules. Thus, this evidence may support the later hypothesis. Indeed, the transition between lowest and third subband is allowed while it is forbidden between neighboring subbands due to the wavefunction symmetry. Therefore, Coulomb- and radiative scattering could contribute both to the inter-subband relaxation.

### 4.4.3 TR pump-probe ABS measurement

A further experimental confirmation of the model for the relaxation process proposed in previous Section (Fig. 4.19) is provided by the TR analysis of carrier dynamics in the ultrafast regime. Time-resolved LT pump-probe ABS measurements with a resolution better that 50 fs have been performed. Details on the experimental setup can be found in Section B.5.

The results obtained for sample 7864-E3 are shown in Fig. 4.21. A pump wavelength of 990 nm (1.25 eV) has been chosen, which is about 50 meV higher than the cΓ2-HH2 transition but lower than the cΓ3-HH3 transition. Electrons are consequently pumped into the continuum of the cΓ2 subband. The LT CW-PL spectrum obtained for the same $\lambda_{exc}$, is reported on top of Fig 4.21(b) for a direct comparison.

Fig. 4.21(a) shows the two-dimensional plot of the differential absorption (ΔαL) as function of photon energy and time delay between the pump and the probe pulses (Δt). The linear ABS is also shown at the top of the Figure for reference. Selected ΔαL spectra, offset for clarity, are plotted in Fig. 4.21(b) for different Δt. At positive Δt values the ΔαL spectra at the excitonic resonances cΓ1-HH1 and cΓ1-LH1 show a shift to lower energies due to the band-gap renormalization as well as bleaching as a result of Pauli-blocking due to the population.[118] The latter increases with Δt, as expected. Altogether, the ΔαL features of the main excitonic transitions correspond well to the reported behavior of Ge/SiGe QWs.[34, 36] Further, the initial bleaching on the high energy side of the cΓ1-HH1 and cΓ1-LH1 transitions at Δt = 0, clearly visible, is due to the population created by the pump pulse at 1.25 eV ($\lambda_{exc}$ = 990 nm). A distinct bleaching feature then appears about 60 - 90 fs after the pump pulse at 1.14 eV, which corresponds to the energy of the satellite $S_{HH}$ observed in the PL spectrum for the same $\lambda_{exc}$.

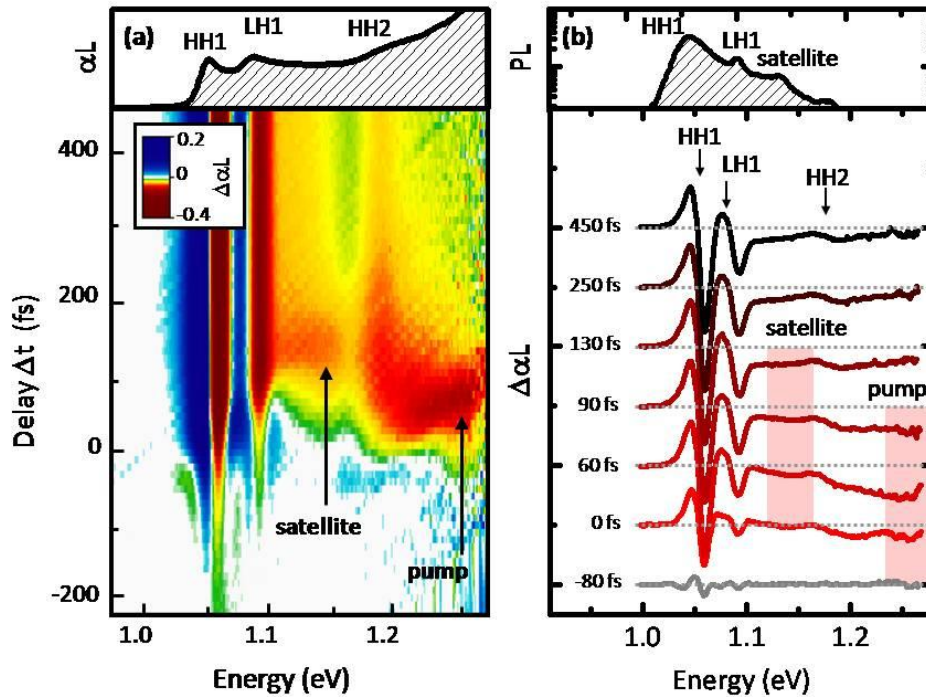


**Figure 4.21: (a)** Top: linear ABS spectrum. Bottom: differential ABS in false color scale for excitation in the continuum of the cΓ2 subband. **(b)** Top: LT PL spectrum at $\lambda_{exc}$ = 990 nm (= 1.25 eV). Bottom: differential ABS (ΔαL) spectra for selected Δt. All the measurements refer to sample 7864-E3and were performed at the lattice temperature of 10 K.

This evidence confirms the interpretation of CW-PL measurements proposed in the previous Section. As it is schematically shown in Fig. 4.22, a bleaching is expected in a pump-probe ABS measurement due to the ultrafast inter-subband electron scattering about 100 fs after the pump pulse. The experimental results confirm the expected behavior: when electrons are excited in the continuum of the cΓ2 subband at 1.25 eV, they scatter to the continuum of the cΓ1, giving rise to a bleaching of the absorption centered at 1.14 eV. Indeed, this energy is in a very good agreement with the satellite peak energy when PL is excited by $\lambda_{exc}$ = 990 nm, corresponding to a photon energy of 1.25 eV. This result clearly shows that the PL emission at the energy of the satellite peak is caused by a non-thermal carrier population in the continuum of the first subband. The pump-probe measurements provide the time scale of the inter-subband relaxation in the range of 100 fs. The bleaching then persists for $\Delta t < 250$ fs, corresponding to the Γ-to-L scattering time in Ge/SiGe QWs. [25, 34]

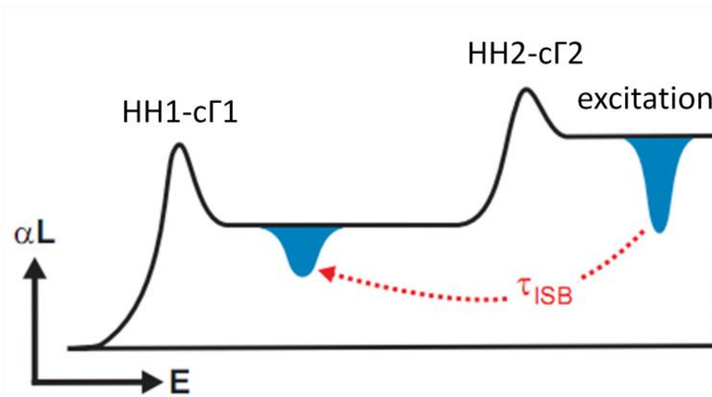


**Figure 4.22**: Sketch of a typical ABS spectrum of Ge/SiGe QWs. Blue areas schematically show the features expected in pump-probe ABS measurements: when exciting in the continuum of the cΓ2 subband a bleaching is expected also in the continuum of the cΓ1 subband due to the ultrafast electron inter-subband scattering.

## 4.5 Conclusions

In this Chapter the direct gap related cΓ1-HH1 emission in Ge/SiGe QWs has been investigated and the typical features of the direct region of PL spectra have been studied: Stokes shift, self-absorption and emission from states with $n > 1$ have all been observed.

RT direct gap related emission in Ge QWs, i.e. in an indirect gap system, has been demonstrated. The study of the temperature dependence of CW-PL spectra has shown that a thermal promotion of electrons from L to Γ states occurs for temperatures higher than 180 K. These results have been corroborated by the comparison between spectra obtained in resonant

and non resonant excitation conditions. This proves that Ge/SiGe MQWs are interesting potential condidates for the integration of light emitters on the Si-platform.

In the second part of the Chapter, the rich carrier dynamics in Ge/SiGe QWs has been explored through TR-PL, CW-PL as a function of $\lambda_{exc}$ and ultrafast pump-probe measurements. TR-PL data have shown that the depletion of Γ states is dominated by the efficient and ultrafast phonon assisted scattering towards L states. Evidence of inter-subband scattering of electrons at Γ in the femtosecond regime has been provided; this inter-subband scattering is competitive with the intra-subband thermalization and with the scattering towards L-type states. The intricate interplay between these different relaxation processes yields spectral features different respect to the commonly observed emission in GaAs-based QWs. This is due to the different time scales typical of the Ge system. An overall description of the intricate relaxation and recombination dynamics in Ge/SiGe QWs when electrons are excited resonantly into Γ-type states at $\mathbf{k}_{//} \neq 0$ at low lattice temperature is presented at the end of the Chapter.

# Chapter 5

# Conclusions

A wide experimental study of the recombination processes and of the carrier dynamics of compressively strained Ge/SiGe QWs with Ge-rich barriers has been presented. Ge/SiGe QWs are a new system characterized by optical and electronic properties different from those commonly observed in the more widely studied QWs based on III-V semiconductors. These peculiar properties are due to the type-I band alignment for both the Γ− and the L-type states[15] and to the small energy distance between the direct and the indirect bad gap in Ge, which provides Ge/SiGe QWs with a so-called quasi-direct gap (i.e., transitions at the centre of the Brillouin zone strongly influence the optical properties of the system). This behavior has been proved in the literature by the dominance of direct gap related HH$n$-cΓ$n$ transitions in ABS spectra,[16, 17, 29] and by the observation of both direct cΓ1-HH1 and indirect cL1-HH1 emission with comparable intensities in the same PL spectrum.[15] Moreover, Ge/SiGe QWs with Ge-rich barriers are compatible with the CMOS technology, resulting promising candidates for the integration of good optical properties on the Si-platform.

Different optical spectroscopy techniques have been used: continuous-wave photoluminescence (CW-PL), time-resolved photoluminescence (TR-PL), linear absorption, and time-resolved pump-probe spectroscopy. Measurements as a function of different parameters, such as QW thickness, lattice temperature, excitation power density and excitation wavelength have all been performed for the analysis of the different processes. The main results of this work can be summarized as follows.

- CW-PL measurements in resonant and non-resonant excitation conditions at different lattice temperatures give evidence of the different thermalization paths, contributing to clarify the mechanisms which are at the basis of the observation of the direct gap related emission.
- Results concerning the intervalley scattering between Γ- and L-type states are obtained through different experimental techniques. At LT, carriers promoted to Γ-

type states are very efficiently scattered to L-type states, as confirmed by our TR-PL results and by TR pump-probe measurements reported in literature[25, 34]. At RT carriers scattered to L are thermally promoted back to Γ-type states and a quasi-thermal equilibrium is established between the two states, as shown by CW-PL measurements as a function of the lattice temperature.

- Carrier relaxation processes have been studied through CW-PL measurements as a function of the excitation wavelength, corroborated by TR pump-probe ABS measurements in the fs regime, which evidence the ultrafast inter-subband electron relaxation at Γ competitive with the intravalley thermalization and the efficient scattering towards L-type states.
- The first detailed study of the decay times of both the direct and the indirect gap related recombination is carried out through TR-PL measurements. The dependence of the decay time of the indirect emission on QW thickness and lattice temperature is also analyzed.

Fig. 5.1 summarizes the main results obtained in this study of the carrier recombination and dynamics.

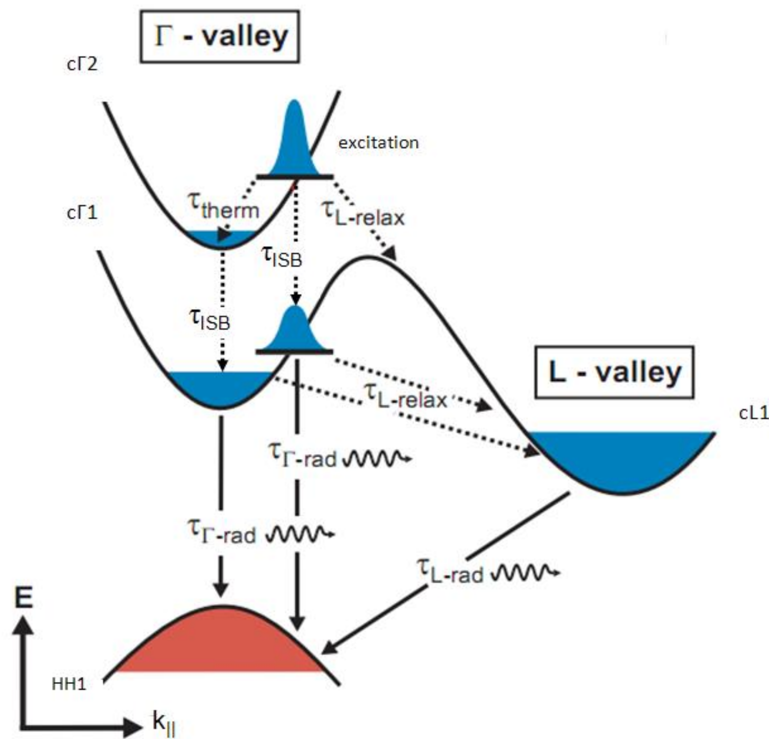


**Figure 5.1:** Schematic picture of scattering, thermalization and recombination processes that occur in Ge/SiGe QWs when electrons are excited to the continuum of a Γ-type subband at low lattice temperature.

Let us consider carriers resonantly excited to quantum confined states at Γ at low lattice temperature. When electrons are excited to states of a Γ-type subband with $\mathbf{k}_{||} \neq 0$, three processes occur.

(1) Electrons are very efficiently scattered to L-type states through phonon interaction; typical scattering times ($\tau_{L\text{-relax}}$) are of the order of 200-300 fs, as shown by recent literature results.[25] Once they have reached the L-valley, electrons can recombine radiatively giving rise to the indirect cL1-HH1 emission. As shown in Chapter 3, typical decay times of the indirect recombination ($\tau_{L\text{-rad}}$) are of the order of 10 ns, and depend on both QW thickness and lattice temperature.

(2) Electrons can thermalize to the bottom of the subband; typical intravalley thermalization times ($\tau_{therm}$) of the order of 0.5 - 1 ps have been measured for bulk Ge in Ref. [116]. Then, they can recombine radiatively, giving rise to the direct emission. The strongest direct transition in PL spectra is the cΓ1-HH1. High energy recombinations, such as cΓ1-LH1 and cΓ2-HH2 emission, can also be observed, depending on the subband energy spacing and on the excitation conditions. In literature, typical decay times of 0.1 - 1 ns are found for the direct gap related recombination in type-I QWs based on III-V semiconductors (see, e.g., Refs. [96, 98]). In Ge/SiGe QWs, the decay times $\tau_{\Gamma\text{-rad}}$ can not be experimentally measured, as discussed in Section 4.4.1, since the depletion of Γ states is dominated by the Γ to L scattering.

(3) Furthermore, electrons can scatter to cΓ1 subband states with $\mathbf{k}_{||} \neq 0$, as discussed in Sections 4.4.2 and 4.4.3. Scattering times $\tau_{ISB}$ of the order of 50 - 100 fs have been measured through TR pump-probe ABS with a time resolution of tens of fs (Section 4.4.3). These measurements have also shown that a non-equilibrium carrier population persists in Γ-type subbands up to about 250 fs. This value is compatible with the literature value of $\tau_{L\text{-relax}}$[25].

In conclusion, the presented results contribute to the understanding of the intricate interplay between the different processes involved in the carrier dynamics of Ge/SiGe QWs, an indirect band-gap model system whose optical properties are strongly influenced by transitions at the center of the Brillouin zone. Ge/SiGe QWs are of particular interest also for their potential applications in optical interconnects integrated on Si: indeed, an efficient Quantum Confined Stark Effect[18, 19], RT electroluminescence[26], and transient optical gain[25] in these systems have all been recently demonstrated.

# Appendix A

# Electronic properties of quantum wells

In this Appendix the main effects of quantum confinement on the electronic states will be first summarized for an ideal (i.e. infinitely deep) QW and then extended to the case of real systems. Optical properties and excitonic effects will be also briefly reviewed. The aim of this Appendix is to provide references and notes useful for the discussion of the experimental results presented in Chapters 3 and 4. A detailed coverage of the properties of quantum confined systems and semiconductor nanostructures can be found in a number of books and papers, such as, e.g., in Refs. [70, 111, 119].

## A.1 Band alignment

Let us consider a heterostructure made of two semiconductors with different energy gaps. At the interface, the discontinuity of CB and VB generates a potential step.[d] Choosing properly the energy gap values, it is possible to confine electron and/or holes in a spatial region, thanks to the potential barrier they encounter at the interface. Carriers can be confined in one or more directions. A QW is formed by a layer of a semiconductor with low energy gap (*well*) embedded between two layers of another semiconductor with high energy gap (*barriers*): it is consequently a 2D system in which electrons and holes are confined in the direction perpendicular to the interfaces (*z*), while behave as free carriers in the other two directions (*x* and *y*). When the size of the confinement region is comparable to the De Broglie wavelength of the carriers, quantum mechanical effects occur [120], such as a discretization of the energy levels and a change of the DOS respect to that of bulk materials.

$E_g$ values and band alignment are important parameters for the design of a QW structure, since they significantly contribute in determining its electronic and optical properties. Then,

[d] Different methods can be applied to determine the band offsets of a semiconductor heterostructures. As an example, in Ref. [129] a detailed description of band offsets through photoemission measurement is presented.

when the QW is made with alloys, an appropriate choice of the composition allows to tailor energy gaps (see Fig. A.1) and offset values and thus to obtain a QW with desired properties (*band-gap tailoring*) [121]. Moreover, since also the strain has effects on bandstructures and $E_g$ values (see Section 2.1.2), the control of the strain in QW layers contributes to the band gap tailoring.

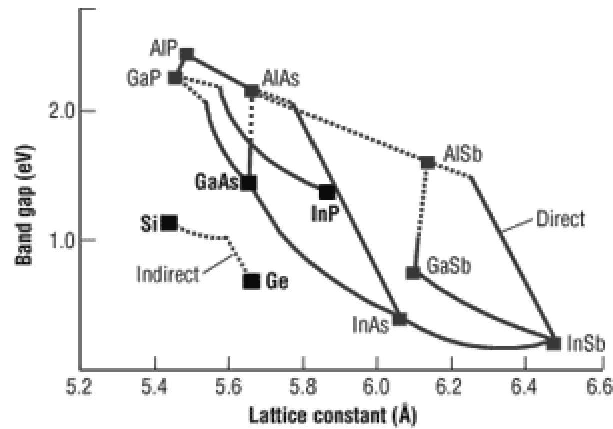


**Figure A.1:** Energy gap as a function of the lattice constant for III-V and group IV semiconductors. Full and dotted lines indicate direct and indirect energy gap semiconductor alloys, respectively.

Two types of band alignment are possible, reported in Fig. A.2.

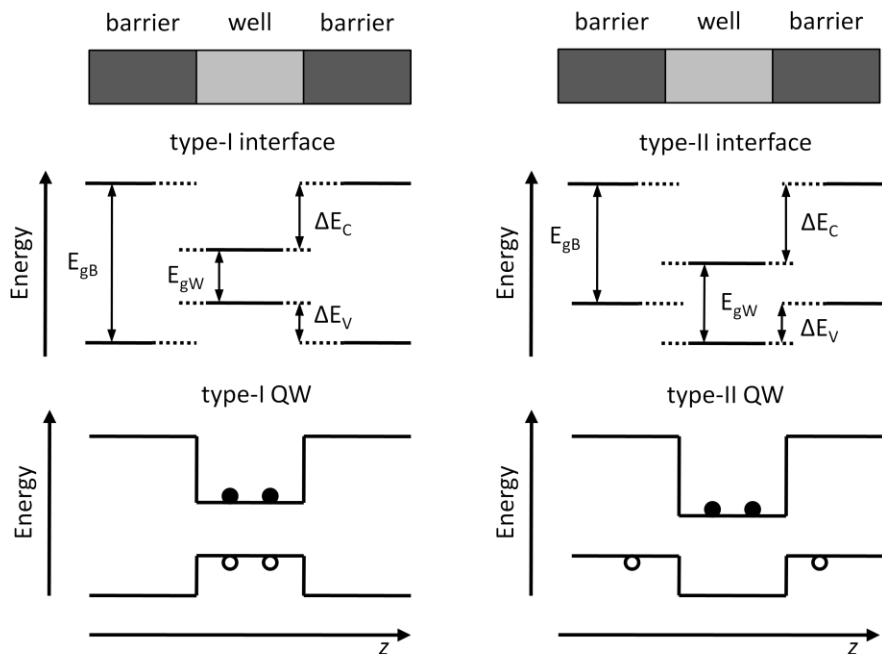


**Figure A.2:** Band aligment for type-I and type-II interfaces and band structure of type-I and type-II QWs. Only in type-I QWs both electrons and holes are confined in the same spatial region.

In the case of type-I band alignment, the bottom of the CB and the top of the VB of the semiconductor that forms the well layer are lower and higher, respectively, than those of the semiconductor that forms the barriers. Of consequence, both kinds of carriers (electrons and holes) are confined in the same spatial region. On the contrary, in type-II QWs the bands are staggered for both the CB and the VB, causing the confinement of electrons and holes in different spatial regions. It is evident that type-I band alignment is strongly preferred for optical applications: the higher overlap between electron and hole wavefunctions provides an increase of the absorption coefficient and of the recombination efficiency.[111]

## A.2 Electronic states in quantum wells

The following description of wavefunctions, energy levels and DOS in QWs is based on the EMA method, which is one of the most widely used tools to calculate the band structure of semiconductor heterostructures[122]. In its simplest form it calculates the valence and conduction eigenvalues by solving the standard 1D time-independent Shrödinger equations considering the energy and the effective mass of carriers at the extremity of each band only[70]. A detailed description of the EMA theory and of the bandstructure calculation of QWs can be found in different texts, such as Refs. [69, 70, 120]. Where not otherwise specified, the following short discussion is based on Ref. [70].

Let us consider for simplicity a type-I QW of III-V direct-gap semiconductors, in which the relevant band edges are all at the Γ point of the Brillouin zone. The QW eigenstates can be written as

$$\Psi_n^{\mathrm{EMA}}(\mathbf{r}) = \sum_{j=1}^{N_B}\left\{\int_{BZ} d\mathbf{k}_\parallel dk_z C_j^{\mathrm{EMA}}(\mathbf{k}_{//}, k_z)\exp\left[i\left(\mathbf{k}_\parallel\cdot\mathbf{r}_\parallel + k_z z\right)\right]\right\} u_{j,\Gamma}(\mathbf{r}) \tag{A.1}$$

where $u_{j,\Gamma}(\mathbf{r})$ are the bulk Bloch functions of the $j^{th}$ band at the Γ point and $\mathbf{k}_\parallel = (k_x, k_y)$ and $\mathbf{r}_\parallel = (r_x, r_y)$ are the wave and the spatial vectors referred to the $xy$ plane. In the EMA, the $C_j^{\mathrm{EMA}}$ coefficients are ≠ 0 only in a small region around Γ. “BZ” indicates that the integral is extended over the whole Brillouin zone. If the contribution of each band can be considered separately (*single-band approximation*), the $j^{th}$ band envelope eigenfunction is given by:

$$f_j(\mathbf{r}) \propto f_j(z)\exp\left[i\mathbf{k}_\parallel\cdot\mathbf{r}_\parallel\right]. \tag{A.2}$$

The exponential term is the plane wave that describes the free motion of carriers in $x$ and $y$ directions. The kinetic energy related to this motion is

$$E_{j,xy} = \frac{\hbar^2 k_\parallel^2}{2m^*} = \frac{\hbar^2\left(k_x^2 + k_y^2\right)}{2m^*}, \tag{A.3}$$

where m* is the effective mass at the band edge we are considering.

The term $f_j(z)$ in Eq. A.2 is the wavefunction for the quantized states in the $z$ direction. If we assume the *Infinitely Deep Well Approximation* (IDWA), i.e. if we consider a QW with infinitely high barriers, $f_j(z)$ is the solution of a Shrödinger equation like

$$-\frac{\hbar^2}{2}\frac{\partial^2 f_j(z)}{\partial z^2} = \mathrm{E}_{j,z} f_j(z). \tag{A.4}$$

The boundary condition is that $f_j(z) = 0$ at the interfaces, due to the fact that the particles can not tunnel out of the well. The solutions to Eq. A.4 are standing waves with nodes at the interfaces. The energy that corresponds to the $n^{\text{th}}$ discrete level is given by

$$\mathrm{E}_{j,z}^{n} = n^2 \frac{\pi^2 \hbar^2}{2\mathrm{m}^* \mathrm{L_z}^2}, \tag{A.5}$$

where $n$ (*subband index*) is the quantum number that marks each confined state of the $j^{\text{th}}$ band and $\mathrm{L_z}$ is the QW thickness.

Equation A.5 describes an infinite ladder of discrete levels whose energy is proportional to the square of the subband index $n$, and inversely proportional to the effective mass and to the square of QW thickness (see Fig. A.3).

It is useful to note that :

- since the confinement energy $\mathrm{E}_{j,z}^{n}$ depends on the effective mass, heavy hole and light hole levels are splitted; in the most of cases the heavy holes have the lowest energy and form the ground state level; [120]
- the wavefunctions can be identified by the number of nodes ($n$-1);
- the states with odd $n$ have even parity and those with even $n$ have odd parity (see Fig. A.3).

The simmetry breaking along the $z$ direction due to the confinement, splits the $j^{\text{th}}$ band into $n$ subbands belonging to different quantized states. Each state in the subband is characterized by four quantum numbers: the band index $j$, the subband index $n$, and the k-values for the motion in the $xy$ plane ($k_x$ and $k_y$). The total energy of the carriers is:

$$\mathrm{E}_j^n = \mathrm{E}_{j,xy} + \mathrm{E}_{j,z}^n = \frac{\hbar^2\left(k_x^2 + k_y^2\right)}{2\mathrm{m}^*} + \frac{n^2\pi^2\hbar^2}{2\mathrm{m}^*\mathrm{L}_z^2} = \frac{\hbar^2}{2\mathrm{m}^*}\left[\left(k_x^2 + k_y^2\right) + \frac{n^2\pi^2}{\mathrm{L}_z^2}\right]. \tag{A.6}$$

The DOS of each subband is a step function of the energy:

$$\mathrm{DOS}_{j,z}^n = \frac{\mathrm{m}^*}{\left(\pi\hbar^2\right)\theta\left(\mathrm{E} - \mathrm{E}_{j,z}^n\right)} . \tag{A.7}$$

As an example, the DOS dependence on energy for the CB is reported in Fig. A.3, together with a schematic picture of the wavefunctions, the energy levels and the dispersion curves for a GaAs QW in the IDWA approximation.

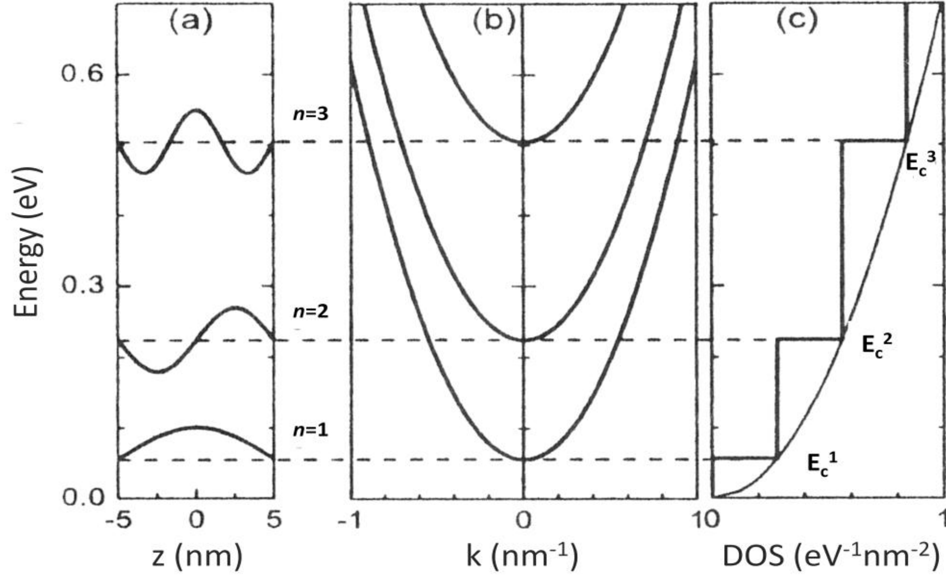


**Figure A.3:** (**a**) Scheme of wavefunctions and energy levels in the CB for a GaAs QW with $L_z$ = 10 nm in the IDWA approximation. (**b**) Dispersion curves: subbands derived from confinement in *z* direction are clearly visible. (**c**) Step-like DOS for a 2D system; the typical trend for the bulk DOS is also reported as a reference.[111]

When we consider the case of a real QW with a finite potential barrier $V_0$ (see Fig. A.4), the penetration of the wavefunction into the barrier regions has also to be considered. The wavefunctions in the barriers assume an exponential form like:

$$f_{j,B}(z) = A e^{\pm \kappa z} \quad , \tag{A.8}$$

where κ satisfies the relationship

$$\frac{\hbar^2 \kappa^2}{2m_B^*} = V_0 - E_{j,z}^n \quad . \tag{A.9}$$

In Eq. A.9 $m_B$* is the effective mass in the barrier.

The results obtained in the IDWA are still valid, but have to be modified as follows:

- the number of confined states is finite, and there is always at least one confined state, no matter how small $V_0$ is;
- the confinement energies $E_{j,z}^n$ are reduced respect to the IDWA case;

- the localized state wavefunctions penetrate into the barrier region: since the decay constant κ (Eqs. A.8 and A.9) is proportional to ($V_0$ - $E^n_{j,z}$), the fraction of the wavefunction that penetrates into the barrier rises as the energy level approaches $V_0$.

The numer of nodes of the wavefunction and the parity of the states are the same as in the IDWA condition.

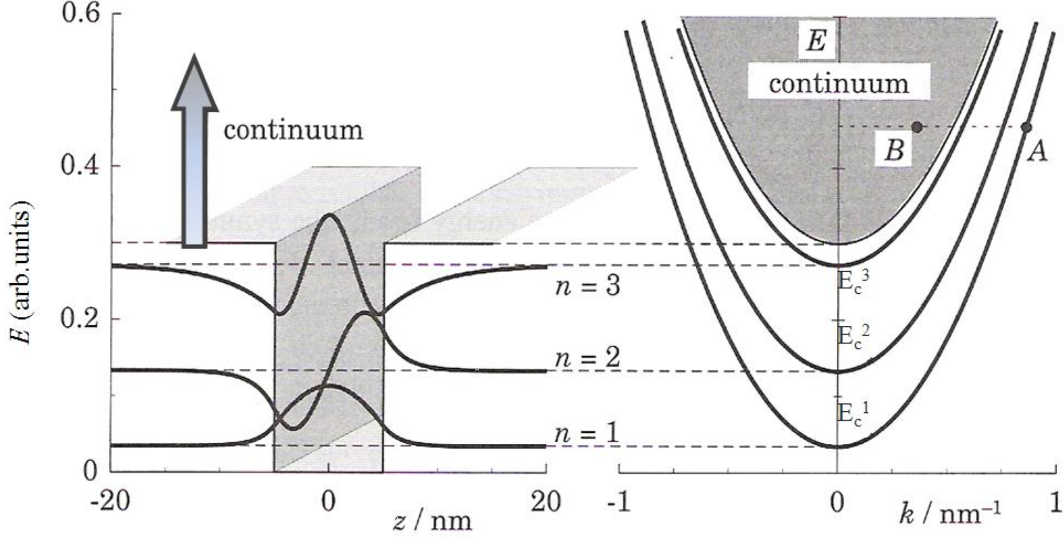


**Figure A.4:** Scheme of levels and wavefunctions (left) and bandstructure (right) of a QW with finite potential barriers. Above the discrete levels, continuum states can be found. The wavefunctions of the confined states penetrate into the barrier. Even if electrons A and B (right) have the same energy, their confinement character is different: the first is confined, with high $k_x$ and $k_y$ values, the second is delocalized in the *z* direction.[70]

For a more accurate description of the electronic states in QWs also the differences in the band structures, and thus in the effective masses, of wells and barriers should be considered. This is done in basic textbooks, such as, e.g., Ref. [70].

Different other methods can be used to calculate the electronic properties of QWs, as tight-binding [76, 123], pseudopotential [124] and density functional [125, 126]. A detailed review on EMA advantages and limits, and a comparison of the different methods can be found in Ref. [122].

## A.3 Optical transitions in quantum wells

This Section is aimed at providing the selection rules for optical transitions in QWs. The probability of a transition between confined states in a QW can be derived using the Fermi golden rule:

$$W_{j,i} = \frac{2\pi}{\hbar}\left(\frac{eE_0}{m_0\omega}\right)^2 \left|\langle j|\mathbf{e}\cdot\mathbf{p}|i\rangle\right|^2 \delta(E_i - E_j - \hbar\omega)\,, \tag{A.10}$$

where **e** and $E_0$ are the electric field polarization and intensity, respectively, **p** is the momentum operator and $\hbar\omega$ is the photon energy. If we consider a transition between a confined valence state ($i$) and a confined conuction state ($j$) in a direct gap type-I QW, in the EMA framework the initial and final states can be written as

$$\psi_i = \mathrm{A}^{-1/2} f_{v,i}(z) \exp\left[i\mathbf{k}_{\|}^{v,i}\mathbf{r}_{\|}\right] u_{v,\Gamma}(\mathbf{r}) \tag{A.11}$$

$$\psi_j = \mathrm{A}^{-1/2} f_{c,j}(z) \exp\left[i\mathbf{k}_{\|}^{c,j}\mathbf{r}_{\|}\right] u_{c,\Gamma}(\mathbf{r}), \tag{A.12}$$

giving a matrix element

$$\left|\langle j|\mathbf{e}\cdot\mathbf{p}|i\rangle\right| = p_{v,c}\, g\, \delta\left(\mathbf{k}_{//}^{v,i} - \mathbf{k}_{//}^{c,j}\right)\int \mathrm{d}z f_{c,j}^{*}(z) f_{v,i}(z). \tag{A.13}$$

In Eq. A.13 $g$ is the spin-orbit factor, which takes into account the selection rules for optical transition between states with different angular momentum, and $p_{v,c} = \langle u_{c,\Gamma}|\mathbf{e}\cdot\mathbf{p}|u_{v,\Gamma}\rangle$ is the optical oscillator strength. The possible transitions between conduction and valence subbands are vertical in the $\mathbf{k}_{\|}$ space. The oscillator strength of such transitions depends on the overlap between electron and hole wavefunctions:

$$\int \mathrm{d}z f_{c,j}^{*}(z) f_{v,i}(z). \tag{A.14}$$

In the case of a type-I QW in the IDWA approximation, this integral is simply given by $\delta_{i,j}$, i.e. only interband transitions between states with the same subband index $n$ are allowed: $\Delta n \equiv i - j = 0$.

Extending these results to the case of a real QW with finite potential barriers, transitions with $\Delta n \neq 0$ are also allowed, but very weak. For symmetric QWs, transition with $\Delta n = \pm\, 2m + 1$, with $m = 0$, 1,2… are strictly forbidden. The selection rules for a real QW with type-I band alignment are schematically reported in Fig. A.5.

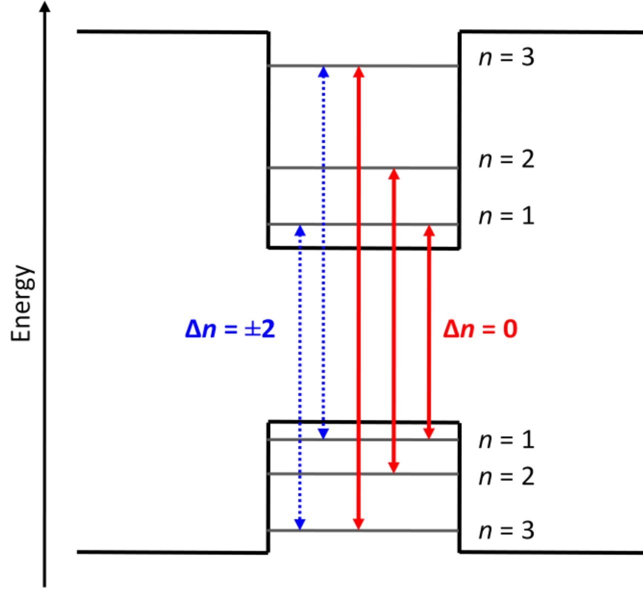


**Figure A.5:** Scheme of interband transitions between confined states of a QW. Continuous red lines indicate strong transitions ($\Delta n$ = 0), while blue dashed lines indicate weak, but allowed transitions ($\Delta n$ = 2).

## A.4 Excitons in 2D systems

Excitons are bound states between an electron and a hole, with the Coulomb interaction being responsible for the binding energy[127]. In bulk semiconductors hydrogenoid discrete energy levels rise below the continuum due to this Coulombian attraction. The exciton binding energy ($R^*$) and Bohr radius ($a^*$) are given by

$$R^* = \frac{2m_{re}^* e^4}{\hbar^2 (8\pi\varepsilon)^2} = \frac{m_{re}^*}{m_0}\frac{\varepsilon_0^2}{\varepsilon_0} R_H \qquad \text{(A.15)}$$

and

$$a^* = \frac{4\pi\varepsilon\hbar^2}{m_{re}^* e^2} = \frac{m_0}{m_{re}^*}\frac{\varepsilon_0}{\varepsilon} a_H , \qquad \text{(A.16)}$$

where $m_{re}^* = (1/m^*_e + 1/m^*_h)^{-1}$ is the reduced mass of the electron-hole pair, $\varepsilon$ is the permettivity of the semiconductor, $R_H$ is the Rydberg of the hydrogen atom (= 13.6 eV) and $a_H$ is the Bohr radius of the hydrogen atom.[111] In bulk semiconductors $a^*$ is of the order of 10 nm, while $R^*$ is of the order of some meV depending on the semiconductor.

Since in QWs the dimension of the well layer is close to the typical exciton Bohr radius, the exciton wavefunction and energy can be significantly modified. For $L_z << a^*$ the exciton can be considered two-dimensional: in the IDWA, the exciton binding energy is about 4 times

larger than in bulk semiconductors ($R_{QW}^* = 4R^*$) and its Bohr radius is reduced by a factor of 2 ($a_{QW}^* = a^*/2$). One of the consequences of this increase of the binding energy in QWs is that the excitons are very stable, and dominate PL and ABS spectra even at RT [111, 120] (see, e.g., Fig. A.6).

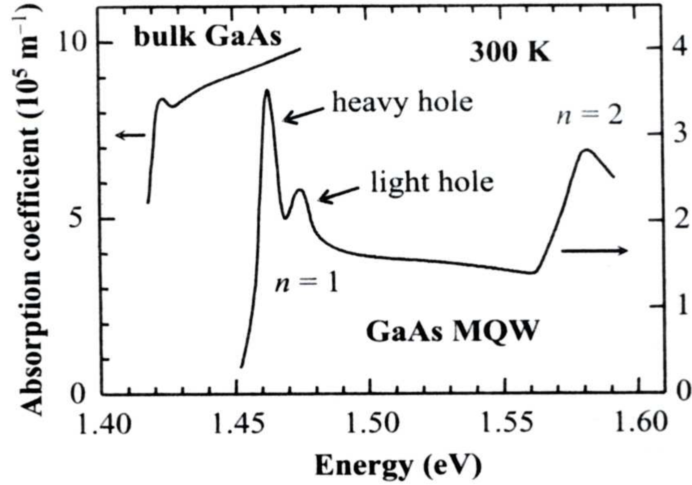


**Figure A.6:** RT ABS spectrum of GaAs/$Al_{0.28}Ga_{0.72}As$ QWs: strong excitonic peaks for both the HH1-cΓ1 and the LH1-cΓ1 transitions are visible. The RT ABS spectrum of bulk GaAs is also reported: the exciton manifests itself as a weak shoulder at the band edge. [128]

Of consequence, in a QW system $R_{QW}^*$ and $a_{QW}^*$ depend on $L_z$: as an example for real QWs with finite potential barriers, in Fig. A.7 their values are reported as a function of $L_z$ for $Al_{0.4}Ga_{0.6}As$/GaAs QWs[104]. When $L_z$ decreases, $R_{QW}^*$ increases and $a_{QW}^*$ decreases due to the smaller electron-hole separation. For narrow QWs a non negligible fraction of the wavefunctions penetrate the barriers: as a consequence, $R_{QW}^*$ and $a_{QW}^*$ tend to bulk values.

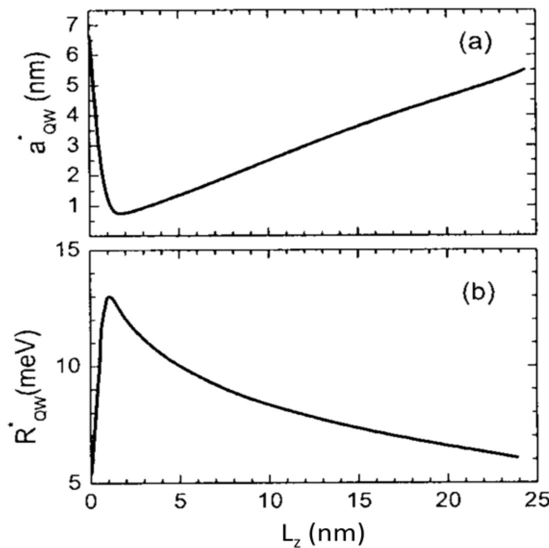


**Figure A.7:** Dependence of exciton Bohr radius $a_{QW}^*$ **(a)** and binding energy $R_{QW}^*$ **(b)** on the QW thickness $L_z$.[104]

# Appendix B

# Samples and experimental

## B.1 Ge/SiGe quantum wells grown via LEPECVD

This section is devoted to the description of the samples analyzed in this work. First, the main features of the growth technique are summarized. Then, the characteristics of the samples are described and their structural quality is discussed also using the results of optical characterization.

### B.1.1 LEPECVD

The samples analyzed in this work have all been grown by LEPECVD. The key features of this "state-of-the-art" technique are a wide range of growth rates (from 0.1 nm/s to 10 nm/s), the independence of the deposition kinetics on the substrate temperature and the close correspondence between the mixture of precursor gases and the composition of the grown layers[130]. LEPECVD has been employed for the growth of both SiGe relaxed layers and SiGe heterostructures, as reported for example in Refs. [38, 131 - 133]. A schematic diagram of the LEPECVD system is shown in Fig. B.1. The core of this growth system is a CVD reactor in which the cracking of the precursor gases is caused by a plasma flow instead of being due to the high temperature of the substrate. The high intensity of the plasma provides fast deposition rates, while its low energy prevents any damage of the substrate due to collisions with ions.

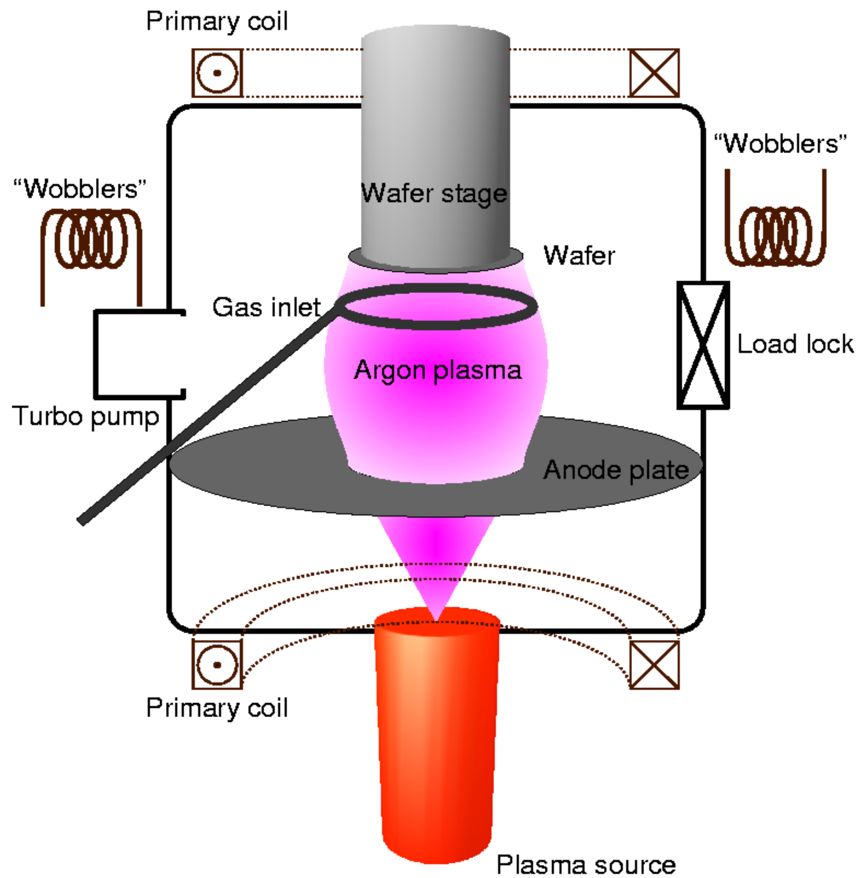


**Figure B.1:** Schematic diagram of the LEPECVD growth system. [130]

The plasma is generated by a DC arc discharge in an Ar atmosphere between a heated filament (cathode) and the grounded walls of the chamber (anode). External copper coils, that produce a magnetic field, allow to stabilize the plasma flux, to make it homogeneous and to focalize or deviate it. In this way it is possible to calibrate the intensity of the plasma on the substrate, in order to obtain the desired growth rate. During the deposition process, the working pressure is $10^{-2}$ mbar. The substrate, whose diameter in the case of our samples is 4 inch, is kept at temperatures between 450°C and 700°C, depending on the composition of the alloy to be deposited. The cracking of the precursor gases by plasma provides a better control of thickness and composition of the grown layers than the thermal activation due to the substrate heating. For SiGe alloys deposition silane ($SiH_4$) and germane ($GeH_4$) are used, diluted in $H_2$. In case of n or p doping, $PH_3$ and $B_2H_6$ are respectively employed. Details on the growth process and on the development of LEPECVD technique can be found in Ref. [130].

## B.1.2. Sample structure

All the samples studied in this thesis are characterized by the same general structure, schematically sketched in Fig. B.2. On a 4-inch Si wafer (100) a *graded virtual substrate* (GVS) is grown, whose composition varies from Si to $Si_{0.10}Ge_{0.90}$ with a rate of about 7 % $\mu m^{-1}$. The GVS is capped with a 2 µm thick relaxed $Si_{0.10}Ge_{0.90}$ layer. The total thickness of this buffer layer is about 15 µm. The active part of the structure is then deposited, alternating $Si_{0.15}Ge_{0.85}$ barriers and Ge wells. At the end a 40 nm $Si_{0.10}Ge_{0.90}$ layer and a ~ 10 nm Si cap are grown in order to guarantee that the same strain conditions are experimented at both the edges of the active part of the heterostructure. For each sample a reference substrate is grown for ABS measurement (see Section B.2): its structure reproduces that of the sample but without well and barrier layers, as shown in Fig. B.2.

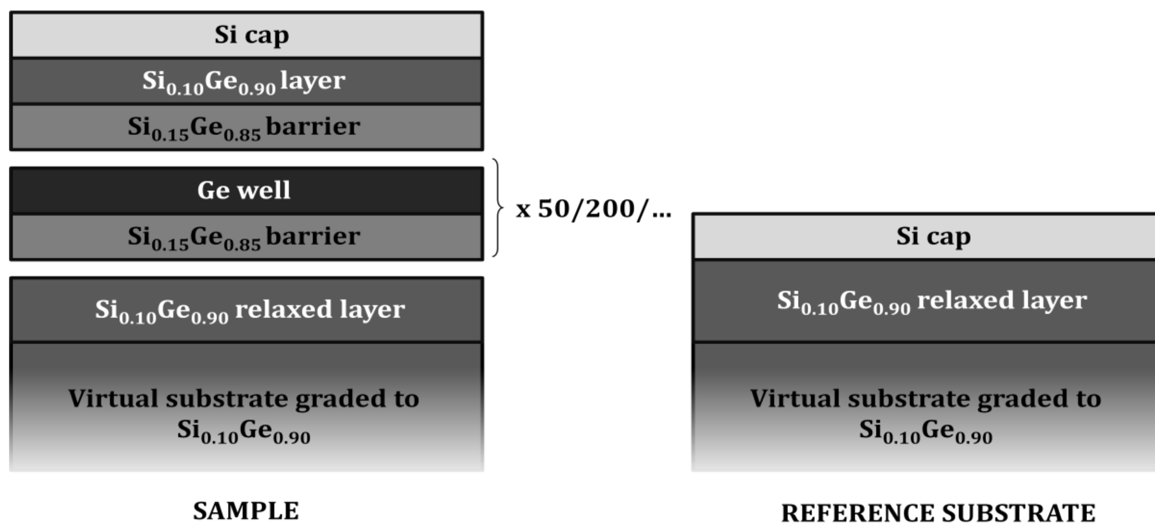


**Figure B.2:** Sketch of the structure of the analyzed samples (left) and of the reference substrates (right). The samples generally differ just for the number of periods and for the thickness of well and barrier layers.

The characteristics of the different wafers are reported in Table B.1. They present the same nominal thickness of the layers and barrier composition values, and differ just for the number of periods and for the deposition rates. The number of periods ranges from 50 to 1000, while two different deposition rates were used: 0.3 nm/s (*Low Rate*) and 4 - 6 nm/s (*High rate*).

| Wafer | Periods | Well | | Barrier | | Growth rate | Substrate |
|---|---|---|---|---|---|---|---|
| | | % Ge | Nominal thickness | % Ge | Nominal thickness | | |
| 7864 | 200 | 100% | 10 nm | 85% | 21nm | 0.3 nm/s | 7865 |
| 7909 | 200 | 100% | 10 nm | 85% | 21nm | 4-6 nm/s | 7908 |
| 8009 | 50 | 100% | 10 nm | 85% | 21nm | 4-6 nm/s | 7908 |
| 7873 | 1000 | 100% | 10 nm | 85% | 21nm | 4-6 nm/s | 7908 |
| 8013 | 50 | 100% | 10 nm | 85% | 21nm | 4-6 nm/s | 7908 |
| 8125 | 50 | 100% | 10 nm | 85% | 21nm | 0.3 nm/s | 8132 |

**Table B.1:** Analyzed wafers grown by LEPECVD. For each wafer the number of periods, the growth rate, the composition, and the nominal thickness of well and barrier layers are reported. For each wafer the reference substrate is also indicated.

Despite the high number of periods, the analyzed samples present a good structural quality, as discussed in Ref. [68]. This is made possible mainly by two factors: the introduction of the GVS and the strain balancement in the active part of the structure.

The GVS reduces the effect of the lattice mismatch between the Si substrate and the Ge-rich layers, yielding a TDD of about $4\text{-}5\cdot10^{6}$ $cm^{-2}$ in the relaxed $Si_{0.10}Ge_{0.90}$ layer.[134] This value, which can be reasonably assumed to characterize also the active part of the structure, is two orders of magnitude lower than typical TDD density of Ge-rich layers directly grown on Si[135] (see Fig. B.3).

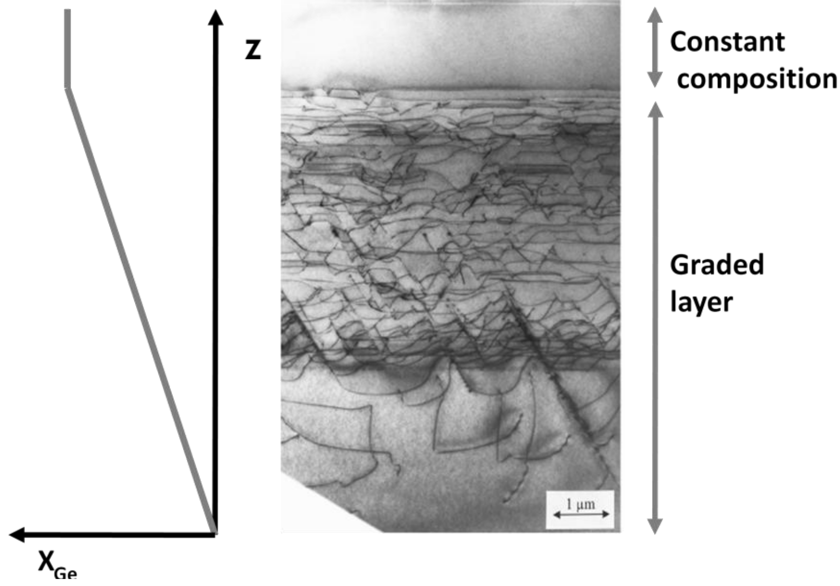


**Figure B.3:** TEM image of a typical graded virtual substrate grown via LEPECVD [132]. The final relaxed layer with constant composition is also shown. The graded virtual substrate allows to reduce the lattice mismatch and to lower the TDD concentration in the active layers of two orders of magnitude respect to Ge layers directly grown on Si.

The strain compensation allows to keep the mean strain in the active layer equal to 0, preventing the strain to relax through formation of dislocations. As a matter of fact, in order to adapt their lattice constant to that of the relaxed $Si_{0.10}Ge_{0.90}$ layer (*pseudomorphic* growth), wells and barriers experiment compressive and tensile strain respectively. The growth of a large number of layers without strain relaxation through dislocations requires the balance between the compressive strain in the wells and the tensile strain in the barriers. This is reached if the compositions and the thicknesses of well and barrier layers satisfy the following condition

$$\frac{\mathrm{d_W} a_\mathrm{W} + \mathrm{d_B} a_\mathrm{B}}{\mathrm{d_W} + \mathrm{d_B}} = a_\mathrm{S}, \tag{B.1}$$

where d is the layer thickness, $a$ is the lattice constant, and W, B and S refer respectively to well, barrier and substrate. In other words the mean lattice constant of well and barrier layers has to be equal to that of the relaxed layer at the top of the GVS (see Fig B.4).
High resolution XRD measurement have confirmed the pseudomorphic growth of the active part of the structure on top of the $Si_{0.10}Ge_{0.90}$ constant composition layer and then the effectiveness of strain balancement in the heterostructure.[68] Moreover, thanks to the strain

balancement no new dislocatios are generated in the active part of the structure due to strain relaxation.

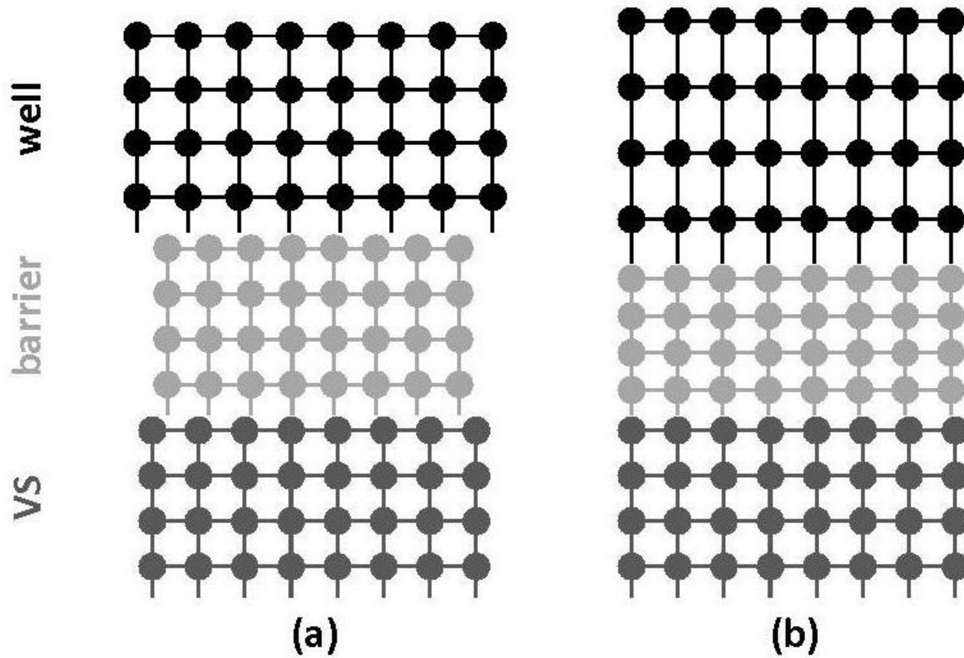


**Figure B.4:** **(a)** SiGe lattice constant depends on alloy composition. **(b)** Strain balanced heterostructure: the tensile strain in $Si_{0.15}Ge_{0.85}$ barriers is compensated by the compressive strain in Ge wells. The active part of the structure grows pseudomorphically on the relaxed $Si_{0.10}Ge_{0.90}$ VS.

The samples studied in this work were grown on substrates with a 4-inch diameter. The actual thickness of the deposited layers is highly non uniform across the wafer, due to inhomogeneity in the intensity of the plasma. For example, in Fig. B.5(a) the thickness of one period (well + barrier) measured via XRD at different distances from the center of the wafer along the direction perpendicular to the main flat (grey area of Fig. B.5(b)) is reported for wafer 7873. Even if this inhomogeneity is a limit of the LEPECVD, it is an advantage for the optical analysis, since it provides samples with identical structure and composition, but with different well thickness.

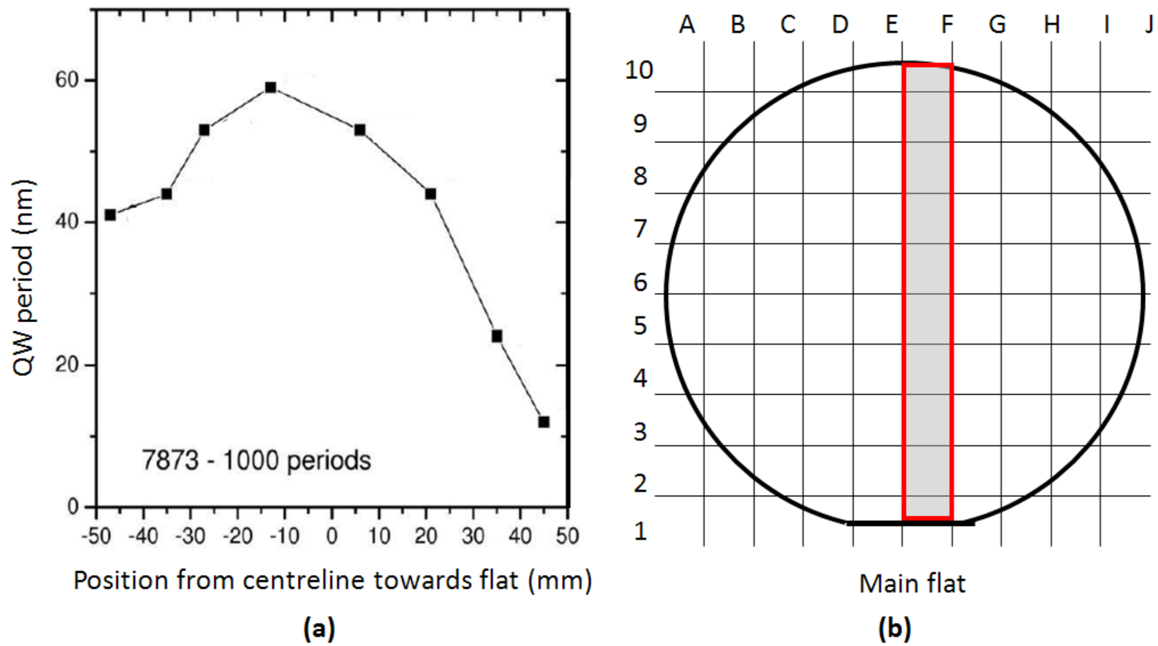


**Figure B.5: (a)** Thickness of a period (well + barrier) measured via XRD for wafer 7873 as a function of the position along the direction perpendicular to the main flat. The measurements have been performed at the L-NESS laboratories in Como. **(b)** Typical plan of a wafer that allows to identify the position of a sample across the wafer.

As a consequence, each analyzed sample is identified with two numbers: the first refers to the wafer, and the second indicates the position of the sample across the wafer.

HR XRD measurement have been performed to obtain the real thickness and composition values of well and barrier layers for some of the analyzed samples. The results for samples belonging to wafer 7864 are reported in Table B.2[15].

| Sample | Well Ge content | Well thickness | Barrier Ge content | Barrier thickness | VGS final Ge content |
|---|---|---|---|---|---|
| 7864-E1 | 1.00 | 3.8 nm | 0.825 | 7.7 nm | 0.90 |
| 7864-E3 | 1.00 | 6.1 nm | 0.825 | 12.3 nm | 0.90 |
| 7864-E5 | 1.00 | 8.5 nm | 0.825 | 17.0 nm | 0.90 |
| 7864-E10 | 1.00 | 9.9 nm | 0.82 | 22.8 nm | 0.89 |

**Table B.2:** Actual well and barrier thickness and compositions measured via HR-XRD for samples belonging to wafer 7864. The composition of the relaxed final layer of the GVS is also reported. The first number of the sample names defines the growth, the second the position of the sample along the wafer. The measurements have been performed at the Institute of Microtechnology of the University of Neuchâtel.[15]

As previously discussed (see, e.g., Section A.2), the energy of the transitions between confined states depends on $L_z$. For example, the dependence of the cL1-HH1 zero-phonon PL peak on $L_z$ in our Ge/SiGe MQWs is reported in Fig. 2.17. This allows to estimate from optical measurements the actual value of $L_z$ even for samples that have not been measured through HR XRD.
A detailed discussion about sample structure, VGS growth protocol and XRD analysis of these samples is reported in Ref. [68].

## B.2 Continuous wave photoluminescence and linear absorption measurements

In this Section the experimental setup used for CW-PL measurements, schematically represented in Fig. B.6, is briefly described. The samples are excited

- by the 1064 nm (1.165 eV) line of a Nd:YVO laser, with maximum exciting power density of about 5 kW/cm$^2$, a spot diameter of about 100 µm and penetration depth of about 50 QWs (*resonant* excitation, see Section 4.3);
- by the 532 nm (2.35 eV) line of a Nd:YVO laser, with maximum exciting power density of about 2 kW/cm$^2$, a spot diameter of about 100 µm and penetration depth of 2-3 QWs (*non resonant* excitation, see Section 4.3).

The laser beam is focused on the sample by an achromatic doublet at an incidence angle of about 60°. The emitted light is collected and collimated by a parabolic mirror (M1), and reaches the Fourier transform spectrometer (Jasco FT-IR 800) thanks to two plain mirrors (M2 and M3). The optical system of the FT spectrometer is sketched in Fig. B.6. Two detectors are available: an InGaAs photodetector for measurements in the spectral range between 0.73 and 1.38 eV (D3), and a Peltier cooled PbS photoresistance (D2), that allows to extend the spectral range to low energies down to 0.4 eV. Measurements at lattice temperatures between 5 K and 300 K can be performed mounting the sample in a Oxford Optistat AC-V12 cold finger closed circle cryostat. Alternatively, for measurements at the lattice temperature of 2 K, the sample is bathed in superfluid He using an Oxford Bath Cryostat MD3.
Unless otherwise specified, the spectral resolution of this system is 16 cm$^{-1}$, corresponding to 2 meV.
In Ref. [136] a detailed discussion of the advantages and limits of Fourier transform spectrometers applied to CW-PL measurements in the IR spectral region is provided.

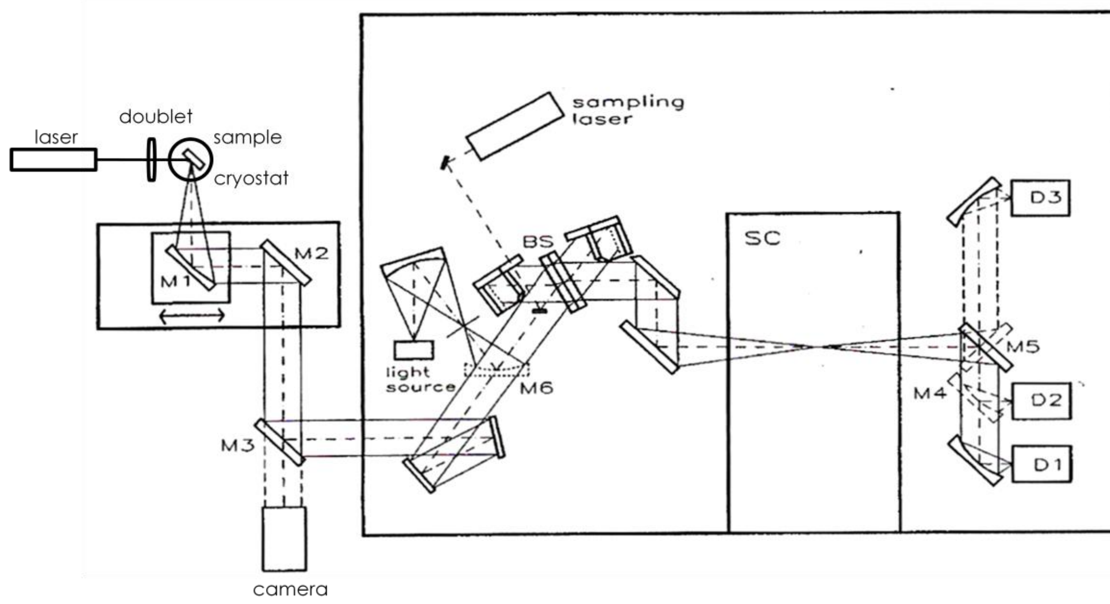


**Figure B.6:** Experimental setup used for CW-PL measurements. The optical scheme of the FT-IR spectrometer is also reported.

For linear ABS measurements the same experimental setup is used. An halogen lamp is employed for the excitation; the light is focused on the mirror-polished back surface of the sample by two parabolic mirrors. In ABS measurement a sample area of about 1 $mm^2$ is probed. The measured OD is defined as

$$OD(\lambda) = -\log \frac{I_{TS}(\lambda)}{I_{TR}(\lambda)}, \quad (B.2)$$

where $I_{TS}(\lambda)$ is the transmission spectrum of the sample and $I_{TR}(\lambda)$ is that of the reference substrate (see Section B.1.2).

## B.3 Decay time measurements

In this Section, the experimental setups used for TR-PL measurement of the indirect and direct gap related emission are described. Since the two transitions are expected to be characterized by different decay times, two systems with different time resolution were used. Moreover, in Section B.3.2 the procedure to extract decay time values from the experimental data in the case of the indirect-gap related recombination is described; the effects that may affect the shape of the decay curve are also presented, together with the solutions adopted for their elimination.

## B.3.1 Measurement of the indirect gap related decay time

In Fig. B.7 the experimental setup employed for the decay time measurement of the indirect gap related emission is sketched. The excitation source is the 351 nm (3.51 eV) line of a Q-switched triplicated Nd:YLF pulsed laser (3 kHz repetition rate, 121 W/cm$^2$ average power density, and 5.5·10$^3$ kW/cm$^2$ peak power density). As discussed in Sections 3.2 and 4.3, this excitation energy promotes carriers to the continuum states of wells and barriers (*non-resonant* excitation conditions). A penetration depth of 2-3 QWs is estimated. The incidence angle of the laser beam on the sample is about 70°. The emission is collected by a single grating monochromator with a bandwidth of 3.2 nm, detected by a Hamamatsu R5509-73 photomultiplier tube and finally recorded by a FAST ComTec P7888-1(E) multi-stop acquisition board, working in single photon counting mode. A trigger signal coming from the laser provides the start to the acquisition. The sample is mounted in a close cycle cold finger cryostat Leybold R210 and the PL can be measured at lattice temperatures ranging between 14 and 300 K.

This system allows to measure the decay curve at a selected emitted wavelength (see, e.g., Fig. 3.5); the shortest measurable decay time is 2 ns and the precision of the measured decay time is ± 0.3 ns.

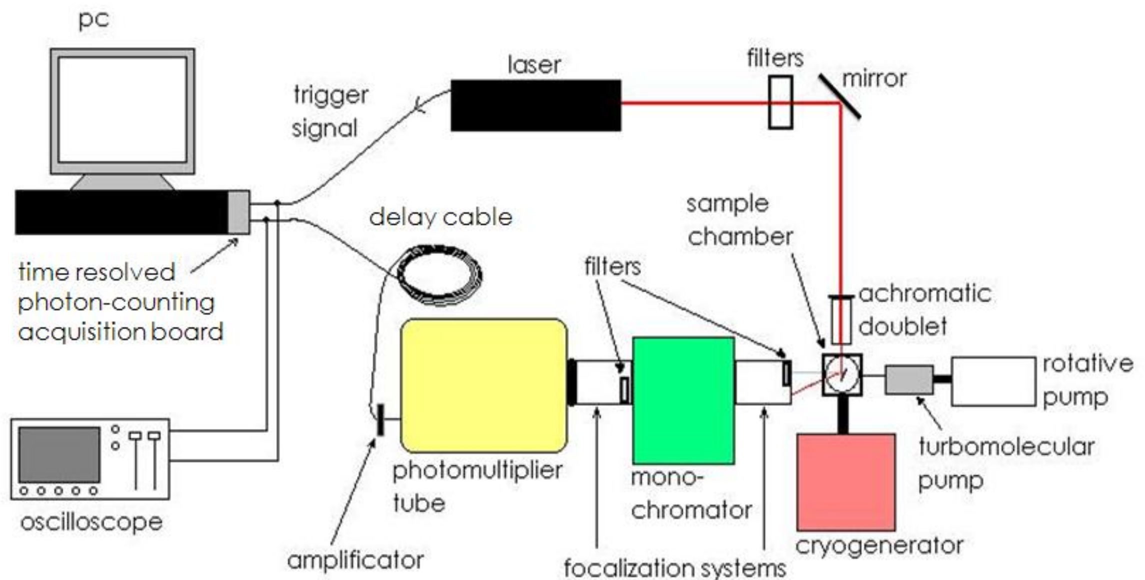


**Figure B.7:** Schematic sketch of the experimental setup for the decay time measurements of the indirect gap related emission.

## B.3.2 Extraction of the PL decay time from the experimental measurements

This Section is devoted to a detailed description of the extraction of PL decay times from the experimental measurements. First the procedure adopted to estimate the decay time values from the experimental decay curves is described. Then the methods employed to prevent instrumental artifacts and to obtain reliable decay curves are discussed.

A measured PL decay curve is actually a convolution of three components: the laser pulse, the acquisition system response and the sample PL decay. A measurement of the diffused laser light gives a curve which includes the first two components. This curve, which is well fitted by a Gaussian, can be written as

$$f(t) = \frac{A}{w\sqrt{\frac{\pi}{2}}}\exp\left[-2\left(\frac{t}{w}\right)^2\right]. \tag{B.3}$$

The PL decay is characterized by an exponential shape, and it is consequently given by

$$g(t) = \exp\left[-\frac{t}{\tau}\right]. \tag{B.4}$$

If we convolve $f(t)$ and $g(t)$, we obtain

$$c(z) = \frac{A}{2}\exp\left(\frac{w^2 - 8\tau z}{8\tau^2}\right)\left\{1 - Erf\left[\frac{w^2 - 4\tau z}{2\sqrt{2}\tau w}\right]\right\}. \tag{B.5}$$

The function $c(z)$ well describes the shape of our experimental decay curves. The two main effects of the convolution are listed in the following.

- The maximum of $c(z)$ is shifted respect to the maximum of the Gaussian $f$(t). A shift of about 2 ns has been indeed experimentally observed, as shown by the comparison between the laser pulse and a typical decay curve reported in Fig. B.8.
- The decay curve is dominated by the Gaussian character within about 7 ns from the maximum and then by the exponential character.

As a consequence, a reasonable estimation of the decay time can be simply obtained through a fit of the decay curves in the region dominated by the exponential component.

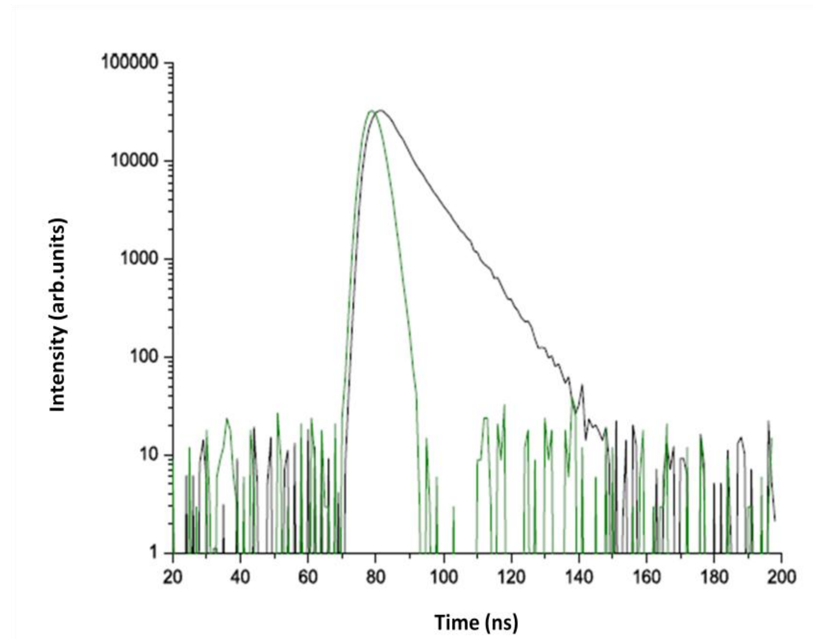


**Figure B.8:** Comparison between the laser decay (green line) and the decay of the PL of sample 7864-E6 at the energy of the cL1-HH1 zero-phonon emission at 14 K (black line).

Our experimental method has also been refined taking into account different effects that can affect the experimental decay curves; the main examples are listed in the following.

- The response time of the electronics of the detection system would cut the initial part of the decay curves (about 10 ns). Consequently, a delay cable has been inserted between the amplifier and the acquisition board (see Fig. B.7) in order to shift the signal of about 70 ns, allowing to detect the whole decay curve.
- If the intesity of the detected PL is too high, the superposition of the electric pulses corresponding to different photon events causes a loss of counts in the decay curve shape. This effect is shown in Fig. B.9 where decay curves obtained for different excitation power densities are reported. When a critical value of emitted photons per bin per pulse is exceeded, artifacts appear on the decay curve (see orange and black lines). A critical value of about $9{\cdot}10^{-3}$ photons per bin per pulse has been measured. Thus, a control of the number of photons per bin per pulse through a proper choise of exciting power densities allows to avoid this effect. On the other hand, this solution can lower the S/N ratio: longer acquisition times are consequently required.

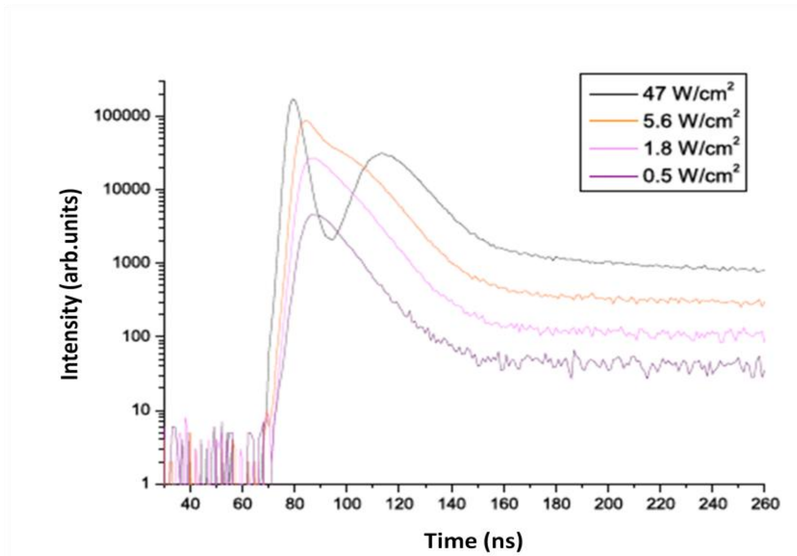


**Figure B.9:** Decay curves obtained exciting sample 7864-E6 with different average power densities. The artifacts due to the overlap between signals corresponing to different photons are visible for higher excitation power densities.

- The indirect gap related emission could be detected also in resonant excitation conditions (Section 4.3). Nevertheless, in these excitation conditions the decay curve present a strong slow component related to defects of the substrate (see Fig. B.10): this component is particularly intense in samples with 50 QWs, as expected since the penetration depth of the 1064 nm line is about 50 QWs (Section B.2). Spectra obtained in non resonant excitation conditions, where the laser penetration depth is of 2-3 QWs only, do not present this component, as shown by the orange line in Fig. B.10.

  Even if a proper subtraction of this slow component related to defects allows to obtain the same decay time values measured under non resonant excitation conditions, in the discussion of Chapter 3 spectra obtained under non resonant conditions only are shown and discussed for consistence and reliability of the data.

In the end, each single QW is actually excited by a different power density. Measurements of decay time as a function of the exciting power density have shown that the decay time is not affected by changes in the exciting power density over an order of magnitude. Consequently, the variation of effective exciting power density for QWs at different depth in the sample does not induce any variation of decay time.

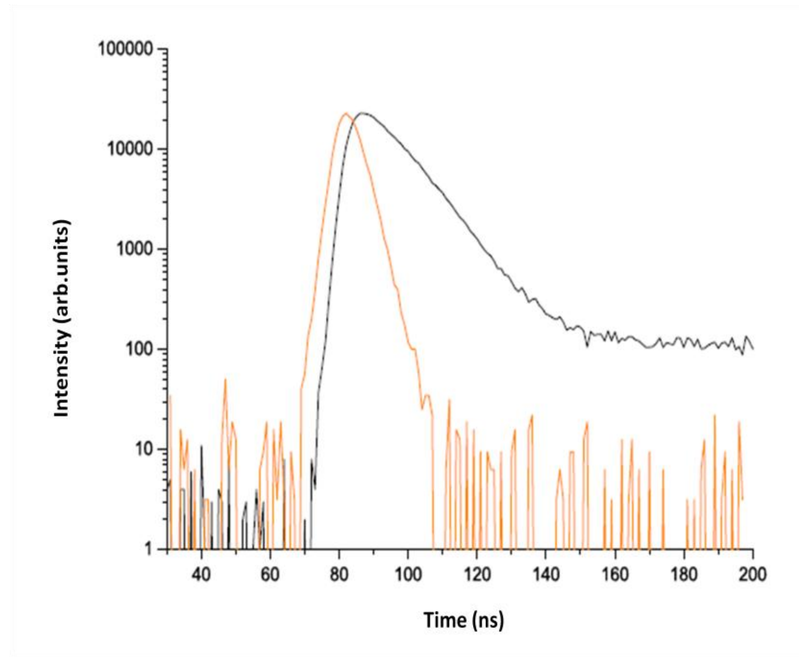


**Figure B.10:** Comparison between decay curves obtained exciting sample 7864-E6 resonantly (black line) and non resonantly (orange line) at 14 K.

## B.3.3 Measurement of the direct gap related decay time

The experimental setup used for time resolved measurement of the direct gap related emission is shematically represented in Fig. B.11. These TR-PL measurements have been performed at the Physics Department of the Philipps-Universität Marburg, in Marburg (Germany).

The excitation source is an ultrafast solid-state tunable Ti:sapphire 100 fs pulsed laser, with a repetition frequency of 80 MHz; the peak power density is 106 kW/cm$^2$ and the average power density 3.5 kW/cm$^2$. *Resonant* excitation conditions (electrons pumped directly to confined Γ-type states) are needed to observe direct gap related emission at LT (see Section 4.3). As a consequence, excitation wavelengths ranging between 980 and 900 nm are chosen. The pump is focused on the sample which is mounted in a liquid He flow cryostat. All measurements are performed at the lattice temperature of 7 K. The PL is focused onto the entrance slit of a grating spectrometer where the light is spectrally dispersed and then imaged on the entrance slit of the optical system of the streak camera (see Fig. B.12). This experimental setup yields a temporal resolution of 1.5 ps.

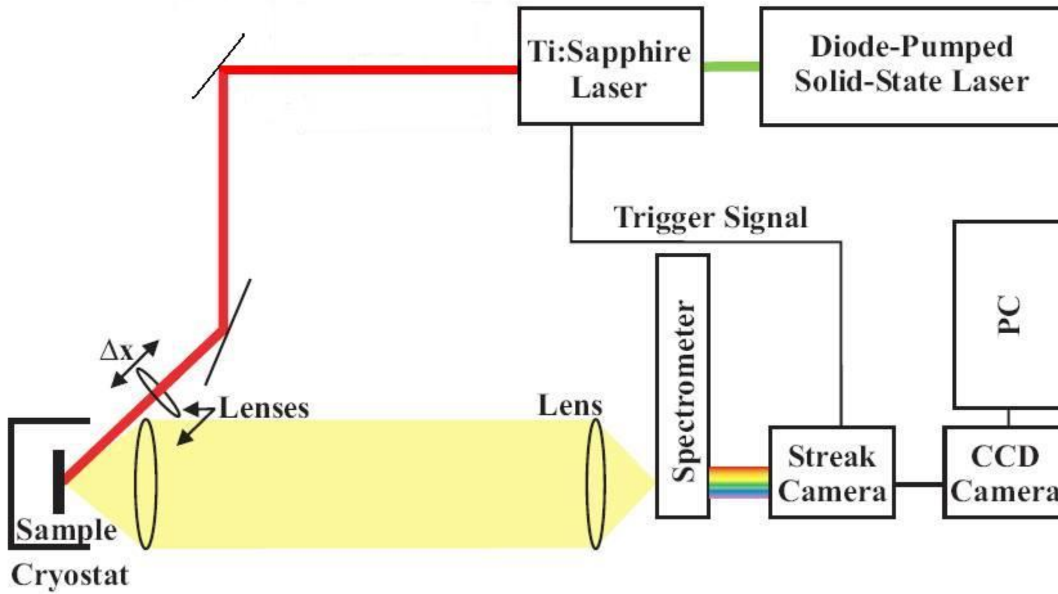


**Figure B.11:** Schematic sketch of the experimental setup for TR-PL measurements using a streak camera.This setup was used to measure the decay of the direct gap related emission.

The principle of operation of a streak camera is schematically shown in Fig. B.12. The photocathode (cutoff energy at about 0.9 eV) converts photons into electrons (photoelectric effect). The electrons are accelerated and pass trough a plate capacitor where they are deflected by applying a sinusoidal voltage, which is frequency-locked to the trigger signal generated by the titanium-sapphire laser. The electrons are then vertically deflected according to the corresponding relative phase. Next, the electrons go through a multi-channel plate where the signal is amplified. A phosphorus screen is used to convert the electrons into photons which are then detected using a standard thermo-electrically cooled CCD camera.

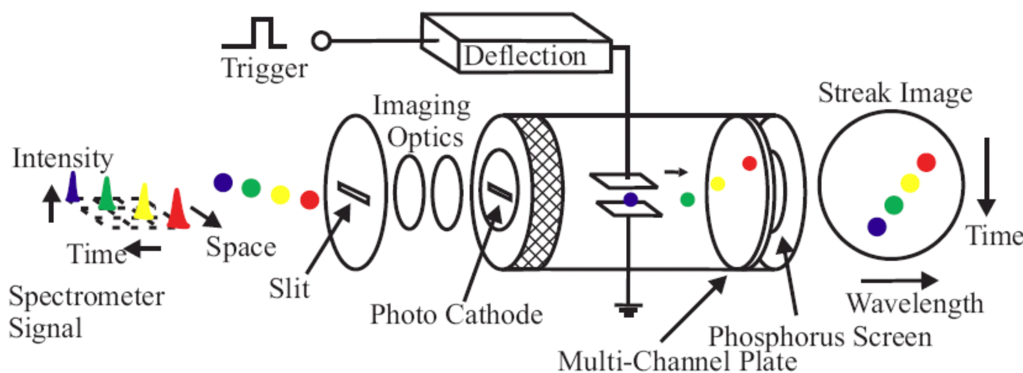


**Figure B.12:** Scheme of the setup and the principle of operation of a streak camera.

A TR-PL measurement performed with this systems yields 3D spectra: *x*-scale is the wavelength, *y*-axis is the time and a false colour scale indicates the intensity of the emitted light at a given time and wavelength. The decay curve shown in Fig. 4.16 is the time trace at the maximum of the direct emission.

## B.4 Photoluminescence as a function of excitation wavelength

For the CW-PL measurements as a function of the excitation wavelength, which have been performed at the Physics Department of the Philipps-Universität Marburg, in Marburg (Germany), the system sketched in Fig. B.13 has been employed. The samples are excited by a tunable Ti:sapphire laser, with $\lambda_{exc}$ ranging from 840 to 1010 nm, corresponding to photon energies between 1.48 and 1.23 eV (resonant excitation). Different excitation power densities from 1 to 11 kW/cm$^2$ are applied. The exciting laser is focused on the sample which is mounted in a liquid He flow cryostat. All measurements are performed at the lattice temperature of 10 K. An Optical Spectrum Analyzer (OSA) with a cut-off energy of about 0.7 eV and spectral resolution of about 1 nm is used for the analysis of both Γ- and L-related transitions.

Additionally, linear ABS measurements can be performed using the same detection system. The light emitted by a tungsten halogen lamp is used: the beam is focused on the mirror-polished back surface of the sample. A suitable system setting allows to observe the same point of the sample in both PL and ABS measurements.

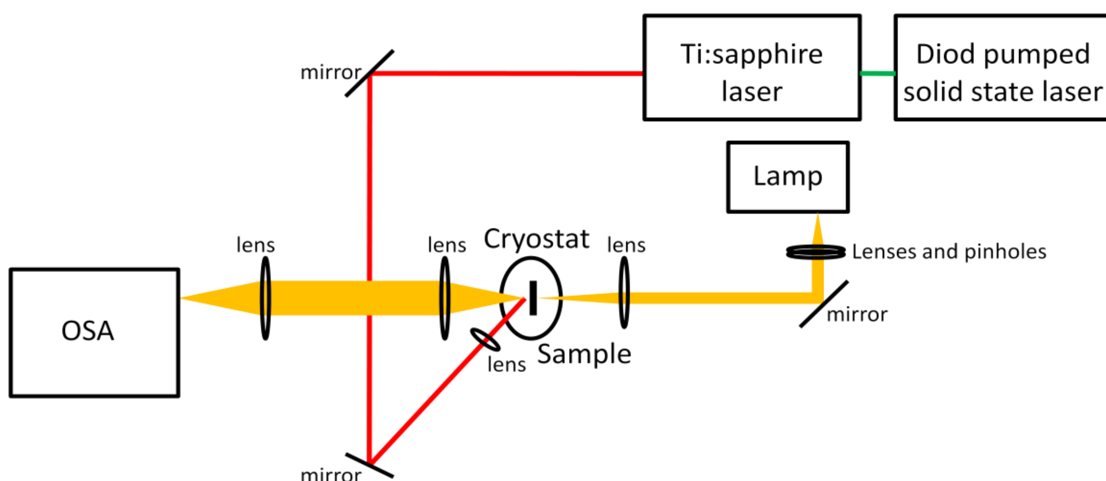


**Figure B.13:** Experimental set up for CW-PL measurements as a function of the excitation wavelength. The system allows also to perform ABS measurements on the same point of the sample under analysis.

In order to more accurately detect peak shifts and intensity variations of the direct gap PL we have exploited the higher sensitivity of the experimental system used for the TR-PL measurements (see Section B.3.3). In this case, the acquisition is performed in *Focus mode*, i.e. integrating the spectra in time: no voltage is applied at the plate capacitor of the streak camera and the electrons pass without deflection.

## B.5 Time resolved pump-probe absorption measurements

Figure B.14 schematically shows the experimental setup used in TR pump-probe ABS measurements in the ultrafast regime, which have been performed at the Physics Department of the Philipps-Universität Marburg, in Marburg (Germany). A tunable Optical-Parametric Amplifier (OPA) is used as pump source, emitting 80 fs pulses and allowing for a continuous tuning of the excitation energy in the visible and the near infrared spectral range. The samples are probed by a white-light supercontinuum generated by self-phase modulation in a sapphire crystal. Both the generation of the pump and probe pulses are driven by a 1 kHz regenerative Ti:sapphire amplifier system with 120 fs pulse length at 800 nm and a pulse energy of 1 mJ. The system yields a time resolution better than 50 fs. The sample is mounted under Brewster angle to minimise reflection losses and placed in a liquid He flow cryostat that allows to perform measurements at the lattice temperature of 10 K. The probe light transmitted by the sample is spectrally resolved by a grating spectrometer, and then detected using an InGaAs photodiode array. Further details concerning the pump-probe setup and the white-light chirp corrections can be found in Refs. [35] and [137].

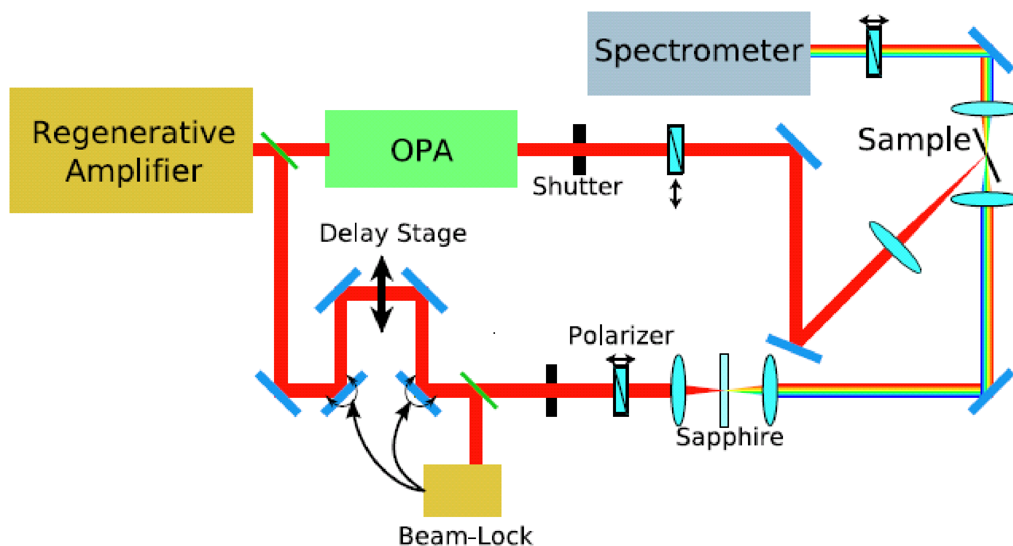


**Figure B.14:** Schematic sketch of the experimental setup used for TR pump-probe ABS measurements in the fs regime.

# List of publications

## Papers

[1] A. Giorgioni, **E. Gatti**, E. Grilli, A. Chernikov, S. Chatterjee, D. Chrastina, G. Isella, and M. Guzzi, “Photoluminescence decay of direct and indirect transitions in Ge/SiGe multiple quantum wells”, *Journal of Applied Physics* **111**, 013501 (2012)

[2] **E.Gatti**, E. Grilli, M. Guzzi, D. Chrastina, G. Isella, A. Chernikov, V. Bornwasser, N. Köster, R. Woscholski, and S. Chatterjee, “Photoluminescence and ultrafast intersubband relaxation in Ge/SiGe multiple quantum wells”, *Physical Review B* **84**, 245319 (2011)

[3] **E. Gatti**, E. Grilli, M. Guzzi, D. Chrastina, G. Isella, and H. von Kaenel, "Room temperature photoluminescence of Ge multiple quantum wells with Ge-rich barriers", *Applied Physics Letters* **98**, 031106 (2011)

[4] P. Chaisakul, D. Marris-Morini, G. Isella, D. Chrastina, X. Le Roux, **E. Gatti**, S. Esmond, J. Osmond, E. Cassan, and L. Vivien, "Quantum confined Stark effect measurements in Ge/SiGe quantum well structures", *Optics Letters* **35**, 17, 2913 (2010)

## Proceedings

[1] G. Isella*, F. Bottegoni, F. Pezzoli, S. Cecchi, **E. Gatti**, D. Chrastina, E. Grilli, M. Guzzi, and F. Ciccacci, “Optical spin injection in SiGe heterostructures”, *Proceedings of SPIE* **8100**, 810007 (2011)

[2] P. Chaisakul*, D. Marris-Morini, G. Isella, D. Chrastina, X. Le Roux, **E. Gatti**, S. Edmond, J. Osmond, E. Cassan, and L. Vivien, "Ge/SiGe quantum wells structures for optical modulation", *Proceedings of the 7th IEEE International Conference on Group IV Photonics* (2010)

## Communications at congresses

[1] F. Pezzoli*, F. Bottegoni, G. Isella, **E. Gatti**, E. Grilli, F. Ciccacci, and M. Guzzi, “Robust optical orientation of spins in Ge/SiGe quantum wells”, at Quantum Information Processing and Communication (QIPC) 2011 International Conference, Zurich (Switzerland), September 5-9, 2011

[2] A. Giorgioni*, and **E. Gatti**, “Photoluminescence decay of direct and indirect transitions in Ge/SiGe multiple quantum wells”, at National School on the Physics of the Matter 2011, Erice (Italy), July 26 – August 7, 2011

[3] **E. Gatti***, A. Giorgioni, D. Chrastina, G. Isella, M. Guzzi, and E. Grilli, "Direct and indirect emission and carrier dynamics in Ge/SiGe multiple quantum wells" at E-MRS 2011 Spring Meeting, Nice (France), May 9-13, 2011

[4] P. Chaisakul*, D. Marris-Morini, L. Vivien, G. Isella, D. Chrastina, X. Le Roux, S. Edmond, **E. Gatti**, and E. Cassan, "Optical properties of Ge/SiGe quantum wells for optical modulation", at "Journées Nationales du Reseau Doctoral en MicroElectronique (JNRDM) 10" congress, Montpellier (France), 7-9 giugno 2010

[5] M. Bonfanti, **E. Gatti***, M. Guzzi, E. Grilli, D. Chrastina, G. Isella, and H. von Kaenel, "Direct and indirect gap related photoluminescence spectra in Ge/SiGe quantum wells" at E-MRS 2009 Spring Meeting, Strasburg (France), June 6-12, 2009

[6] **E. Gatti***, and M. Bonfanti, "Electronic transitions in Ge/SiGe MQWs", at "CMOS Photonics - 5th Optoelectronic and Photonic Winter School", Fai della Paganella, Trento (Italy), March 15-21, 2009

# Acknowledgements

I am very grateful to my tutor, prof. Mario Guzzi, for his trust on me, for the possibility of growing on the professional as well as on the human side, for his attention and support in all the aspects of my work. I am also really thankful to prof. Emanuele Grilli, for his steady support and his valuable help in the experimental problem solving. Prof. Guzzi and Prof. Grilli are for me an example of hard-working and expert scientists, fond of their work; I would be honored to become as skilled as they are.

During my PhD I have spent four months working at the Physics department of the Philipps-Universität in Marburg (Germany), under the supervision of Priv. Doz. Sangam Chatterjee. I sincerely acknowledge him for the very valuable opportunity he has given to me. My research stay in Marburg has been very fruitful and significant from both the scientific and the personal point of view. The possibility of working in an expert, young and dynamic group has kept my interest for physics and research alive.

I also thank prof. Stefano Sanguinetti and Emiliano Bonera for the useful discussions and for giving me their external point of view on my experimental results in a constructive and friendly way.

All the samples analyzed in this work have been grown at the L-NESS centre of Como by Giovanni Isella and Daniel Chrastina. I thank them not only for the sample growth, which was of course the basis for my experimental work, but also for the fruitful collaboration throughout all my PhD.

For the same reason, I am grateful to all the people I have worked with during these three years, in particular Prof. Giuseppe Grosso, Michele Virgilio and Giovanni Pizzi of the University of Pisa, and Prof. Laurent Vivien, Prof. Delphine Marris-Morini and Papichaya Chaisakul of the University of Paris Sud.

I am very thankful to my German colleagues, that have welcomed me in their group in a very friendly way. I would like to thank Niko for his explanations, for our nice and fruitful

scientific discussions and for his kindness, and Verena for her support and friendship. In particular, I really thank Alexej for the many good working hours spent shoulder-to-shoulder, for all the things he has taught me in his friendly and expert way, and for the very nice and pleasant moments we enjoyed outside the university.

I am thankful to Andrea, my “PhD-mate” for his interest and enthusiasm, to Anna for the work done together and her friendship, and to Fabio for his help, patience and kindness. Together with them, I thank Sergio, Claudio, Daniela, Elkid, Laura F. and Laura R., Roberto, Nicola, and Alexandra; in other words, all the people of my research-group. It has been a pleasure for me to share every working day with them.
I would like to thank especially my “predecessor” Matteo, for introducing me in the world of photoluminescence, Ge and QWs, for his support in the initial part of my PhD work, for all his help while I was learning how to be “a scientist” and for his friendship and steady interest.

I am very grateful to my family that has always supported and encouraged me, and that has taught me to do everything as best as I can, and to improve without forgetting my starting point.
As they know, I am really thankful to my friends: its really pleasant to share interests and projects with them, to mutually believe in our skills and capabilities, and, why not, to spend relaxing and funny moments together.
I am also thankful to all the friends I met because of my work, who are doing (or have just finished) their PhD in Milano or all over Europe: the possibility to confront each other, to share work and out-of-work moments and to meet new ways of life has been indeed valuable and has given me enthusiasm for my work and my projects.
Last, but actually first, it is impossible to express with few words how grateful I am to Roberto: the pleasure of sharing with him the important steps as well as everyday life is indeed gorgeous and irreplaceable for me.

For all these reasons, my PhD has been one of the most exciting and important experiences of my life, from every point of view. Thank you.

# Bibliography


[1] E. Bonera et al., *Phys. Rev. B* **79**, 075321 (2009)

[2] D.J. Norris et al., *Journal of Physics: Conference Series* **209,** 012061 (2010)

[3] F. Shäffler, *Semiconductor Science and Technology* **12**, 1515(1997)

[4] R. Soref, *Silicon* **2**, 1 (2010)

[5] D. Ahn et al., *Optics Express* **15**, 3916 (2007)

[6] J. Osmond et al., *Applied Physics Letters* **94**, 201106 (2009)

[7] J. Michel et al., *Nature Photonics* **4**, 527 (2010)

[8] S. Jongthammanurak et al., *Applied Physics Letters* **89**, 161115 (2006)

[9] J. Liu et al., *Optics Letters* **35**, 679 (2010)

[10] J. Liu et al., *Optics Express* **15**, 11272 (2007)

[11] M. El Kurdi et al., *Applied Physics Letters* **96**, 041909 (2010)

[12] M.A. Herman and H. Sitter, *Molecular Beam Epitaxy*, Springer, Berlin (1996)

[13] A. Strass, *Laser Focus World* **9**, 79 (1994)

[14] M. Virgilio and G. Grosso, *Journal of Physics: Condensed Matter* **18,** 1021 (2006)

[15] M. Bonfanti et al., *Physical Review B* **78**, 041407 (2008)

[16] S. Tsujino et al., *Applied Physics Letters* **89**, 262119 (2006)

[17] Y. Busby et al., *Physical Review B* **82**, 205317 (2010)

[18] Y.H. Kuo et al., *Nature* **437**, 1334 (2005)

[19] P. Chaisakul et al., *Optics Letters* **35**, 2913 (2010)

[20] J.E. Roth et al., *Optics Express* **15**, 5851 (2007)

[21] R.K. Shaevitz et al., *Photonics Society Summer Topical Meeting Series, 2010 IEEE*, 219 (2010)

[22] L. Lever et al., *Journal Of Lightwave Technology* **28**, 3273 (2010)

[23] N.S. Köster et al., *Physica Status Solidi C* **8**, 1109 (2011)

[24] E.Gatti et al., *Applied Physics Letters* **98**, 031106 (2011)

[25] C. Lange et al., *Physical Review B* **79**, 201306 (2009)

[26] P. Chaisakul et al., *Applied Physics Letters* **99**, 141106 (2011)

[27] L.K. Orlov et al., *Journal of Applied Physics* **80**, 415 (1996)

[28] Y.Yin et al., *Physical Review B* **52**, 8951 (1995)

[29] M. Bonfanti et al., *Physica E* **41**, 972 (2009)

[30] M. Virgilio et al., *Physical Review B* **79**, 075323 (2009)

[31] M. De Seta et al., Applied Physics Letters **95**, 051918 (2009)

[32] R.K. Shaevitz et al., *AIP Advances* **1**, 032164 (2011)

[33] L. Carroll et al., *Applied Physics Letters* **99**, 031907 (2011)

[34] S.A. Claussen et al., *Optics Express* **18**, 25596 (2010)

[35] N.S. Köster et al., Proceedings of SPIE (2010) **7600**, 76000B-1 (2010)

[36] C. Lange et al., *Physical Review B* **81**, 045320 (2010)

[37] F. Pezzoli et al., *Optical spin injection and spin lifetime in Ge heterostructures*, submitted to *Physical Review Letters* (2011)

[38] G. Isella, et al., *Solid-State Electronics* **48**, 1317 (2004)

[39] M. Cardona and F.H. Pollak, *Physical Review* **142**, 530 (1966)

[40] M.M. Rieger and P. Vogl, *Physical Review B* **48**, 14276 (1993)

[41] M.V. Fischetti and S.E. Laux, *Journal of Applied Physics* **80**, 2234 (1996)

[42] K. Brunner, Reports of Progress in Physics **65,** 27 (2002)

[43] D.J. Paul, *Semiconductor Science and Technology* **19,** R75 (2004)

[44] Y. Shiraki and N. Usami, ed. by, *Silicon-germanium (SiGe) nanostructures*, Woodhead Publishing, Cambridge (2011)

[45] S.M. Sze, *Semiconductor Devices: Physics and Technology*, Wiley, New York (1985)

[46] A.R. Denton and N. W. Ashcroft, *Physical Review A* **43**, 3161 (1991)

[47] O. Madelung, ed., *Landolt-Börnstein: Numerical Data and Functional relationships in Science and Technology - New Series*, Vol. III/17a, Springer Verlag, 1982

[48] J. Dismukes et al., *Journal of Physical Chemistry* **68**, 3021 (1964)

[49] E. Kasper et al., *Journal of Crystal Growth* **157**, 68 (1995)

[50] S. de Gironcoli et al., *Physical Review Letters* **66**, 2116 (1991)

[51] E. Kasper and H.J. Herzog, *Structural properties of silicon-germanium (SiGe) nanostructures*, in Y. Shiraki and N. Usami, ed. by, *Silicon-germanium (SiGe) nanostructures*, Woodhead Publishing, Cambridge (2011)

[52] J.H. van der Merwe, *Surface Science* **31**, 198 (1972)

[53] K.S. Kim et al., *Journal of Vacuum Science and Technology* **16**, 2663 (1998)

[54] Novikova S. I., *Soviet Physics Solid State* (English Transl.) **2**, 37 (1960)

[55] H.P. Singh, *Acta Crystallographica* **24a**, 469 (1968)

[56] N. Mori, *Electronic band structures of silicon-germanium (SiGe) alloys*, in Y. Shiraki and N. Usami, ed. by, *Silicon-germanium (SiGe) nanostructures*, Woodhead Publishing, Cambridge (2011)

[57] P. Lautenschlager et al., *Physical Review B* **36**, 4281 (1987)

[58] J. Weber and M.I. Alonso, *Physical Review B* **40**, 5683 (1989)

[59] C. Pickering et al., *Journal of Applied Physics* **73**, 239 (1993)

[60] J.S.Kline et al., *Heletica Physica Acta* **41**, 968 (1968)

[61] Y.P. Varshni, *Physica* **34**,149 (1967)

[62] T. Ebner et al., *Physical Review B* **57**, 15448 (1998)

[63] Y. Ishikawa et al., *Journal of Applied Physics* **98**, 013501 (2005)

[64] Y.Kuo et al., *IEEE Journal of Selected Topics in Quantum Electronics* **12**, 1503 (2006)

[65] W.T. Masselink et al., *Physical Review B* **32**, 8027 (1985)

[66] R. Dingle et al., *Physical Review Letters* **33**, 827 (1974)

[67] P. Blood, *IEEE Journal of Quantum Electronics* **36**, 354 (2000)

[68] M. Bonfanti, *Ge Multiple Quantum Wells, Electronic states and optical properties*, PhD thesis, Università di Milano-Bicocca, Milan (2008)

[69] G. Bastard, *Wave mechanics applied to semiconductor heterostructures*, Monographies da Physique, France, 1988

[70] J.H. Davies, *The physiscs of low dimensional semiconductors: an introduction*, Cambridge University Press, Cambridge, 1998

[71] D.A.B. Miller et al., *Physical Review Letters* **53**, 2173 (1984)

[72] U. Arad et al., *IEEE Photonics Technology Letters* **15**, 1531 (2003)

[73] C.P. Liu et al., *IEEE Transactions on Electron Devices E* **86C**, 1281 (2003)

[74] I. Bar-Joseph et al., *Applied Physics Letters* **50**, 1010 (1987)

[75] D.A.B. Miller et al., *Physical Review B* **32**, 1043 (1985)

[76] M. Virgilio and G. Grosso, *Physical Review B* **77**, 165315 (2008)

[77] L. Martinelli, *SiGe heterostructures for microelectronics*, PhD thesis, University of Milano-Bicocca, Milan (2003)

[78] E. Taşyürek et al., Proceedings of the 7th IEEE International Conference on Group IV Photonics (GFP), Beijing (2010)

[79] J.T. Devreese, *Polarons* in G.L. Trigg, ed. by, *Encyclopedia of Applied Physics,* Wiley-VCH, Weinheim (1996)

[80] V. Härle et al., *Journal of Applied Physics* **75**, 5067 (1994)

[81] S. Fukatsu et al., *Journal of Crystal Growth* **157**, 1 (1995)
[82] M.W.C. Dharma-wardana et al., *Physical Review B* **41**, 5319 (1990)
[83] C.E. Bottani et al., *Applied Physics Letters* **69**, 2409 (1996)
[84] F. Pezzoli, *Raman Spectroscopy od $Si_{1-x}Ge_x$ micro and nanostructures*, PhD thesis, Università di Milano-Bicocca, Milan (2007)
[85] G.A. Northropet al., *Vacuum Science and Technology B* **10**, 2018 (1992)
[86] Y. Shiraki et al., *Applied Physics Letters* **68**, 2097 (1996)
[87] N. L. Rowell et al., *Thin Solid Films* **321**, 158 (1998)
[88] W. Weber, *Physical Review B* **15**, 4789 (1977)
[89] N.G. Kalugin et al., *JETP Letters* **58**, 200 (1993)
[90] G.A. Thomas et al., *Physical Review Letters* **37**,1000 (1976)
[91] A. Uddin et al., *Physical Review B* **41**, 3078 (1990)
[92] F. Wooten, *Optical properties of solids*, Academic Press, New York (1972)
[93] J.I. Pankove, *Optical processes in semiconductors*, Prentice Hall, Englewood Cliffs (1971)
[94] M. Herman et al., *Journal of Applied Physics* **70** (1991) R1
[95] J. Christen et al., *Applied Physics Letters* **44**, 84, (1984)
[96] J. Feldmann et al., *Physical Review Letters* **59**, 2337 (1987)
[97] T. Amand et al., *Journal of Applied Physics* **72**, 2077 (1992)
[98] J. Tignon et al., *Physica E* **2**, 126 (1998)
[99] W. Hoyer et al., *Physical Review B* **72**, 075324 (2005)
[100] N. L. Rowell et al., *Journal of Applied Physics* **74**, 2970 (1993)
[101] S. Fukatsu et Y. Shiraki, *Journal of Crystal Growth* **150**, 1025 (1995)
[102] M. Engel et al., *Journal of Crystal Growth* **93**, 359 (1988)
[103] H. Akiyama et al., *Physical Review Letters* **72**, 924 (1994)
[104] M. Grundmann and D. Bimberg, *Physical Review B* **38**, 13486 (1982)
[105] C. Weisbuch and B. Vinter, *Quantum Semiconductor Structures: Fundamentals and applications*, Academic Press, New York (1991)
[106] V. Srinivas et al., *Physical Review* **46**, 10193 (1992)
[107] M. Grundmann et al., *Physical Review B* **41**, 10120 (1990)
[108] L.C. Andreani et al., *Solid State Communication* **77**, 641 (1991)
[109] Y. Takahashi et al., *Applied Physics Letters* **60**, 213 (1992)
[110] K. Tanaka et al., *Journal of Applied Physics* **80**, 6991 (1996)

[111] S. Sanguietti, M. Guzzi, and M. Gurioli, C. Lamberti, edited by, *Characterization of semiconductor heterostructures and nanostructures*, Chapter 6, Elsevier, Amsterdam (2008)

[112] F. Yang et al., *Physical Review Letters* **70**, 323 (1993)

[113] Y. T. Oh et al., *Solid State Communications* **93**, 629 (1995)

[114] S. Shirakata et al., *Physica Status Solidi A* **203**, 2680 (2006)

[115] X. Mu et al., *Laser physics* **15**, 225 (2005)

[116] G. Mak and W. W. Rühle, *Physical Review B* **52**, R11584 (1995)

[117] T. Elsaesser et al., *Semiconductor Science and Technology* **7,** 144 (1992)

[118] H. Haug and S.W. Koch, *Quantum theory of the optical and electronic properties of semiconductors*, 5th ed., World Scientific, Singapore (2009)

[119] E. Einsenberg and R. Resnik, *Quantum Physics of Atoms, Molecules, Solids, Nuclei and Particles*, John Wiley and Sons, New York, 1985

[120] M. Fox, *Optical properties of solids*, Oxford University Press, New York (2010)

[121] L. Esaki, *IEEE Journal of Quantum Electronics* **22**, 1611 (1986)

[122] L.J. Sham, *Superlattices and Microstructures* **5**, 335 (1989)

[123] Y. Fu and K.A. Chao, *Physical Review B* **43**, 4119 (1991)

[124] A. Franceschetti and A. Zunger, *Applied Physics Letters* **68**, 3455 (1996)

[125] G.E.W. Bauer and T. Ando, *Physical Review B* **34**, 1300 (1986)

[126] H.P. Komsa et al., *Journal of Physics: Condensed Matter* **20**, 315004 (2008)

[127] H. Ibach and H. Lüth, *Solid-state physics*, Springer, Berlin (2003)

[128] D.A.B. Miller et al., *Applied Physics Letters* **41**, 679 (1982)

[129] G. Margaritondo, in C. Lamberti, edited by, *Characterization of semiconductor heterostructures and nanostructures*, Chapter 12, Elsevier, Amsterdam (2008)

[130] M. Kummer et al., *Materials Science and Engineering B* **89**, 288 (2002)

[131] C. Rosenblad et al., *Journal of Vacuum Science and Technology A* **16**, 2785 (1998)

[132] C. Rosenblad et al., *Applied Physics Letters* **76**, 427 (2000)

[133] H. von Känel et al., *Applied Physics Letters* **80**, 2922 (2002)

[134] S. Marchionna et al., *Materials Science in Semiconductor Processing* **9**, 802 (2006)

[135] E.A. Fitzgerald et al., *Applied physics letters* **59**, 881 (1991)

[136] A. Bignazzi et al., *Review of Scientific Instruments* **67**, 666 (1996)

[137] S. Chatterjee, *Nonequilibrium Carrier Dynamics in Semiconductor Heterostructures,* Habilitationsschrift, Philipps Universität Marburg, Marburg, Germany (2009)